School of Physics and Astronomy

Coherent Non-linear Microscopy Employing Novel Femtosecond Laser Sources

Dominykas Gudavičius

Submitted for the degree of Doctor of Philosophy
School of Physics and Astronomy
Cardiff University

31-03-2024

Summary

Coherent Raman scattering (CRS) which is divided into Coherent anti-Stokes Raman scattering (CARS) and stimulated Raman scattering (SRS) microscopy combined with second/third harmonic generation (SHG/THG) is powerful label-free imaging method which is demonstrated in this thesis with various experimental setups. It provides concise history and introduction to CRS/SHG/THG microscopy and molecule vibrations. It further dives into background of the instrumentation used throughout the thesis such as pulsed lasers, optical parametric devices and how they are used in microscopy. Pulse characterization methods are described which allow to control pulse duration for most optimal spectral resolution in CARS/SRS experiments when femtosecond pulses are used. Following that, the thesis introduces basics of noise theory that provides noise characterization of commercially available OPO. Two laser systems with different gain material are compared (Yb and Ti:Sa) and it is concluded that both are shot-noise limited and suitable for SRS microscopy. To demonstrate SRS, Calu-3 cells were images by both systems. Later, microscopy layout changes are explained which allowed to add dual CARS modality to an existing setup. Experiments were performed which show that it is possible to record polystyrene (PS) and polymethyl methacrylate (PMMA) bead flow without motion artifacts and to simultaneously record deuterated water and water inside HeLa cells by using commercially available OPO. Additionally, it includes technique to perform pre-resonance SRS. Finally, novel technique which uses amplified laser system and multiple focal points to image the sample are introduced and discussed in detail. The image reconstruction and optimization algorithms of multifocal approach allow to reconstruct an image with PSF size similar to previously reported in confocal microscopy.

Acknowledgement

I would like to thank Prof. Wolfgang Langbein and Prof. Paola Borri without whose support completing this scientific journey would have been impossible. Their time and consistent effort allowed me to learn and grow.

I am grateful for the opportunity to do secondments and collaborative research at other labs, namely Prof. Hervé Rigneault, Prof. Andreas Zumbusch and Dr. Sandro Heuke. I would also like to thank my close colleagues, other PhD students, Dr. Eric Michele Fantuzzi, Andrea Pruccoli who helped and spent time with me both inside and outside of a laboratory, making my secondments a well-rounded experience.

I could not have conducted my research without the lasers and day-to-day support provided by Light Conversion. Thank you for believing that I can make it until the end of my PhD even though I came from a completely different field.

Noriu padėkoti savo draugams Karoliui, Tautvydui, Dovydui, Tadui, Domantui, Alvydui ir kitiems už praleistą laiką kartu tiek ramiai dienos metu, tiek judant mieste vakarais, ačiū jums už tai. Taip pat noriu padėkoti savo mamai už besąlygišką palaikymą visais gyvenimo atvejais. Galiausiai, didelis ačiū mano merginai Eglei už plieninę kantrybę ir rūpestį.

Contents

List of Figures

List of Tables

Chapter 1

Introduction

Microscopy is an inextricable part of modern research and technological development. First compound microscopes in the 16th century allowed humans to observe objects with magnifications and spatial resolution which were impossible before, revealing tissues, cells, various minerals and other materials which led to multiple life-changing discoveries and inventions [3]. However, one of the limiting factor for life science and biology soon became evident—biological matter often lacks contrast and it is hard to track internal changes or distinguish parts of the cell even when the magnification and resolution is sufficient. To solve this problem, various staining methods were developed like hematoxylin and eosin staining, trypan blue dye staining and many more, which became standards in their area. The biggest issues with biological sample staining is the time it takes to prepare the sample, dyes themselves as they can change the sample, the inability to target exact parts of the cell and most importantly, the sample often cannot be alive. A breakthrough came with the development of fluorescence and genetically encoded dyes. The dye can be engineered in a way to attach only to a specific part of the cell and when excited, it emits light at different frequency. With a well engineered optics system the emitted frequency can be detected and an image reconstructed with higher magnification, resolution and most importantly contrast than bright-field microscopy. Since the first description of the fluorescence phenomena in 1852 it led to multiple major cell biology discoveries and now is considered as a mature and well-established microscopy method [4]. It is possible to achieve super-resolution and cutting-edge imaging speeds by using fluorescence microscopy techniques [5, 6]. Additionally, fluorescence microscopy has found a way into operating rooms where fluorescence-guided glioma surgeries are performed [7, 8]. Miniaturization of electronics together with novel imaging approaches led to coin-sized devices capable of imaging $140\,\mathrm{mm}^3$ volume with $7\,\mu\mathrm{m}$ lateral and $200\,\mu\mathrm{m}$ axial resolution.

As with any other technology or method, fluorescence is not suited for all applications and comes with a set of problems. First, the molecules of fluorescence dyes are relatively large and can be even bigger than the object of interest which influences the behavior. Fluorescence dye can influence DNA fragments under investigation [9]. Despite availability of a wide selection of dyes, another issue is the broad absorption and emission spectra due to strong vibrational coupling of many different modes, and the liquid surrounding [10]. This limits the dyes that can be distinguished at the same time to 4 or 5. The excitation for some of the fluorescence dyes is in the blue or UV range which renders poor penetration depth due to absorption an scattering which can also damage the sample. Finally, the fluorophores

experience bleaching which implies that they cannot be illuminated for a long time without loosing fluorescence signal.

An alternative which circumvents majority of fluorescence problems is Raman imaging which is based on vibrational contrast of different molecules. Spontaneous Raman imaging allows to extract rich spectral information from a sample without requiring any sample modifications and is sensitive to concentration changes. These features allow to diagnose disease in tissues, classify bacteria, etc [11, 12]. The greatest disadvantage of spontaneous Raman is weak signal with combined fluorescence background which requires long exposure times that are undesirable for time-evolving biological systems. The weak signal problem can be overcome by achieving coherent Raman scattering (CRS) which is several orders of magnitude stronger and is classified into stimulated Raman scattering (SRS), coherent anti-Stokes Raman scattering (CARS) and coherent Stokes Raman scattering (CSRS). Just like spontaneous Raman, CRS does not require any staining or dyes to provide chemical specificity of the sample and there are no bleaching effects allowing to image the same sample multiple times. Two major areas where CRS is developing is imaging speed and resolution. Since the linewidth of molecular spectral peaks are in the range of $10\,\mathrm{cm}^{-1}$, one can multiplex and image more than 5 channels without sacrificing speed advantage [13] or retrieve the whole spectrum in the order of microseconds by using broadband white-light continuum pulses both in CARS and SRS setups [14]. The acquisition speed of spectra is limited by the non-resonant background in CARS microscopy which distorts the Raman spectrum, and the lack of commercially available lock-in spectrometers for SRS. Additionally, point scanning approaches were demonstrated capable of detecting epi-CARS from live tissue in video rate regimes [15] but requires high average pulse power at a single focal point. For improved resolution, super resolution methods were demonstrated named stimulated emission depletion and saturated excitation microscopy which allows to image below diffraction limit without using any labels [5, 16, 17] but requires high excitation power and experimental complexity. An alternative to this, is the application of deconvolution algorithms which removes image distortions and can go to 59 nm spatial resolution [18]. The drawback of deconvolution methods is the long algorithm processing times and possible creation of false artifacts.

CRS signals come with a background which is independent of the detection method [19]. To eliminate the influence of the non-resonant background in CARS microscopy, retrieval algorithms like Kramer-Krönig transformation and maximum entropy approach can be used [20]. The drawback is the possibility of the phase errors when the non-resonant background is incorrectly estimated. Recently, new approaches were applied by using machine learning [21, 22] which allow to remove the non-resonant background and extract resonant signal with high precision and speed but requires large data sets to train. For SRS background removal, methods such as frequency modulation, polarization modulation, and phase modulation have been shown to eliminate the majority of background contributions [23]. However, despite their effectiveness, these techniques introduce additional complexity to the setup compared to conventional amplitude modulation.

Due to abundance of high repetition rate (MHz range) and low pulse energy (nJ range) laser systems, majority of coherent Raman microscopes are point-scanning. This is a well-established method with demonstrated 160 ns/point pixel dwell time CARS imaging but the speed is fundamentally limited by CARS signal saturation [15, 24]. This leads to novel wide-field CARS approaches which preserve z section-

ing capabilities [25, 26]. Recently, surface enhanced wide-field CARS approach was demonstrated enabling live cell imaging with 120 Hz rate in 130×130 µm^2 area by using gold nanoparticles to enhance CARS [27]. The wide-field approach became more appealing with the development of amplified laser systems with µJ pulse energies. Researchers have demonstrated CARS imaging by using random illumination which opens doors for fast CARS imaging potentially breaking current state-of-the art scanning CARS microscope imaging speed [28]. Similarly, a multifocal approach with an amplified laser system and many (>1000) foci is demonstrated for the first time in chapter 6 which has a potential for video-rate megapixel CARS imaging.

The majority of work described in this thesis was performed at Light Conversion where the main task was to test and explore the performance of laser systems in the field of non-linear microscopy.

Chapter 2

Background

2.1 Spontaneous Raman scattering

To understand CRS, first spontaneous Raman scattering needs to be introduced. It is a physical process, discovered in 1928 by C.V. Raman and K.S. Krishnan, which is used in spectroscopy to probe the molecular vibrational frequencies [29, 30]. When molecules are interacting with light, there is a small probability for inelastic scattering in which the frequency of a scattered photon is changed. In microscopy and spectroscopy applications, it is used to map chemical species based on their vibrational spectra. Spontaneous Raman scattering is weak, with typical cross section of $10^{-29}\,\mathrm{cm}^2$ per vibrational mode, while absorbtion cross sections for electronic transitions are typically $10^{-15}\,\mathrm{cm}^2$ which makes it not well suited for microscopy [31]. Energy diagram of the spontaneous Raman effect is sketched in Figure 2.1.

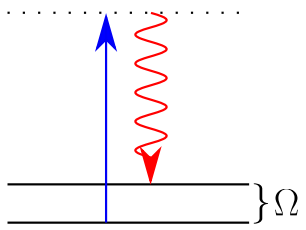

Figure 2.1: Spontaneous Raman energy diagram. Pump beam (blue arrow) causes spontaneous Raman scattering which is longer wavelength and depends on the vibrational energy level with frequency Ω.

To get more insight into the process, we start by defining induced dipole moment which depends on the polarizability $\alpha(t)$ and the applied external electric field $E(t) = E_0 \cos(\omega_\mathrm{p} t)$

$$P = \alpha(t)E(t). \tag{2.1}$$

The polarizability will change as the molecule vibrates and can be written in a Taylor series with generalized coordinates $q(t)$

$$\alpha = \alpha_0 + \left(\frac{\partial \alpha}{\partial q}\right)_0 q(t) + \dots, \tag{2.2}$$

where higher order terms are not considered.

The generalized coordinates can be written as a linear superposition of N vibrational modes which are defined by a periodic function

$$q(t) = \sum_{i=1}^{N} q_i \cos(\omega_i t)\,. \tag{2.3}$$

By combining equations (2.1), (2.2) and (2.3), and treating only a single vibrational mode as treatment of other modes is going to be identical, we obtain

$$P = \alpha_0 E_0 \cos(\omega t) + \frac{E_0 q}{2}\left(\frac{\partial \alpha}{\partial q}\right)_0 \Big[\cos((\omega_p + \omega_i)t) + \cos((\omega_p - \omega_i)t)\Big]\,. \tag{2.4}$$

Equation 2.4 gives important results. First, the second term indicates new frequencies at $\omega_p + \omega_i$ and $\omega_p - \omega_i$ called anti-Stokes and Stokes scattering respectively which appear as sidebands for the fundamental frequency. Secondly, the term $\left(\frac{\partial \alpha}{\partial q_i}\right)_0$ suggest that some vibrational bands are Raman inactive as the polarizability in one bind can shrink while the other bind extend leading to cancellation of the first order electronic polarizability as demonstrated in Figure 2.2. Since the vibrational frequencies of the molecule depend on the atomic wights, bond strength and geometry, it is possible to identify molecules by recording Raman spectrum which leads to the field of Raman spectroscopy and microscopy.

Figure 2.2: Polarizability during the oscillation must change for the mode to be Raman active. Raman active mode of carbon dioxide a) and Raman inactive mode of carbon dioxide b).

2.2 Coherent Raman scattering (CRS) microscopy

The spontaneous process can be enhanced by achieving coherence which requires two beams: shorter wavelength (called pump) and longer wavelength (called Stokes). If the energy difference $\hbar(\omega_\mathrm{p} - \omega_\mathrm{S})$ between the incident pump beam with angular frequency ω_p and the Stokes beam with angular frequency ω_S matches the energy difference between the ground and excited vibrational state of a molecule $\hbar\Omega$, four new processes can take place. The processes are coherent anti-Stokes Raman scattering (CARS) which scatters light at angular frequency ω_aS, coherent Stokes Raman scattering (CSRS) which scatters light at angular frequency ω_cS, stimulated Raman loss (SRL) with pump beam loosing intensity and stimulated Raman gain (SRG) with Stokes beam gaining intensity. SRL and SRG processes are denoted as stimulated Raman scattering (SRS). CARS, CSRS and SRS energy diagrams are presented in Figure 2.3.

To express it mathematically, we start by defining a molecule as driven oscillator by a differential equation [32]

$$\frac{\mathrm{d}^2 q}{\mathrm{d}t^2} + 2\gamma\frac{\mathrm{d}q}{\mathrm{d}t} + \omega_v^2 q = \frac{F(t)}{m}\,, \tag{2.5}$$

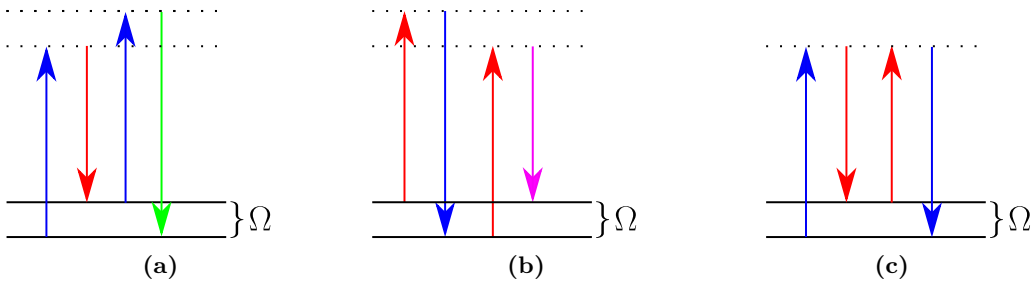

Figure 2.3: Energy level diagrams of CARS (a), CSRS (b) and SRS (c). Blue, red, green and pink arrows indicate pump, Stokes, CARS and CSRS angular frequencies respectively. Dashed lines are virtual energy levels.

where γ is a damping coefficient and $F(t)$ is a driving force.

The energy of the dipole in the field is

$$W = \frac{1}{2}\langle P(t)E(t)\rangle = \frac{1}{2}\alpha\langle E^2(t)\rangle\,, \tag{2.6}$$

where $\langle\rangle$ denote time average over an optical period.

The force is then

$$F = \frac{\partial W}{\partial q} = \frac{1}{2}\left(\frac{\partial \alpha}{\partial q}\right)_0 \langle E^2(t)\rangle\,. \tag{2.7}$$

By knowing pump and Stokes fields cause beat frequency which is the main driving force for the oscillator, we write

$$F = \left(\frac{\partial \alpha}{\partial q}\right)_0 \left[E_\mathrm{p}E_\mathrm{S}^* e^{-i(\omega_\mathrm{p}-\omega_\mathrm{S})t} + \mathrm{c.c.}\right]. \tag{2.8}$$

Knowing that differential equation (2.5) has a solution

$$q(t) = Q(\omega)e^{-i(\omega_\mathrm{p}-\omega_\mathrm{S})t} + \mathrm{c.c.}\,, \tag{2.9}$$

and by knowing the force which is defined in equation (2.8) and general solution to equation (2.5), we can solve for the oscillation amplitude which turns out to be

$$Q(\omega) = \frac{1}{m}\left(\frac{\partial \alpha}{\partial q}\right)_0 \frac{E_\mathrm{p}E_\mathrm{S}^*}{\omega - (\omega_\mathrm{p}-\omega_\mathrm{S})^2 - 2i(\omega_\mathrm{p}-\omega_\mathrm{S})\gamma}\,. \tag{2.10}$$

Revisiting equation (2.1) and introducing pump and Stokes fields yields polarisation

$$P = N_v\alpha(t)(E_\mathrm{p}(t) + E_\mathrm{S}(t)) = N\left[\alpha_0 + \left(\frac{\partial \alpha}{\partial q_i}\right)_0 q(t)\right](E_\mathrm{p}(t) + E_\mathrm{S}(t))\,, \tag{2.11}$$

where N_v is number of bonds per volume.

By following the same steps as in equations (2.2), (2.3) and looking only at the non-linear terms, we obtained induced polarization as

$$P_\mathrm{NL} = P(\omega_\mathrm{cS})e^{-i(2\omega_\mathrm{S}-\omega_\mathrm{p})} + P(\omega_\mathrm{S})e^{-i\omega_\mathrm{S}} + P(\omega_\mathrm{p})e^{-i\omega_\mathrm{p}} + P(\omega_\mathrm{aS})e^{-i(2\omega_\mathrm{p}-\omega_\mathrm{S})} + \mathrm{c.c.}\,, \tag{2.12}$$

which suggest new fields at frequencies $2\omega_S - \omega_p$, ω_S, ω_p, $2\omega_S - \omega_p$, $2\omega_p - \omega_S$ corresponding to CSRS, SRG, SRL and CARS respectively. Writing the full polarizability for CARS, we obtain

$$P(\omega_{aS}) = \frac{N_v}{m}\left(\frac{\partial\alpha}{\partial q}\right)^2 \frac{E_p^2 E_S^*}{\omega - (\omega_p - \omega_S)^2 - 2i(\omega_p - \omega_S)\gamma} = 6\epsilon_0 \chi_{NL} E_p^2 E_S^* \,, \tag{2.13}$$

where ϵ_0 is the permittivity of free space and χ_{NL} is the non-linear susceptibility.

Since anti-Stokes field is linearly proportional to the polarisation, the anti-Stokes signal intensity is proportional to the square of polarisation,

$$I(\omega_{aS}) \propto |\chi_{NL}|^2 I_p^2 I_S \,. \tag{2.14}$$

From equation (2.14) we see that CARS intensity depends on the number of bonds per volume squared N_v^2 and the signal scales quadratically with the pump intensity I_p and linearly with the Stokes intensity I_S. In case of SRS, the generated $E_p^{(3)}$ and $E_S^{(3)}$ electric fields interfere destructively and constructively. In case of SRL, the intensity is expressed

$$I(\omega_p) = \frac{\epsilon_0 c}{2}\left|E_p^{(3)} + E_p\right|^2 \propto \left|E_p^{(3)}\right|^2 + \left|E_p\right|^2 - 2\left|E_p\right|^2\left|E_S\right|^2 \mathrm{Im}(\chi_{NL}) \,. \tag{2.15}$$

Equation (2.15) shows an important aspect as the change in pump intensity is related to the imaginary part of the non-linear susceptibility and thus depends linearly on the number of bonds in the sample [32].

Due to the coherent nature, CARS can be more intense, by a factor of up to the number of vibrational bonds probed when compared to spontaneous Raman scattering intensity [31]. It is important to note that CARS and CSRS produce a signal at a frequency different from the incident laser beams, while SRS produces a signal at the same frequency and therefore modulates the transmitted beam intensity. CRS does not require labels, and therefore allows investigations of samples in their natural state [33]. CSRS allows more favorable epi-detection due to differences in phase matching conditions but is not discussed here due to the complications, compared to CARS, of signal detection which is in the infrared region when near-infrared femtosecond lasers are employed [34]. All CRS processes are presented in Figure 2.4.

The first use of CARS in microscopy was reported in 1982 where imaging with chemical specificity was demonstrated on acetonitrile and octane samples [35]. However, due to a lack of signal because of the dye lasers used, which provided 250 mW and 150 mW average power, 6 ps duration pulses with 80 MHz repetition rate, it was insufficient to yield high quality images so that signal-to-noise ratio (SNR) became an important issue in CARS microscopy early on. In addition, CARS has an inherent property—a non-resonant background which distorts the Raman signature. The most popular methods to reduce non-resonant background are by employing polarization CARS or time-resolved CARS schemes with the price of also reducing the resonant CARS signal [33]. CARS is relatively weak with a low signal to background ratio which leads to difficulties in analyzing CARS images [36]. However, epi-detection CARS can greatly improve the contrast when compared to forward CARS because of the dark-field configuration which discriminates heavily scattering from homogenous structures [37]. SRS was suggested as an alternative vibrational

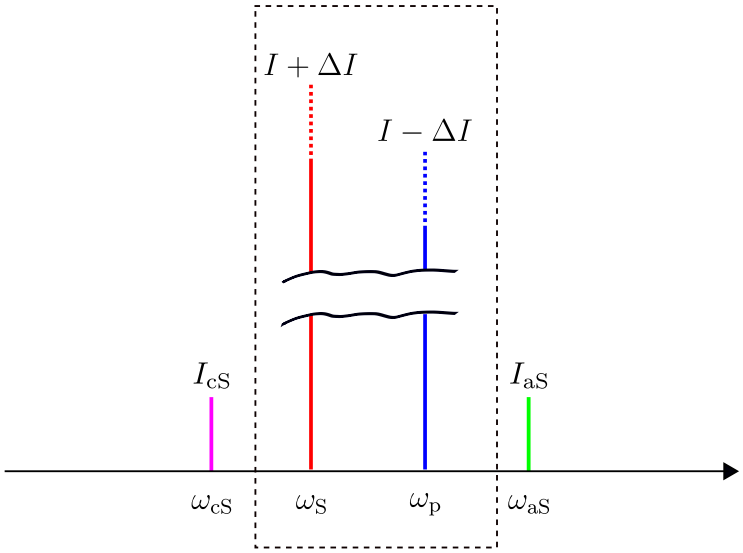

Figure 2.4: CRS processes in the frequency domain where ω_{aS} is CARS angular frequency with intensity I_{aS}; ω_{cS} is CSRS angular frequency with intensity I_{cS} and dashed rectangle shows SRS process where pump beam looses intensity while Stokes beam gains intensity. Line break indicates that CARS and CSRS intensities are significantly lower.

contrast mechanism in microscopy in 2007 [38]. One of the main drawbacks of SRS is the weak modulation of a strong incident laser beam requiring high-frequency modulation to reach shot-noise limited performance. Therefore, noise characteristics of the excitation beams are strongly affecting the performance of SRS microscopes [39]. It is relevant to note that SRS is not completely free from background. The most common background contributions are photo-thermal lensing, cross-phase modulation and transient absorption [19]. Photo-thermal lensing arises due to temperature changes in the sample which affect the refractive index and distorts the detected signal changing the fraction of the transmitted beam which is detected. Cross-phase modulation is caused by third-order susceptibility and the interaction between pump and Stokes beams, changing beam propagation and frequency due to optical Kerr effect that is similar to photothermal effect but is instantaneous. Transient absorption is induced when pump and Stokes beams interact in such way that two photon absorption takes place leading to electronic excitation [19]. A short comparison between CARS and SRS is presented in Table 2.1.

	Signal frequency	Signal relation to susceptibility	Signal scaling	Non-resonant background	Beam modulation
CARS	$2\omega_{\mathrm{p}} - \omega_{\mathrm{S}}$	$\propto \lvert\chi^{(3)}\rvert^2$	N^2, I_{p}^2	high	not required
SRS	ω_{p} or ω_{S}	$\propto \mathrm{Im}(\chi^{(3)})$	linear	low	required

Table 2.1: Comparison between CARS and SRS.

Typical CARS and SRS setups with corresponding diagrams can be seen in Figure 2.5. For SRS, the laser beam is split into two separate beams where one beam is used to pump an optical parametric oscillator (OPO) while the remaining beam is modulated. The pulses at a different frequency from the laser and OPO are then recombined. The overlapped pulses (in space and time) then enter the

microscope where it interacts with the sample. One of the beams is suppressed by a spectral filter while the other reaches the photo detector and is sent to the lock-in-amplifier. The lock-in amplifier extracts intensity change in pump or Stokes beam by multiplying the reference signal with the detector signal and then averaging the result over time. This avoids low intensity noise by using high frequency detection, reducing noise as $1/\sqrt{t}$, where t is time, while signal is kept constant. Typical CARS setups are similar but do not require modulation nor lock-in-detection since light is scattered at frequency $2\omega_\mathrm{p} - \omega_\mathrm{S}$ free of excitation laser background and can be isolated by optical bandpass filters.

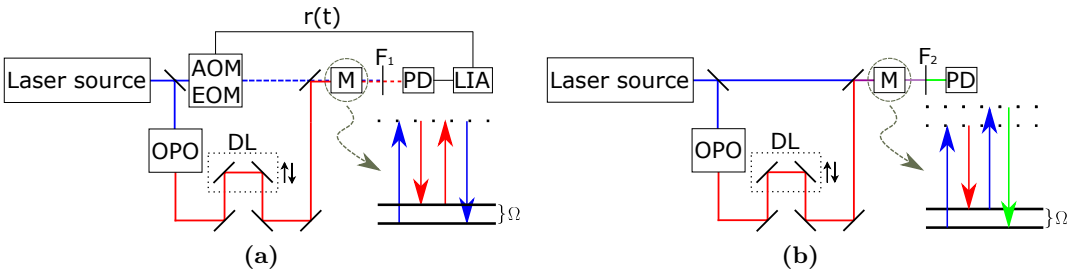

Figure 2.5: SRS (a) and CARS (b) experimental setups with corresponding diagrams. AOM, acousto-optic modulator or EOM; r(t), reference signal; DL, delay line; M, scanning microscope with sample; F_1, pump or Stokes filter; F_2, pump and Stokes filter; PD, photodetector; LIA, lock-in amplifier; OPO, optical parametric oscillator. Dashed lines are virtual energy levels.

An image illustrating raster scanning SRS imaging is presented in Figure 2.6. Without any additional stains or any special sample preparation procedure it is possible to identify lipid droplets on the Calu-3 cell sample by targeting the resonance at $2850\,\mathrm{cm}^{-1}$ which would be impossible with a regular bright-field microscope.

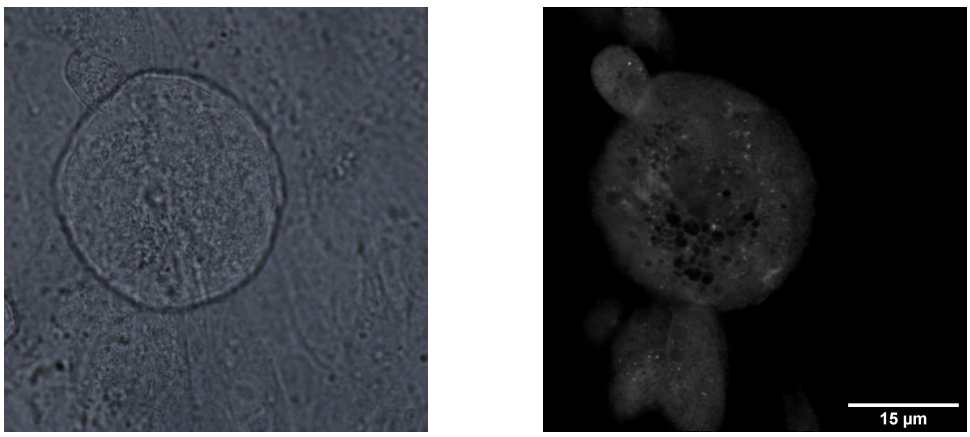

Figure 2.6: Bright-field (a) and SRS (b) images of the same Calu-3 cell clump at the same z section. Min value represents 0 V while the max value represents 10 mV SRS is targeting lipid region while chemical specificity for the bright-field imaging is impossible. SRS images were taken with the setup described in chapter 3.

2.3 Second/third harmonic generation (SHG/THG)

SHG and THG are coherent processes in which two or three photons with the same frequency are combined through a non-linear interaction and produce a photon with double or triple the frequency of the original photons. Mathematically, SHG is derived from equation (2.37) while THG is derived by expanding equation (2.35) to the third-order susceptibility term. One of the main differences between SHG and THG is that the third-order susceptibility tensor is generally non-zero in centrosymmetric structures while the second order susceptibility for such structures is zero. Another important property of THG is that the total emission towards the far field is canceling in an isotropic and homogeneous medium assuming $n(3\omega) = n(\omega)$ and an infinitely extended medium and Gaussian focus [40]. This is caused by the destructive interference between waves generated before and after the focal plane due to the Gouy phase shift [41]. This property suppresses THG from the bulk, makes THG a useful technique for 3D imaging when the medium is not homogeneous as THG is induced at the interfaces [42]. A schematic illustration of SHG and THG generation is presented in Figure 2.7.

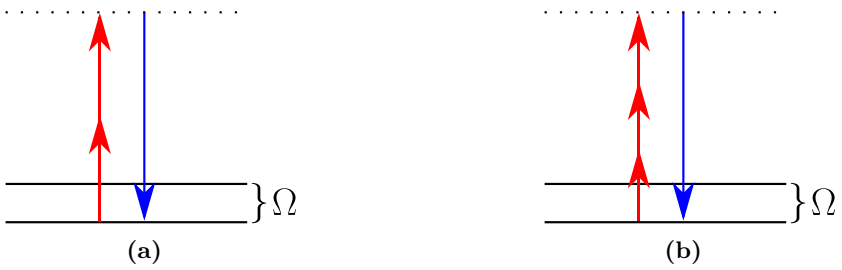

Figure 2.7: Energy level diagrams of SHG (a), and THG (b). Dashed line is a virtual energy level.

SHG and THG microscopy, similarly to CRS microscopy, does not require specimen staining and does not electronically excite the sample. SHG microscopy was first reported in 1986, on rat tail tendons [43]. Despite the reported poor resolution of around 50 µm this imaging technique quickly gained popularity and was developed rapidly. Nowadays, SHG imaging is used for ovary cancer detection [44], human tendon analysis [45], porcine heart imaging[46], etc. Similarly, THG microscopy nowadays is used for in vivo hamster oral cavity optical biopsy [47], in vivo imaging of mouse osteocytes [48] and in combination with SHG and two-photon fluorescence to image *Caenorhabditis elegans* cell structures in vivo [49], etc. In this work, SHG and THG imaging was performed in addition to CARS imaging using two different laser sources.

2.4 Molecular vibrations as mass-spring system

An external electric driving force that matches the resonant molecular frequency of the material affects optical properties which is a basis of CRS microscopy and makes it distinguishable from spontaneous Raman process. At the resonance the molecule will have a particular pattern of vibration called a mode shape which can be explained with a classical mechanics approach. In the literature, one of the most

common molecules used to demonstrate molecular vibrations is water [31], [50] but it is rarely explained how those mode shapes were obtained. Vibrational modes of this molecule will be derived by modeling it as a mass and spring system. The masses are the nuclei with core electrons, and the spring are coming from the energy of the outer electrons providing the chemical bond [29]. The spring with marked one-dimensional nodal points of the element are shown in Figure 2.8.

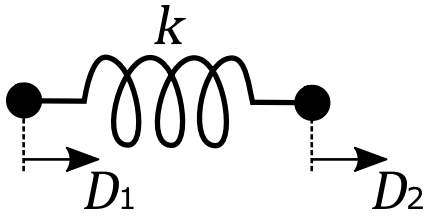

Figure 2.8: General one-dimensional spring diagram with two nodal points and their possible displacements D_1 and D_2. The term k is spring stiffness.

The force applied on the first node will be proportional to the distance that node one moves with respect to the second node. Similarly, force applied on second node will be proportional to the distance that node two moves with respect to the first node. Mathematically, this is expressed

$$\begin{cases} F_1 = kD_1 - kD_2 = k(D_1 - D_2) \\ F_2 = kD_2 - kD_1 = k(-D_1 + D_2)\,. \end{cases} \tag{2.16}$$

The spring equation can be expressed by using the matrix notation

$$\begin{bmatrix} k & -k \\ -k & k \end{bmatrix} \begin{bmatrix} D_1 \\ D_2 \end{bmatrix} = \begin{bmatrix} F_1 \\ F_2 \end{bmatrix}, \tag{2.17}$$

or more generally

$$\mathbf{K}_e \mathbf{D}_e = \mathbf{F}_e\,, \tag{2.18}$$

where the bold represent a matrix. $\mathbf{K}_e$ is called the stiffness matrix, $\mathbf{D}_e$ is a displacement vector and $\mathbf{F}_e$ is a force vector.

This is one of the most basic cases which could be obtained. Replacing end of the second node as a mass point m instead of a force application point, equation of motion can be derived for the new system. If the mass point is slightly displaced from the equilibrium and released, there is going to be kinetic and potential energy exchange. In this case, Lagrangian is the difference between kinetic and potential energy assuming that the damping force in negligible.

$$L = T - V\,. \tag{2.19}$$

The source of kinetic energy is the movement of the point mass and the source of potential energy is the elastic spring deformation. So the Lagrangian becomes

$$L = \frac{1}{2}(m\dot{x}^2 - kx^2)\,, \tag{2.20}$$

where $\dot{x}$ is the first time derivative of displacement x.

The Euler-Lagrange equation describing the motion is the following

$$\frac{d}{dt}\left(\frac{\partial L}{\partial \dot{x}}\right) - \frac{\partial L}{\partial x} = 0\,. \tag{2.21}$$

By inserting equation (2.20) into (2.21) the equation of motion for the spring-mass system becomes

$$m\ddot{x} + kx = 0\,, \tag{2.22}$$

which is a second order homogeneous differential equation which can be solved for the displacement x. For the water molecule model, which consists of only point mass and springs, the equation of motion will have the same type but only more degrees of freedom. For visualization, a diagram of water molecule diagram as presented in Figure 2.9.

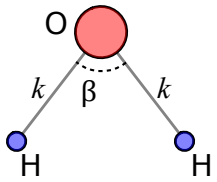

Figure 2.9: Water molecule representation. It is assumed that hydrogen and oxygen atoms are connected to each other through a link which can be modelled as a linear spring. Here: O, oxygen atom; H, hydrogen atom; k, spring stiffness; β, angle between hydrogen atoms which is 104°.

To derive final mode shapes, it is required to describe the stiffness matrix for the water molecule. The system can be split into separate parts and stiffness matrix needs to be constructed for each individual part. The left branch of the system contains two masses m_1 and m_2 connected by a spring as in Figure 2.10.

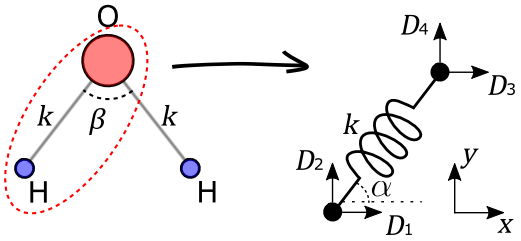

Figure 2.10: Hydrogen and oxygen atom bond modeled as a mass and a spring system. Here: m_1, mass of the hydrogen atom; m_2, mass of the oxygen atom; $D_{1,2,3,4}$, degrees if freedom 1, 2, 3 and 4; α, angle between the spring and the axis of reference.

Because of the angle between the spring and the reference axis x, the masses will move in plane when displaced. Two displacements for each node are required to describe this branch and requires to take the angle α into account. Thus, it requires to go from local element coordinates to global, as presented in Figure 2.11.

To fully describe the element in Figure 2.10, global displacement is transformed to local displacement and the corresponding force in local force is transformed into a force in global coordinates. The global component will be influenced by every single possible displacement in the spring and the corresponding force equation is:

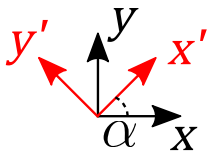

Figure 2.11: Global x and y coordinates marked in black together with local element coordinates x' and y' marked in red. the angle between them is α.

$$\begin{cases} F_1 = kD_1\cos^2\alpha + kD_2\cos\alpha\sin\alpha - kD_3\cos^2\alpha - kD_4\sin\alpha\cos\alpha \\ F_2 = kD_1\cos\alpha\sin\alpha + kD2\sin^2\alpha - kD_3\cos\alpha\sin\alpha - kD_4\sin^2\alpha \\ F_3 = -kD_1\cos^2\alpha - kD_2\cos\alpha\sin\alpha + kD_3\cos^2\alpha + kD_4\cos\alpha\sin\alpha \\ F_4 = -kD_1\cos\alpha\sin\alpha - kD_2\sin^2\alpha + kD_3\cos\alpha\sin\alpha + kD_4\sin^2\alpha \end{cases} . \quad (2.23)$$

or in the matrix form

$$k\begin{bmatrix} \cos^2\alpha & \cos\alpha\sin\alpha & -\cos^2\alpha & -\sin\alpha\cos\alpha \\ \cos\alpha\sin\alpha & \sin^2\alpha & -\cos\alpha\sin\alpha & -\sin^2\alpha \\ -\cos^2\alpha & -\cos\alpha\sin\alpha & \cos^2\alpha & \cos\alpha\sin\alpha \\ -\cos\alpha\sin\alpha & -\sin^2\alpha & \cos\alpha\sin\alpha & \sin^2\alpha \end{bmatrix}\begin{bmatrix} D_1 \\ D_2 \\ D_3 \\ D_4 \end{bmatrix} = \begin{bmatrix} F_1 \\ F_2 \\ F_3 \\ F_4 \end{bmatrix} . \quad (2.24)$$

The expression in the stiffness matrix can be simplified

$$k\begin{bmatrix} \mathbf{r} & -\mathbf{r} \\ -\mathbf{r} & \mathbf{r} \end{bmatrix}\begin{bmatrix} D_1 \\ D_2 \\ D_3 \\ D_4 \end{bmatrix} = \begin{bmatrix} F_1 \\ F_2 \\ F_3 \\ F_4 \end{bmatrix}, \text{where} \quad \mathbf{r} = \begin{bmatrix} \cos^2\alpha & \cos\alpha\sin\alpha \\ \cos\alpha\sin\alpha & \sin^2\alpha \end{bmatrix} . \quad (2.25)$$

The equations describe the relationship between the force and the displacements when element's local coordinates do not match the global coordinates. The same procedure can be repeated with the second branch of the water molecule. It can be done with the second branch of the water molecule since every parameter of the spring stays the same, except the angle. The whole water molecule model is presented in Figure 2.12.

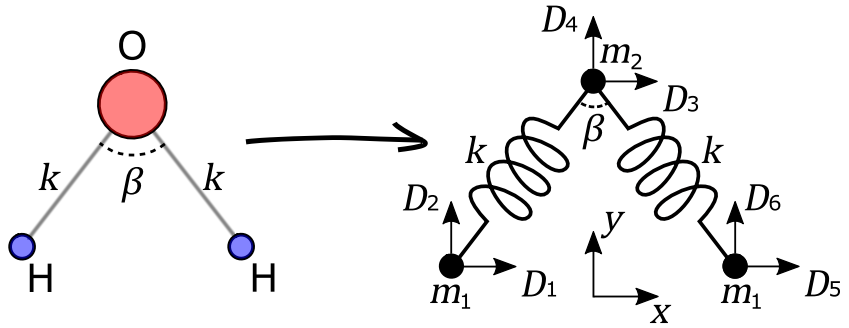

Figure 2.12: The water molecule model with forces between oxygen and hydrogen atoms.

The spring must be connected to prevent the model from falling apart. The connection between springs is ensured by performing stiffness matrix assembly as presented in Figure 2.13.

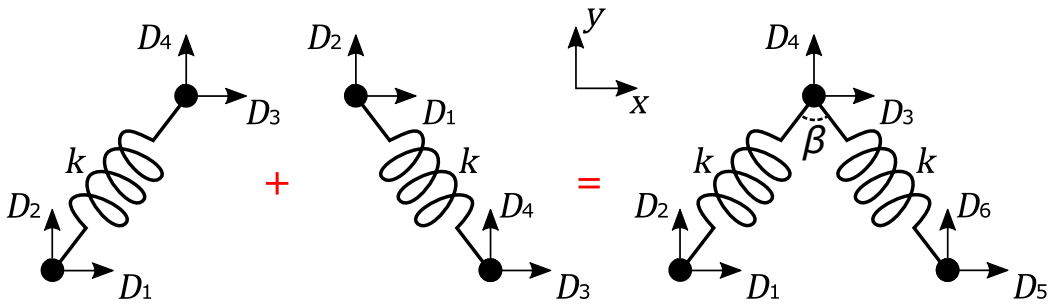

Figure 2.13: Springs can be described independently but they need to be combined by performing stiffness matrix assembly.

Figure 2.13 shows that assembly of displacements D_3, D_4 from the first element with displacements D_1, D_2 of the second element is required. The stiffness matrix allows to identify which variables contribute to the forces on the node with displacements D_3, D_4. This particular case is expressed

$$\boldsymbol{K} = k \left(\begin{bmatrix} \boldsymbol{r}_1 & -\boldsymbol{r}_1 & \mathbf{0} \\ -\boldsymbol{r}_1 & \boldsymbol{r}_1 & \mathbf{0} \\ \mathbf{0} & \mathbf{0} & \mathbf{0} \end{bmatrix} + \begin{bmatrix} \mathbf{0} & \mathbf{0} & \mathbf{0} \\ \mathbf{0} & \boldsymbol{r}_2 & -\boldsymbol{r}_2 \\ \mathbf{0} & -\boldsymbol{r}_2 & \boldsymbol{r}_2 \end{bmatrix} \right), \tag{2.26}$$

where $\boldsymbol{r}_{1,2}$ are angle contributions from springs 1 and 2 respectively.

The new stiffness matrix can be constructed by writing each contribution from each element. Blue color shows the contribution from the first spring element while the red color shows the contribution from the second spring element.

$$\mathbf{K} = k \begin{bmatrix} \cos^2\alpha & \cos\alpha\sin\alpha & -\cos^2\alpha & -\sin\alpha\cos\alpha & 0 & 0 \\ & \sin^2\alpha & -\cos\alpha\sin\alpha & -\sin^2\alpha & 0 & 0 \\ & & \cos^2\alpha+\cos^2\alpha & \cos\alpha\sin\alpha+\cos\alpha\sin\alpha & -\cos^2\alpha & -\cos\alpha\sin\alpha \\ & & & \sin^2\alpha+\sin^2\alpha & -\cos\alpha\sin\alpha & -\sin^2\alpha \\ & \text{sym.} & & & \cos^2\alpha & \cos\alpha\sin\alpha \\ & & & & & \sin^2\alpha \end{bmatrix}, \tag{2.27}$$

where sym. marks that the stiffness matrix is symmetrical around the diagonal.

The operation results in global stiffness matrix which includes multiple spring elements with arbitrary in-plane orientation. To make the water molecule model more realistic, a hydrogen bonds needs to be accounted between hydrogen atoms. The stiffness between oxygen and hydrogen atoms is assumed to be 797 Nm^{-1} which is 4.5 times stronger than the hydrogen-hydrogen bond [51]. The way to combine three individual springs to obtain water molecule model is presented in Figure 2.14

The updated stiffness matrix consisting of three springs is expressed by equation

$$\boldsymbol{K} = k \begin{bmatrix} \boldsymbol{r}_1+\boldsymbol{r}_3 & -\boldsymbol{r}_1 & -\boldsymbol{r}_3 \\ -\boldsymbol{r}_1 & \boldsymbol{r}_1+\boldsymbol{r}_2 & -\boldsymbol{r}_2 \\ -\boldsymbol{r}_3 & -\boldsymbol{r}_2 & \boldsymbol{r}_2+\boldsymbol{r}_3 \end{bmatrix}, \text{where} \quad \boldsymbol{r}_3 = \begin{bmatrix} \frac{10}{45} & 0 \\ 0 & 0 \end{bmatrix}. \tag{2.28}$$

which presents the final stiffness matrix. Since the goal is to determine the mode shapes of the molecule when it is displaced from the equilibrium, one has to assemble the global mass matrix of the structure. The mass is placed only on the nodes and

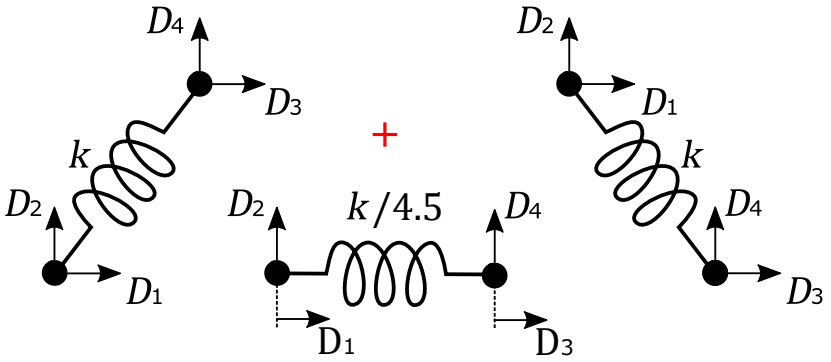

Figure 2.14: Elements used in the final water molecule model. Each spring represents a force between atoms; angled springs represent force between hydrogen and oxygen atoms while the parallel spring represents force between hydrogen atoms which is assumed to be 4.5 times weaker.

acts only locally without any influence on neighboring nodes. The mass matrix is written

$$\mathbf{M} = \begin{bmatrix} m_1 & 0 & 0 & 0 & 0 & 0 \\ 0 & m_1 & 0 & 0 & 0 & 0 \\ 0 & 0 & m_2 & 0 & 0 & 0 \\ 0 & 0 & 0 & m_2 & 0 & 0 \\ 0 & 0 & 0 & 0 & m_1 & 0 \\ 0 & 0 & 0 & 0 & 0 & m_1 \end{bmatrix}, \tag{2.29}$$

Equation (2.29) shows full mass matrix of the water molecule. By using equations (2.28) together with (2.29), an equation of motion for each node in the system is written

$$\mathbf{M}\ddot{\mathbf{x}} + \mathbf{K}\mathbf{x} = \mathbf{0}\,. \tag{2.30}$$

Mode shapes, which show how the molecule vibrates, are obtained by solving equation (2.30). It can be solved by assuming a periodic function as a solution

$$\mathbf{x} = \boldsymbol{\phi}\sin(\omega_i t)\,, \tag{2.31}$$

and the second derivative is then

$$\ddot{\mathbf{x}} = -\omega_i^2\boldsymbol{\phi}\sin(\omega_i t)\,. \tag{2.32}$$

Rewriting the equation of motion and dropping the sinusoidal term yields

$$(\mathbf{K} - \omega_i^2\mathbf{M})\boldsymbol{\phi} = \mathbf{0}\,. \tag{2.33}$$

The part $(\mathbf{K} - \omega^2\mathbf{M})$ cannot have an inverse, otherwise trivial solution is derived where $\boldsymbol{\phi} = \mathbf{0}$. The only way to have something else is when the determinant of $(\mathbf{K} - \omega^2\mathbf{M})$ is equal to 0, so the following equation needs to be solved

$$det(\mathbf{K} - \omega_i^2\mathbf{M}) = 0\,. \tag{2.34}$$

Solving equation (2.34) for ω_i and then substituting it into equation (2.33) allows to calculate $\boldsymbol{\phi}$ which is an unique mode shape for the particular resonant frequency ω_i. The values used for the calculations are provided in Table 2.2.

Symbol	Value	Description
m_1	$1.674 \times 10^{-27}\,\mathrm{kg}$	Mass of a hydrogen atom
m_2	$2.657 \times 10^{-26}\,\mathrm{kg}$	Mass of an oxygen atom
β	104.45°	Angle between hydrogen atoms
k	$797\,\mathrm{Nm}^{-1}$	Force constant between hydrogen and oxygen atoms

Table 2.2: Values used for the mode shape calculations.

By solving the system equation, mode shape solutions are calculated which are presented in Table 2.3.

$\omega_1 = 4258$	$\omega_2 = 3802$	$\omega_2 = 1364$	Natural frequency, (1/cm)
Values of mode 1	Values of mode 2	Values of mode 3	Coresponding degrees of freedom
-0.626	-0.558	0.356	D_1, first hydrogen, x direction
-0.326	-0.432	-0.608	D_2, first hydrogen, y direction
0.000	0.070	0.000	D_3, oxygen, x direction
0.041	0.000	0.077	D_4, oxygen, y direction
0.626	-0.558	-0.356	D_5, second hydrogen, x direction
-0.326	0.432	-0.608	D_6, second hydrogen, y direction

Table 2.3: Calculated water molecule resonant frequencies with corresponding relative displacements.

Table 2.3 provides relative motion between the nodes of the system. The solution can visualize them by plotting the vectors on the water molecule model. It is important to note that the movement of atoms is relative to each other and not absolute so the exact displacement is unknown. The visualization of mode shapes in Table 2.3 are presented in Figure 2.15. It is interesting to notice that the displacement of the oxygen atom is around 10 times smaller than the hydrogen atom because of it's mass.

Only three solutions are presented as other three solutions are at 0 frequency and are unphysical. Additionally, only 2D solution is provided where 3D solution would provide extra 3 vibrational modes. The calculated vibrational frequencies of water are higher than obtained experimentally and this is because real samples contain forces from other water molecules which are unaccounted in this model. Supplement forces makes the system less stiff which shifts all vibrational peaks to lower wavenumber region.

2.5 Ultrafast light sources

CRS microscopy requires pulsed light sources with high peak power for efficient non-linear interaction but low average power to prevent sample damage. Most of

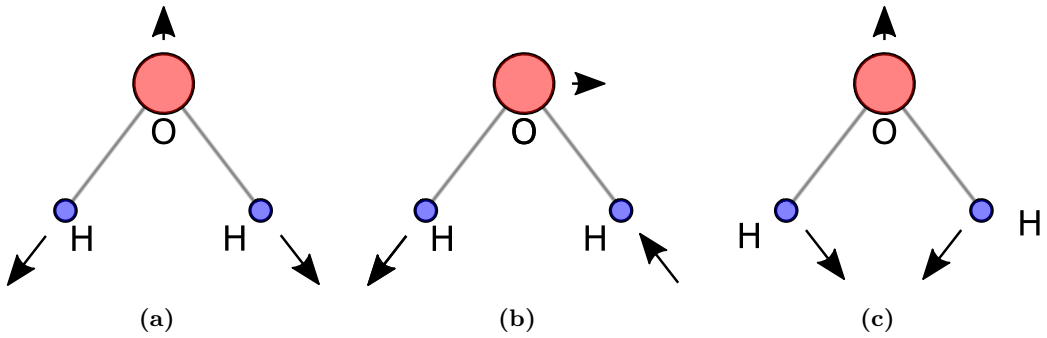

Figure 2.15: The first mode shape at 4258 cm^{-1}(a), the second mode shape at 3802 cm^{-1}(b) and the third mode shape at 1364 cm^{-1}(c) of a water molecule.

the technologies that result of non-linear transformation of a laser beams (light amplification by stimulated emission of radiation) like optical parametric amplifiers (OPA), optical parametric oscillators (OPO), optical parametric generators (OPG), second/third harmonic generators (S/THG), four-wave-mixers (FWM), Raman shifters, etc. have their own advantages and disadvantages. Therefore, it is important to distinguish between ultrafast technology devices and to know their best suited applications and limitations.

2.5.1 Pulsed lasers

A pulsed laser is a device which outputs coherent light pulses. The first ever laser was a ruby pulsed laser which used pump power modulation by pulsed excitation via flash lamps (gain switching) [52]. The technique was rapidly developed and soon, a more efficient technique called Q-switching was introduced where the cavity losses are switched.[53]. The main idea of Q-switching is to have a shutter in the cavity which allows to accumulate higher population inversion by preventing spontaneous lasing in the pump material and then opening the shutter which results in a pulsed behavior depleting the accumulated gain. Q-switching can be separated into active and passive mode, depending if the shutter is externally controlled (active), or controlled by the laser light itself (passive). One way to achieve active Q-switching is by using a Pockel's cell which changes the light polarisation, thus increases losses due to brewster angle elements, when external voltage is applied. Passive Q-switching can be achieved by a saturable absorber, which reduces absorption with increasing intracavity power. However, just purely by Q-switching, pulse duration has a limit in nanoseconds or picoseconds. To make pulses even shorter, a modelocking technique can be used which relies on constructive electric field interference when electric field components are in phase. One of the first demonstrations of modelocking came in 1964 and was demonstrated together with Q-switching [54]. A dye laser which was synchronously pumped and colliding pulse mode-locked was demonstrated in 1984 which used saturable absorber and was one of the main discoveries which led to semiconductor saturable absorber modelocking technology [55]. Nowadays, the simpliest and most used passive modelocking mechanism is utilizing a Kerr lens and a spatial filter: only high intensity light in the cavity is focused through a spatial filter while the less intense light is blocked. Intense light is focusing because it causes refractive index increase which are described by an equation $n = n_0 + n_2 I$ where n_0 is the refractive index, n_2 is the non-linear refractive index coefficient and I is the

intensity. The high intensity modelocked light has reduced losses and thus is the mode which lases. The drawback of Kerr modelocking is the difficulty to start the process as it relies on random interference of the many longitudinal cavity modes, to form a strong enough peak which then gets amplified. Additionally, it involves a shaker which ensures that more cavity modes are lasing, so that the interference can reach a high enough peak. A sketch illustrating Kerr lens used for modelock initiation is presented in Figure 2.16.

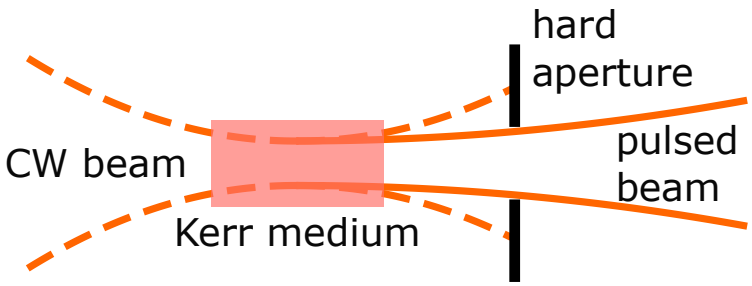

Figure 2.16: Sketch of a typical of a Kerr lens modelocking with a hard aperture. Only pulsed regime passes through the aperture as majority of the continuous wave regime is blocked. Beam sizes are not to scale.

A device working on such principle is called an oscillator and usually provides pulses with nJ energy and >70 MHz repetition rate. To get more energy into pulses without optical damage, a technique called chirped pulse amplification (CPA), can be applied [56]. The idea of CPA is to stretch pulses in time, amplify them and then recompress them to their original duration in order to reduce the peak intensity in the gain medium. Usually, such lasers work in kHz to few MHz regime with pulse energies of µJ to mJ with pulse duration of the order of 100 fs. The pulse amplification part is presented in Figure 2.17. Linearly polarized pulse from the stretcher passes trough a polarizing beamsplitter which transmits only a selected linear polarization and through half-waveplate together with Faraday's rotator which rotate the polarization by 45° each. After the pulse enters the amplification cavity by reflecting from the polarizing beamsplitter, Pockel's cell is turned on which works as a quarter-waveplate. In tandem with the already present quarter-waveplate, pulse is forced to oscillate between gain medium and two mirrors which amplifies the pulse. After certain amount of oscillations, Pockel's cell is switched into half-waveplate regime which rotates the linear polarization by 90° and allows the amplified pulse to exit the cavity by reflecting from the polarizing beamsplitter. Faraday's rotator together with half-waveplate does not change the net polarization of the returning amplified pulse and so the pulse is guided into the compressor by a polarizing beamsplitter.

2.5.2 Optical parametric devices

One of the most limiting factors of lasers is the tuning range limited by the gain medium. Even Ti:Sa lasers with broad spectrum can be tuned from around 700 nm to 1000 nm. Soon after the invention of the first laser in 1961, it was experimentally demonstrated that it is possible to change light wavelength through nonlinear interaction between material and light [57]. For the high intensity electric fields, the polarization acquires significant non-linear components and the induced polarization written as Taylor series

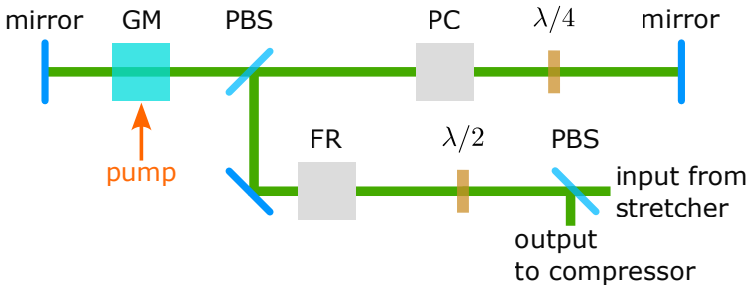

Figure 2.17: Sketch of a typical regenerative amplifier. Here: GM, gain medium; PBS, polarizing beamsplitter; PC, Pockel's cell; FR, Faraday's rotator; $\lambda/2$, half-waveplate; $\lambda/4$, quarter-waveplate.

$$P = \epsilon_0 \left(\chi^{(1)} E + \chi^{(2)} E^2 + \chi^{(3)} E^3 + ... \right) , \tag{2.35}$$

where ϵ_0 is the permittivity of free space; $\chi^{(n)}$ is the electric susceptibility of order n.

Assuming that the total electric field can be written as a sum of two distinct electric fields with different frequencies and looking only at the polarization up to the second order we have

$$\begin{aligned} E(t) &= \frac{1}{2} \left(A e^{-i\omega_1 t} + A e^{i\omega_1 t} \right) + \frac{1}{2} \left(B e^{-i\omega_2 t} + B e^{i\omega_2 t} \right) \\ &= \frac{1}{2} \left(A e^{-i\omega_1 t} + B e^{-i\omega_2 t} + \text{c.c.} \right) , \end{aligned} \tag{2.36}$$

where A and B are the amplitudes of the corresponding electric fields and c.c. is the complex conjugate.

By inserting equation (2.36) into (2.35) and including only first and second order susceptibilities we find

$$\begin{aligned} P = &\frac{1}{2} \epsilon_0 \chi^{(1)} \left(A e^{-i\omega_1 t} + B e^{-i\omega_2 t} + c.c. \right) + \\ &+ \frac{1}{4} \epsilon_0 \chi^{(2)} \left[2 \left(A^2 + B^2 \right) + A^2 e^{-i2\omega_1 t} + B^2 e^{-i2\omega_2 t} + \right. \\ &\left. + 2AB e^{-i(\omega_1 + \omega_2)t} + 2AB e^{-i(\omega_1 - \omega_2)t} + \text{c.c.} \right] . \end{aligned} \tag{2.37}$$

Equation (2.37) shows that the induced polarization consists of the non-linear $\chi^{(2)}$ part, which contains a constant value which is called optical rectification and it introduces new frequencies $2\omega_1$, $2\omega_2$, $\omega_1 - \omega_2$ and $\omega_1 + \omega_2$. Doubling the frequency of fundamental input beams ω_1 and ω_2 to $2\omega_1$ and $2\omega_2$ is called second harmonic generation (SHG), while generating new beams from mixing the fundamentals at frequencies $\omega_1 + \omega_2$ and $\omega_1 - \omega_2$ are called sum frequency generation (SFG) and difference frequency generation (DFG), respectively. Phase matching condition, which ensures that the wave vector difference between polarization and generated waves is zero, has to be met for the processes to accumulate constructively along the beam propagation, and achieve large conversion efficiencies. It is important to note that SHG cannot be generated in centrosymmetric structures.

2.5.2.1 Optical parametric amplifier (OPA)

An OPA is a single-pass device which splits the energy of an input photon into two lower energy photons called signal and idler. By meeting phase matching conditions it is possible to efficiently split a higher energy photon into two lower energy photons: $\hbar\omega_{\mathrm{p}} = \hbar(\omega_{\mathrm{S}}+\omega_{\mathrm{i}})$ where ω_{p}, ω_{S}, ω_{i} are the pump, signal and idler angular frequencies, respectively. Since the process is amplifying signal and idler it is important to seed signal and idler photons, as otherwise the process starts from vacuum fluctuations and a much higher total amplification is required in the system which can be done by using white-light continuum. The phase-matching condition can be fulfilled by a birefringent crystal which has a different refractive indices for fast and slow optical axes and signal and/or idler having different polarization to the pump. By changing the angle of the crystal, refractive index is changed and can lead to phase-matching condition. Depending on the pump wavelength and crystal used to fulfill the phase matching condition, it is possible to generate pulses with tuneability range of from 650 nm to 2500 nm. A simplified OPA diagram with birefringent phase-matching crystal is presented in Figure 2.18. One of the drawbacks is the μJ pulse energy requirement needed for self-phase modulation to be strong enough for white light generation to obtain the seed light. A consequence of pulse amplification is reduced pulse repetition rate. Since μJ pulses are required, it is often limited by the average power in the amplification stage in the oscillator as pulse has to attain substantial number of cycles in it before leaving. Higher repetition rate can also damage the setup.

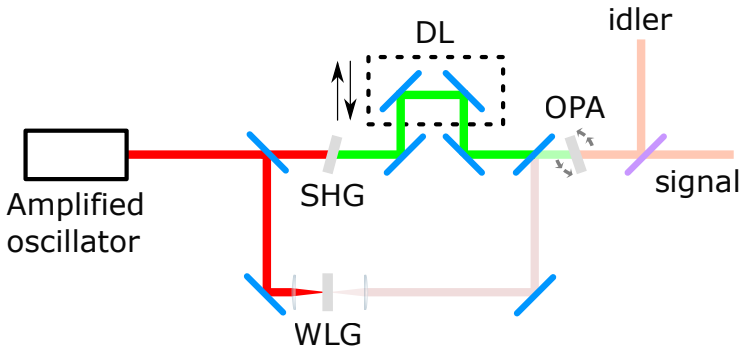

Figure 2.18: Sketch of an OPA. Here: SHG, second harmonic generation; DL, delay line; OPA, optical parametric amplification; WLG, white light generation by self-phase modulation. The OPA output is signal and idler pair.

2.5.2.2 Optical parametric oscillator (OPO)

Process inside the OPO are similar to the OPA and were first experimentally demonstrated in 1965 [58]. The difference from an OPA is the recycling of one of the OPO beams in a cavity, which allows the system, similar to a laser, to start from the vacuum fluctuations, and thus not needing white light generation. The first signal pulse is amplified in the cavity as it travels the same time as it requires to meet the next pulse from the oscillator so it works as an infinite pass OPA. After the amplification, 5% to 10% of the signal leaves the system while the remaining power allows shot-noise limited operation. A simplified OPO scheme is presented in Figure 2.19.

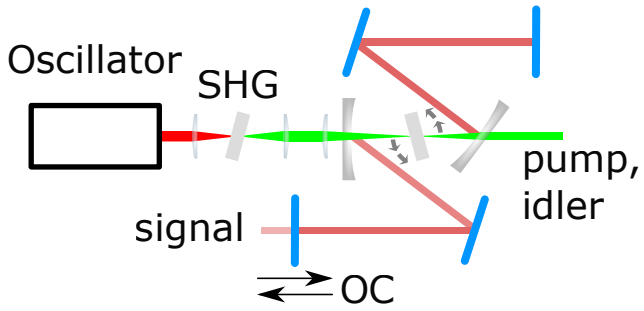

Figure 2.19: Sketch of an OPO. Here: SHG, second harmonic generation; OC, ouput coupler. The rotating part is indicating OPO crystal where only the signal is amplified. The SHG crystal is not compulsory for the OPO process and only depends on desired signal/idler pair wavelength.

The advantage of OPO is the ability to generate pulses with high repetition rate but with low energy so the repetition rate of the OPO is the same as in the oscillator. The general characteristics of oscillator, amplifier oscillator, OPA and OPO are presented in Table 2.4.

	Repetition rate	Pulse energy	Tuneability	Noise
Oscillator	> 30 MHz	nJ	None	Shot-noise limited
Amplified oscillator	kHz to few MHz	μJ	None	Above shot-noise
OPA	kHz to few MHz	μJ	Wide	Above shot-noise
OPO	> 30 MHz	nJ	Wide	Shot-noise limited

Table 2.4: Devices that generate coherent pulsed light.

2.6 Chirped optical pulses

Vibrational resonances in typical biological samples have linewidths in the 10–50 cm^{-1} range, corresponding to vibrational coherence times in the picosecond range. Achieving such spectral resolution accordingly requires excitation and probing pulse durations in the picosecond range. As the source used in the present work delivers around 150 fs pulses, we implemented spectral focusing [59, 60] to stretch the pulses by the dispersion of the refractive index $n(\lambda)$ in optical media. The spectral focusing scheme is based on the idea of temporally stretching broad-band laser pulses in time and controlling their temporal overlap with a delay line which allows to target specific narrow vibration frequencies. Stretching pulses temporally is performed by adding glass blocks to the setup and spectral focusing additionally provides an ability to perform spectral scan by using a delay line without the need of tuning the OPO which is usually slower.

One of the most common approximations for the ultrashort laser pulse in the femtosecond time scale is assuming a Gaussian or a sech^2 shape the latter being more common for optical solitons and most kerr-lens modelocked lasers. Here we assume a Gaussian shape which can be expressed as

$$f(x) = a \exp\Big(- \frac{(x-b)^2}{2c^2} \Big), \tag{2.38}$$

where a is the peak amplitude, b peak position and mean value and c is the standard deviation.

Knowing the mathematical description of a Gaussian function, one can construct the carrier envelope for the pulse in the time domain

$$\mathcal{E}(t) = \mathcal{E}_0 \exp\Big(\frac{-t^2}{2\sigma^2}\Big)\,, \tag{2.39}$$

where $\mathcal{E}_0$ is the amplitude of the envelope, t is time variable centering the peak around 0 and σ is the standard deviation.

We also note that it is inconvenient and not intuitive to use standard deviation σ in the equation. A more intuitive and more frequent method is to describe the Gaussian shape by using full width half maximum (FWHM). To derive the relation between standard deviation and FWHM we evaluate our envelope to half the amplitude and calculate the width of it:

$$\frac{1}{2}\mathcal{E}_0 = \mathcal{E}_0 \exp\Big(\frac{-\tau_{\mathrm{EF}}^2}{2\sigma^2}\Big)\,, \tag{2.40}$$

from equation (2.40) we solve for electric field FWHM τ_{EF} which yields

$$\tau_{\mathrm{EF}} = 2\sigma\sqrt{2\ln 2}\,. \tag{2.41}$$

Substituting value derived in (2.41) into (2.40) we obtain the envelope equation

$$\mathcal{E}(t) = \mathcal{E}_0 \exp\Big(\frac{-4\ln(2)}{\tau_{\mathrm{EF}}^2}t^2\Big)\,. \tag{2.42}$$

However, the FWHM of the electric field is not practical since experimentally we measure pulse intensity so it is more convenient to write in terms of intensity duration. We know that the intensity is proportional to the electric field squared which will lead to an extra factor of 2 in the exponent. Therefore, there is going to be a factor of 2 difference between electric field FWHM and intensity FWHM. Electric field envelope with intensity FWHM value is presented in (2.43).

$$\mathcal{E}(t) = \mathcal{E}_0 \exp\Big(-\frac{2\ln(2)}{\tau_{\mathrm{F}}^2}t^2\Big)\,, \tag{2.43}$$

where τ_{F} is the pulse intensity FWHM value.

To correctly describe the electric field one has to take the rapidly varying carrier frequency into account.

$$E(t) = \frac{1}{2}\mathcal{E}(t)\exp\Big(i(\omega_0 t + \phi(t))\Big) + \text{c.c.}\,, \tag{2.44}$$

where ω_0 is the central frequency of the electric field, $\phi(t)$ is a varying phase component.

There exist a relationship between the temporal width of the pulse and its spectrum called time-bandwidth product which states that the pulse duration is limited by its spectrum and the shortest duration is present when all electric field components are in phase. This feature comes from the Fourier transform which relates time domain and frequency domain of a function and is expressed

$$x(\omega) = \int_{-\infty}^{\infty} x(t)\mathrm{e}^{-i\omega t}dt\,, \tag{2.45}$$

where $x(\omega)$ is a function in the frequency domain and $x(t)$ is a function in the time domain.

Similarly, by knowing a function in the frequency domain, one can apply the inverse Fourier transform and obtain function in the time domain

$$x(t) = \frac{1}{2\pi} \int_{-\infty}^{\infty} x(\omega) \mathrm{e}^{i\omega t} d\omega \,. \tag{2.46}$$

The relationship between time and frequency domains through Fourier transform is demonstrated in Figure 2.20 where a spectrally limited pulse with 120 fs and 250 fs intensity FWHM and center wavelength of 800 nm are shown in time and energy domains. The shorter the pulse in the time domain—the wider the spectrum and vice-versa. Note, that the electric field amplitude is plotted.

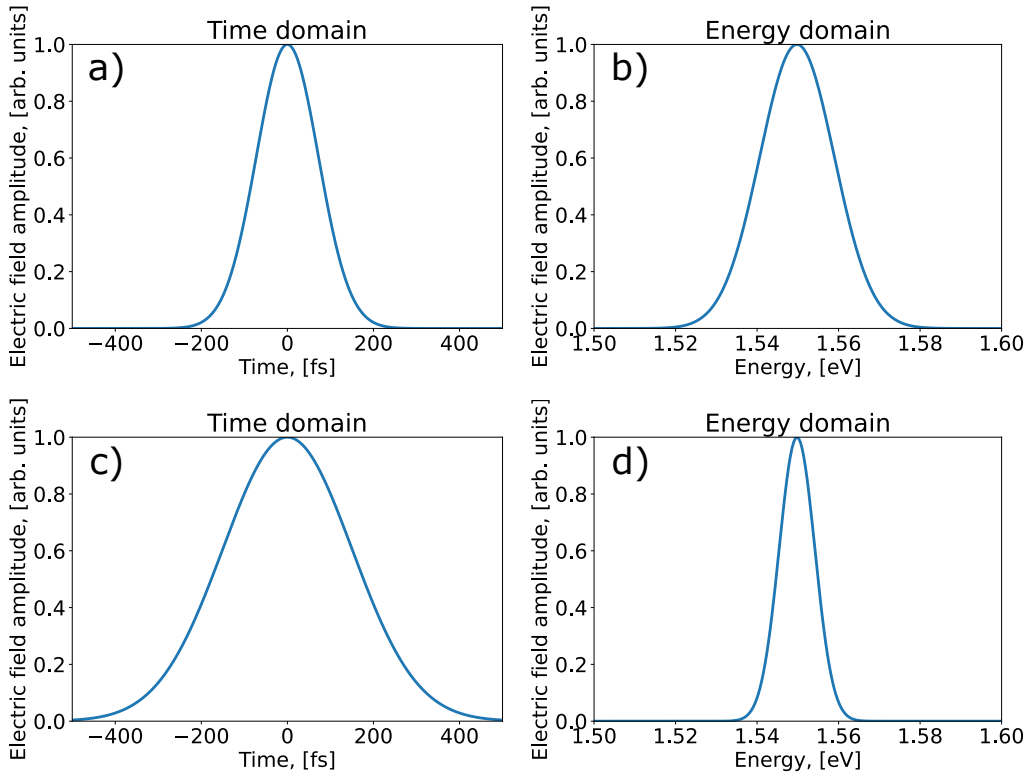

Figure 2.20: Spectrally limited pulses with 120 fs and 250 fs intensity FWHM in time a), c) and energy b), d) domains respectively.

The phase of a laser pulse can be time-varying and the variation of the phase is related to the instantaneous angular frequency ω

$$\omega = \frac{d}{dt}\phi(t) \,. \tag{2.47}$$

Equation (2.47) indicates that to have a linearly varying instantaneous angular frequency with time, which is called a linear chirp, the phase has to be defined by a second order polynomial. In this case, the instantaneous angular frequency is defined by equation (2.48)

$$\frac{d}{dt}\phi(t) = \omega_0 + bt \,, \tag{2.48}$$

where b is the linear chirp parameter.

The final electric field equation which takes into account instantaneous frequency definition in equation (2.47) and (2.48) is presented in (2.49):

$$E(t) = \frac{1}{2}\mathcal{E}(t)\exp\left(i\left(\omega_0 + \frac{bt}{2}\right)t\right) + \text{c.c.} \tag{2.49}$$

An unchirped, spectrally limited intensity FWHM 150 fs pulse and the same pulse but with applied 10800 fs^2 linear chirp are presented in Figure 2.21.

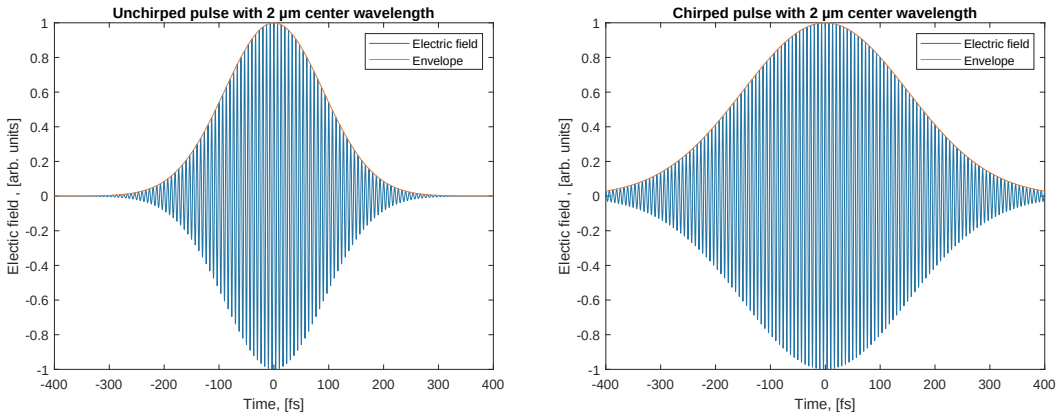

(a) **(b)**

Figure 2.21: Unchirped spectrally limited 150 fs pulse (a) and the same pulse but chirped to 250 fs (b). Center wavelength was set to 2 µm.

Just by providing intensity as a function of time it is impossible to know if the pulse was chirped or not. To overcome this problem a Wigner-Ville distribution can be calculated which is defined as

$$W = \int_{-\infty}^{\infty} E\Big(t + \frac{s}{2}\Big)E^*\Big(t - \frac{s}{2}\Big)\mathrm{e}^{-i\omega s}ds\,, \tag{2.50}$$

where E^* is the complex conjugate of the electric field $E(t)$ and s is the delay time over which the Fourier transform is done.

The Wigner-Ville distribution indicates the intensity profile and the integral of $W(\omega, t)/\omega$ provide temporal intensity curve. It is interesting to observe that the shape of the plot after chirping is stretched in time and has an angle to the time axis. The slope of the line is called the linear chirp parameter. The Wigner-Ville distributions are useful since they allow to visualize the field in a more intuitive way when linear chirp is applied.

The theoretical pulse description does not explain how to control the chirp. One of the easiest ways is by adding a dispersive material into the beam path as it is cheap, easy to setup and stable. To calculate the chirp by propagation through a block of dispersive material, we start with the Sellmeier equation modeling the refractive index of a material as a function of wavelength:

$$n^2(\lambda) = 1 + \sum_{i=1\ldots3}\frac{B_i}{1 - C_i/\lambda^2}\,, \tag{2.51}$$

where B_i, C_i are material constants.

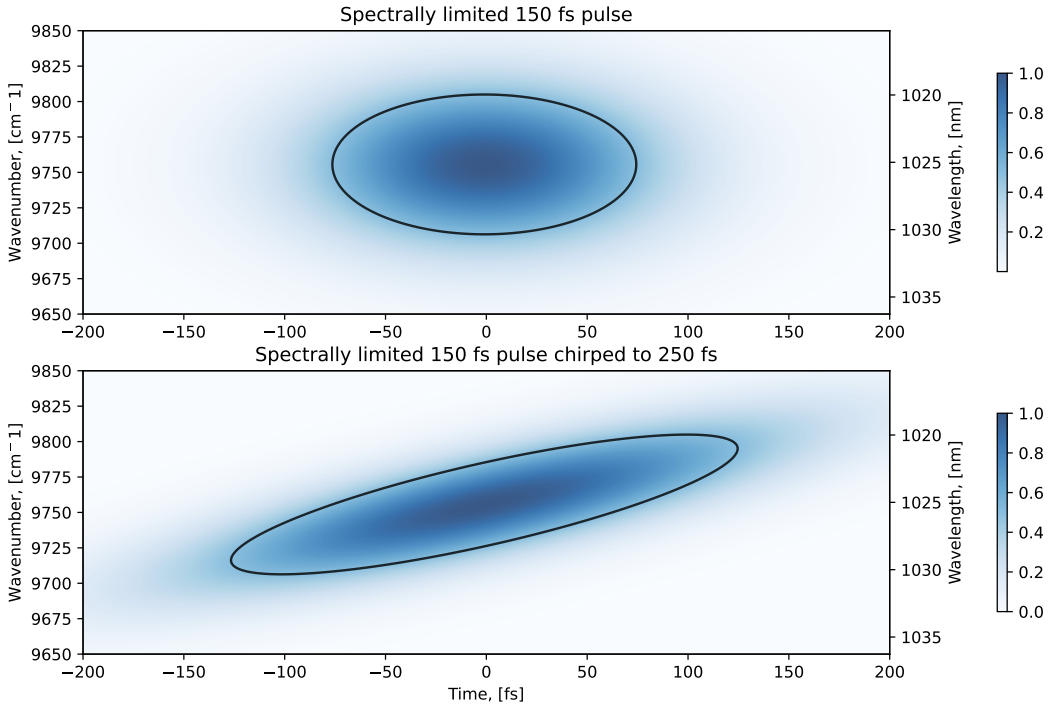

Figure 2.22: Wigner-Ville distribution of 1025 nm center wavelength laser pulses with 150 fs intensity FWHM before and after 10800 fs^2 linear chirp which chirps it to 250 fs. The black line indicates plot values which are half of the maximum value and correspond to the FWHM.

The group velocity, describing the wave packet envelope velocity, is given by $v_g \equiv \mathrm{d}\omega/\mathrm{d}k$, and group velocity dispersion (GVD) parameter is

$$k'' \equiv \frac{\mathrm{d}}{\mathrm{d}\omega}\left(\frac{1}{v_g}\right). \tag{2.52}$$

THe Sellmeier equation (2.51) provides refractive index as a function of wavelength while the group velocity is defined in angular frequency. To change the variable, we start by defining the angular wavenumber $k \equiv \omega n(\omega)/c$ and differentiating equation (2.52).

$$k'' = \frac{\mathrm{d}}{\mathrm{d}\omega}\left[\frac{1}{c}\left(n + \frac{\mathrm{d}n}{\mathrm{d}\omega}\omega\right)\right], \tag{2.53}$$

where c is the speed of light.

Using angular frequency ω is related to a wavelength in vacuum $\lambda = 2\pi c/\omega$, we can change the differentiation variables by applying the chain rule. The derivative with respect to the angular frequency can be expressed as

$$\frac{\mathrm{d}}{\mathrm{d}\omega} = \frac{\mathrm{d}}{\mathrm{d}\lambda}\frac{\mathrm{d}\lambda}{\mathrm{d}\omega} = \frac{-\lambda^2}{2\pi c}\frac{\mathrm{d}}{\mathrm{d}\lambda}, \tag{2.54}$$

and by combining (2.54), (2.53) we arrive

$$k'' = \frac{\lambda^3}{2\pi c}\frac{\mathrm{d}^2 n}{\mathrm{d}\lambda^2}. \tag{2.55}$$

Calculated GVD values of dense flint glasses N-SF66 and N-SF57 are presented in Figure 2.23.

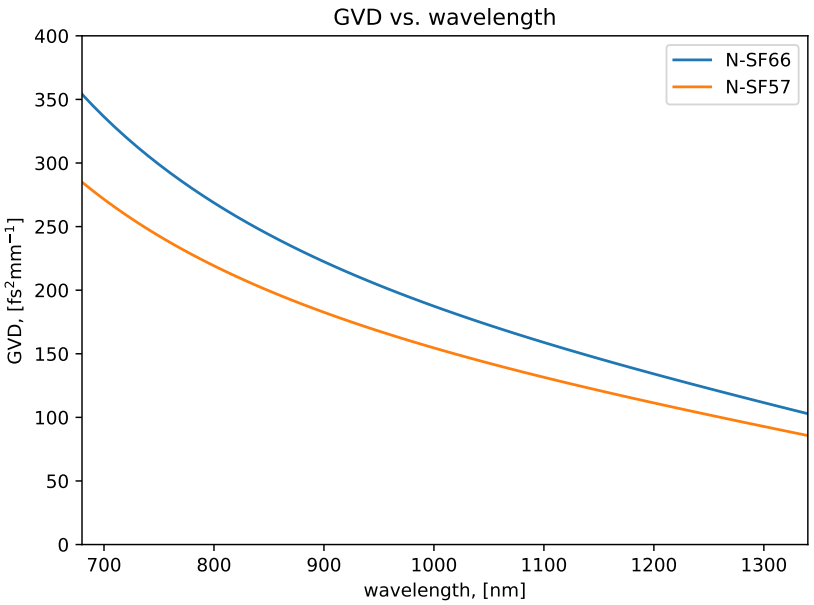

Figure 2.23: GVD versus wavelength of dense flint materials used to chirp femtosecond pulses.

Assuming that the material used is homogeneous, calculating group delay dispersion (GDD) is simply integrating through the length of a material:

$$g = \int_0^L k'' dl = k'' L \tag{2.56}$$

By knowing the material used and its length in the optical path it is possible to calculate how much linear chirp is added and the pulse final duration [61]. It can be calculated by using (2.57).

$$t_{\mathrm{f}} = t_0 \sqrt{1 + a}\,, \tag{2.57}$$

where t_f is final pulse intensity FWHM, t_0 is initial pulse intensity FWHM.

Variable a is a dimensionless chirp parameter and is expressed

$$a = \left(4 \ln(2) \frac{g}{t_0^2}\right)^2 , \tag{2.58}$$

To avoid having a constants in equation (2.43) and make calculations easier, pulse duration is sometimes expressed

$$\tau_G = t_f \sqrt{2 \ln(2)}\,. \tag{2.59}$$

Since linear chirp parameter is defined

$$b = \frac{2a}{\tau_G^2}\,, \tag{2.60}$$

combining equations (2.60, 2.59, 2.58, 2.57) yields linear chirp parameter in spectral units

$$b = \frac{8g}{c\pi\left(16g^2 + t_0^4/\ln^2(2)\right)}\,. \tag{2.61}$$

The linear chirp parameter is an important value to consider as the most optimal spectral resolution is when pump and Stokes beam have the same b value. Since pump and Stokes beams have different wavelengths, they will experience different amounts of dispersion after traveling through the same amount of glass which will lead to non-optimal spectral resolution. Additionally, having the same pump and Stokes pulse duration at the sample does not necessarily mean the spectral resolution is going to be optimal because pulses can obtain different amount of chirp and reach the same final duration because of their different spectra.

Chapter 3

Noise sources in CRS signals

Noise determines the detection limits and the precision of any quantification. Therefore, it is important to understand the sources of noise and how to minimize them. Techniques explaining how to measure laser source noise can be found in the literature [1, 62]. Sources of noise in the detection of radiation power can be split into four main categories: dark noise which is mainly due to thermal excitations in the photodetector and signal amplifiers, excess noise which is due to the signal amplification within some detectors such as photomultipliers or avalanche photodiodes detector by the randomness of carrier multiplication, shot noise, which is due to the quantum nature of light, and classical laser noise which is caused by classical fluctuations of the laser source such as by temperature variations, vibrations, electrical fluctuations, etc.

3.1 Types of noise

3.1.1 Dark noise

Dark noise is present independent of the light power on the detector. For detectors that use internal or external photoelectric effect, it is caused by the shot noise of the detector dark current (due to thermal excitations, semiconductor structure, material doping, etc.) and Johnson-Nyquist thermal noise of resistors and other conductive elements such as transistors in the electronic amplification circuits [63, 64]. The Johnson-Nyquist thermal noise root mean-squared (RMS) is expressed:

$$i_{rth} = \sqrt{\frac{4k_B T}{R}\Delta f}\,, \tag{3.1}$$

where i_{rth}, Johnson-Nyquist noise RMS current; k_B, Boltzmann constant; T, temperature in Kelvin; R, resistance; Δf, frequency bandwidth.

The shot noise RMS of dark current is expressed:

$$i_{rd} = \sqrt{2qi_d\Delta f}\,, \tag{3.2}$$

where q is the electron charge and i_d is the dark current.

The total dark noise is expressed by linearly combining Johnson-Nyquist current in equation (3.1) with shot noise value of the dark current (3.2)

$$i_{tdn} = i_{rth} + i_{rd}\,. \tag{3.3}$$

For SRS, dark noise is mainly due to the Johnson Nyquist noise in the electronic amplification of the diode detectors, used to detect the transmitted beams. Importantly, SRS requires the detectors to be able to cope with mW of power and have a dark noise below the shot noise, which is in the pW range. For CARS, dark noise is more important as the detected light power is weak, usually in the pW range, but it allows the use of photomultiplier tubes or avalanche photodiodes which exhibit carrier multiplication, reducing the importance of noise in subsequent electronic amplification. Dark noise is usually following the detector response frequency dependence.

3.1.2 Excess noise

Devices like photomultipliers and avalanche photodiodes which multiply the electrons generated by the external or internal photoelectric effect by accelerating these electrons by a high voltage followed by impact ionization experience gain noise. It is noise which is intrinsic to the photodetector and occurs because of the randomness in the gain process. Excess noise can be countered by implementing a photon counting scheme, or single photon saturation of amplification possible in photomultiplier at very high gains. However, these are limiting the detectable photon rates to about 10^7 Hz, which is limiting for CARS signals which are typically in the range from 10^6 to 10^9 Hz.

The mean number of electrons at the emission N_u can be calculated by knowing average gain value $\bar{G}$ and mean value of primary electrons N_p

$$N_u = \bar{G} N_p \,. \tag{3.4}$$

The relative variance at the output is then defined

$$\nu_u^2 = \frac{\sigma_u^2}{N_u^2} = \nu_p^2 + \frac{\nu_G^2}{N_p} = \frac{1}{N_p}\left(1 + \nu_g^2\right) \,. \tag{3.5}$$

Combining equations (3.4) and (3.5) leads to variance equation

$$\sigma_u^2 = \sigma_p^2 \bar{G}^2 \left(1 + \nu_g^2\right) \,, \tag{3.6}$$

where σ_p^2, variance at the input; ν_g^2, normalized variance of the gain. Therefore, the RMS current is

$$i_{re} = \sqrt{\sigma_p^2 \bar{G}^2 \left(1 + \nu_g^2\right)} \,. \tag{3.7}$$

where $\left(1 + \nu_g^2\right)$ is excess noise factor.

3.1.3 Shot noise

Light absorbed by the detector via the photoelectric effect consists of individual photons, which arrive randomly. Therefore, the number of photons in a constant light beam measured over two time periods of identical duration will differ. Given the average power, corresponding to average number of photons per unit time γ, the actual number of photons in each unit time will be a random number obeying Poissonian distribution with the mean equal to γ as presented in (3.8)

$$N = \frac{\gamma^k e^{-\gamma}}{k!}, \tag{3.8}$$

where N is a probability to find k photons and $k \in \mathbb{N}$.

The shot noise RMS is $\frac{1}{\sqrt{\gamma}}$ which means that increasing the average number of photons increases the shot noise RMS value but decreases the relative variance. The photocurrent created by the photoelectric effect shows the same randomness current fluctuation, due to randomness, is called shot noise which is inherent to photon detection [63]. This implies that even an ideally-constructed SRS system is going to have a shot noise limit that is independent from the technology used [1]. However, to overcome this problem, squeezed light can be used which can surpass intensity shot noise under selected conditions but increase phase noise and requires very low losses between the squeezed light source and the detection of the SRS signal [65].

3.1.4 Classical fluctuations

Laser parameters that are fluctuating over time give rise to classical noise. Relative intensity noise (RIN) describes the noise power distribution over frequency relative to the average DC power. By definition it is the ratio of the mean-squared noise power over a given frequency bandwidth divided by the square of the average power [62].

Ultrafast pulsed lasers are commonly used for SRS [66]. They are attractive because high peak intensities can be reached with low average power which is desired for most of the samples. Another advantage is the possibility to chirp the pulse which can be delayed for rapid SRS frequency tuning. Continuous wave (CW) lasers can also be used for specific SRS applications [67]. CW lasers are less complex and cheaper but they reduce SRS signal strength and they need a single longitudinal mode for low intensity noise. However, they are not well suited for biological applications because of the bad signal to sample damage ratio. Both types of laser sources may exhibit classical noise for CRS applications

Fiber lasers are usually noisier than free-space lasers because of the amplified spontaneous emission which provides higher power but also amplifies the shot noise. Noise can be even larger for harmonically mode-locked fiber oscillators as there are multiple pulse oscillations [68]. A comparison between SRS systems used in [1], [2] and commercially available Yb based OPO system can be seen in Figure 3.1. It shows that a solid state Ti:Sa and Yb OPOs reaches shot noise limit at around 2 MHz in Figure 3.1a, 3.1c when 5 mW and 3 mW detection power was used. The shot noise limit is around 4 MHz in Figure 3.1b with 28 mW diode power for the Ti:Sa system. In both cases, shot noise cannot be reached using fiber lasers which makes them less suitable for SRS imaging. Another study compared SRS with CARS microscopy and reported SRS noise of 1.5×10^{-8} $/\sqrt{\text{Hz}}$ which is close to the estimated shot-noise limit of 1.1×10^{-8} $/\sqrt{\text{Hz}}$ for 2.8 mA photocurrent [69].

In addition, classical noise is influenced by $1/f$ noise which arise due to low frequency drifts. Due to this noise, it is more convenient to detect the signal at a high frequency where $1/f$ noise is negligible. Noise in SRS applications can be reduced with a balanced detection scheme which records the intensity of the laser beam before and after the sample. Then, by using a variable gain amplifier and subtracting reference from the signal, allows to reach otherwise unapproachable limit which is 3 dB above shot noise since two detectors are used [2]. It was shown

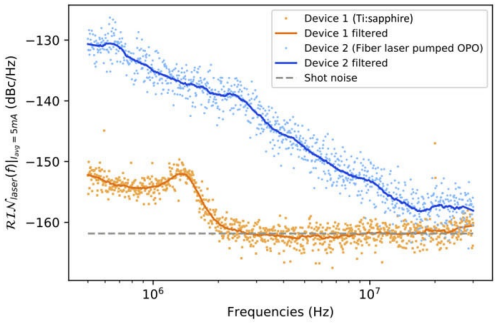

(a)

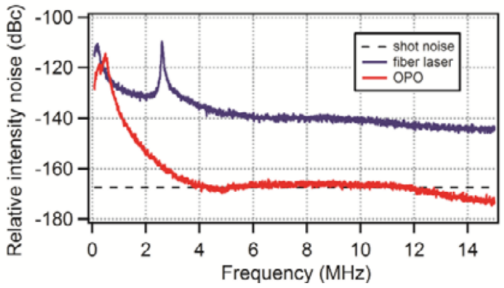

(b)

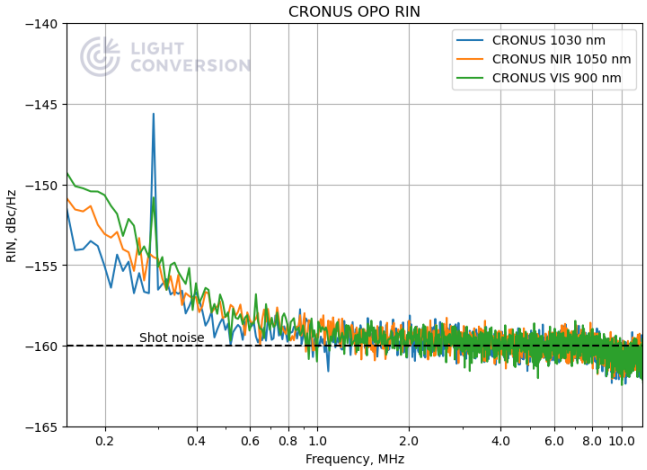

(c)

Figure 3.1: Experimental RIN results (a) from [1], RIN results (b) taken from [2] and RIN results of a commercially available Yb based OPO (c) with measurement procedure taken from [1].

that boxcar averaging method is better suited than lock-in detection when low duty cycles are used and can give the same SNR ratio with half integration time [70].

3.2 Noise performance of two light sources

To compare two commercially available laser sources with different gain material, a CRONUS-2P system was brought to Cardiff University and was tested in the already existing CRS setup. The results were compared with the on-site Ti:Sa system. The CRONUS-2P system was a 77 MHz Yb oscillator with its SHG beam pumping two optically-synchronized OPOs providing two independently tuneable outputs ranging from 680 to 960 nm and 960 to 1300 nm together with one fixed channel at 1025 nm (CRONUS-2P, Light Conversion). The pulse duration from all three channels was around 150 fs. The Ti:Sa laser source was 100 fs duration, 820 nm center wavelength 80 MHz oscillator (Mai Tai, Spectral Physics) pumping with its SHG beam an OPO (Inspire, Spectral Physics) providing signal-idler pair output together with a second harmonic of the oscillator beam.

3.2.1 Experimental setup

The setup used to compare laser source performance in CRS microscopy at Cardiff University is presented in Figure 3.2.

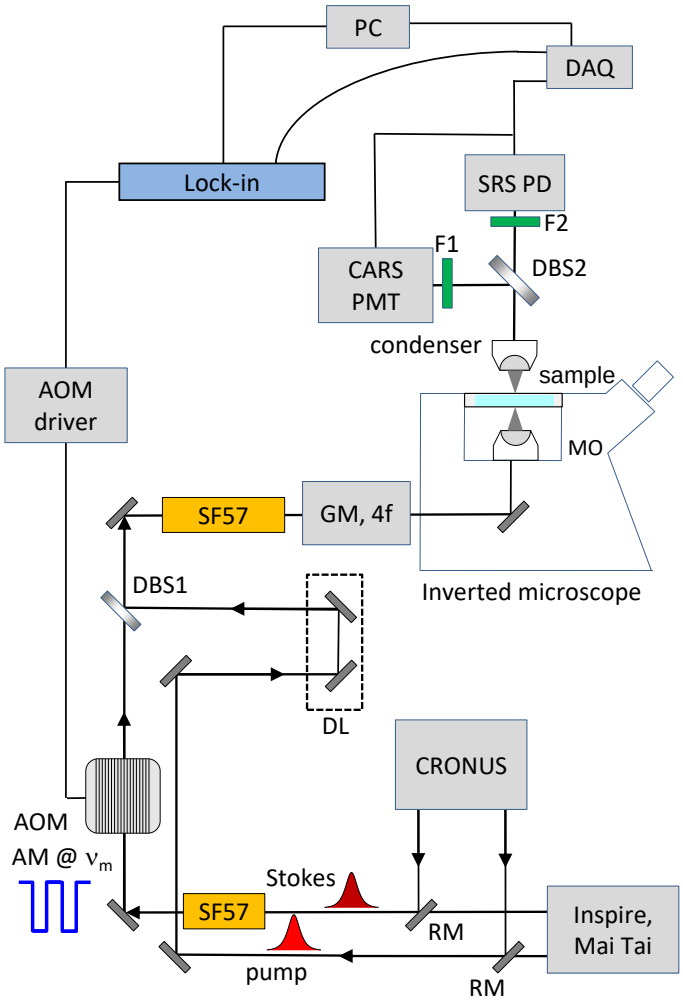

Figure 3.2: Sketch of the setup used for the experiments. Here: RM, removable mirrors; SF57, glass blocks used for pulse chirping; AOM, acousto-optic modulator; DL, delay line; DBS1,2, dichroic beam splitter; GM 4f, galvo mirrors with a 4f system; MO, microscope objective; F1,2, filters; DAQ, data acquisition unit.

The Stokes pulse travels through a glass block (SF57) and is amplitude modulated at 2.5 MHz by an acouto-optic modulator (AOM). Both pulses are recombined by a dichroic beam-splitter (DBS1) and travel through another glass block (SF57). They are coupled into a scanning microscope by galvo mirrors to spatially scan the beam and a 4f system. The beams are focused onto the sample by a 60×, 1.27 NA objective (Nikon CFI Plan Apochromat lambda series MRD70650) and collected by a 1.34 NA oil condenser. The generated CARS signal is guided to a photomultiplier tube (PMT) by a second dichroic beam splitter (DBS2) and the excitation pulses are filtered by a band-pass filter (F1). The remaining Stokes is filtered by a band-pass filter (F2) and SRS signal at a pump frequency is detected by a SRS photodetector (S6976, Hamamatsu). The SRS photodiode is equiped with a home-built resonant circuit at 2.5 MHz with resonant impedance of 10 kΩ while the DC impedance is

3.6 Ω. The resonance quality factor is about 10 followed by a 10× voltage amplifier. The signal is sent to a data acquisition unit (DAQ) to measure the DC signal, and to the lock-in amplifier for demodulation. The reference signal required for demodulation is created in the lock-in and is driving the AOM modulation taken from an AOM. The temporal pulse overlap is controlled by a motorized delay line (DL). Switching between laser sources was enabled adding removable mirrors (RM) which make the beam path for both systems similar so that timing between the pulses for both sources is within the range of the pump delay stage. To allow faster tuning and better spectral resolution, a spectral focusing scheme with dense flint glass (SF57) was applied [71, 72].

3.2.2 Noise measurements

In the experiments, pump noise was characterized as the setup works by detecting stimulated Raman loss of the pump which is called here SRS noise. The pump and Stokes wavelengths were set to 820 nm and 1097 nm respectively for both sources. To prepare a thin polystyrene film sample, PS toluene solution was drop cast to form the PS drop of some mm diameter and a few 10 µm height, and the drop is encapsulated in an imaging gasket of 120 µm height, filled with water. The sample with a Raman peak at 3050 cm^{-1} was placed over the objective for signal generation. For noise measurements, SRS signal was recorded when there was no temporal overlap between pump and Stokes pulses. Measurements were taken for different pump power and thus diode current was controlled using a power attenuator consisting of a half-wave plate and a polarizer. The data sampling period for CRONUS-2P system was 0.1 ms while for Inspire it was 1 ms. Note, the sampling period mismatch was due to human mistake which led to incorrect parameter selection during measurements but this does not influence the end results as they were normalized to root bandwidth. Since detecting photons on the SRS photodetector obbey Poissonian distribution of the coherent light, plotting photodetector voltage against number of occurrences produces a statistical distribution of the voltage. Increasing number of detected photons makes the distribution approach Gaussian distribution. It can be used to calculate RMS value by fitting Gaussian function $f(x) = \exp\left(\frac{-(x-\bar{x})^2}{2\sigma^2}\right)$ where $\bar{x}$ is the average and the standard deviation (σ) is the RMS. By fitting a Gaussian function and then calculating RMS is less sensitive to the data outliers than directly calculating the RMS of the data. Such fit is demonstrated in Figure 3.3 where artificial data was generated with 1000 samples draw from the Gaussian distribution ranging from -10 to 10 with 30 bins. The standard deviation and average value were selected to be 3 and 0 respectively. The outliers are generated at values -7, -2, 7, 10. Directly calculating RMS yields RMS value 3.44 while calculating RMS from the fit yields 3.14 which is closer to the ground truth.

The experimental RMS value is then divided by the square root of the sampling bandwidth to obtain the bandwidth-independent white noise. The obtained data was fitted with the function:

$$f(I) = \sigma\sqrt{\left(\frac{I}{P_0}\right) + \left(\frac{I}{P_1}\right)^2}, \tag{3.9}$$

where I is the photocurrent.

Since shot noise is rising with the square root of intensity while laser noise is linearly proportional, term P_0 expresses shot noise while term P_1 expresses laser

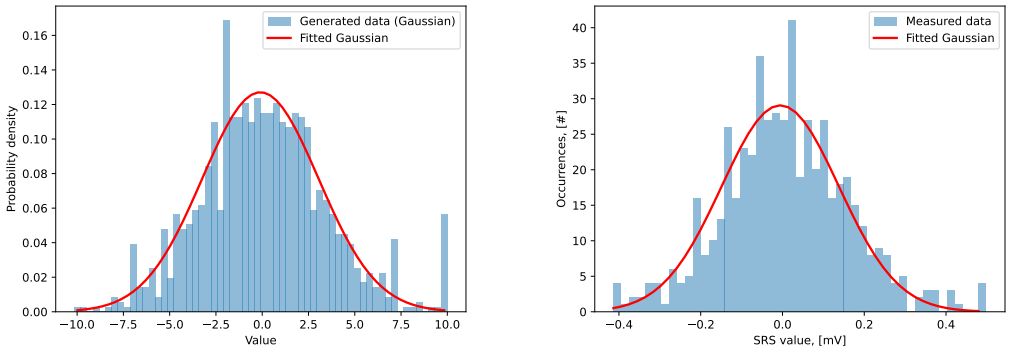

(a) **(b)**

Figure 3.3: a) Generated probability density function plot of Gaussian distribution. The data size was 1000 measurements with RMS value 3 and average value 0 together with artificially generated outliers and 30 bins. Calculating RMS yields 3.44 while performing curve fit yields 3.14. b) Experimentally obtained noise values with 47 bins, RMS is 0.14 mV.

noise. Photodetector's dark noise under absence of light illumination is represented by σ. Laser noise RMS values together with the corresponding coefficients of equation (3.9) are presented in Figure 3.4. The fit coefficient values are presented in Table 3.1. Since shot noise is contributing most to the noise and and laser noise is not dominating, it is concluded that both laser systems are shot noise limited.

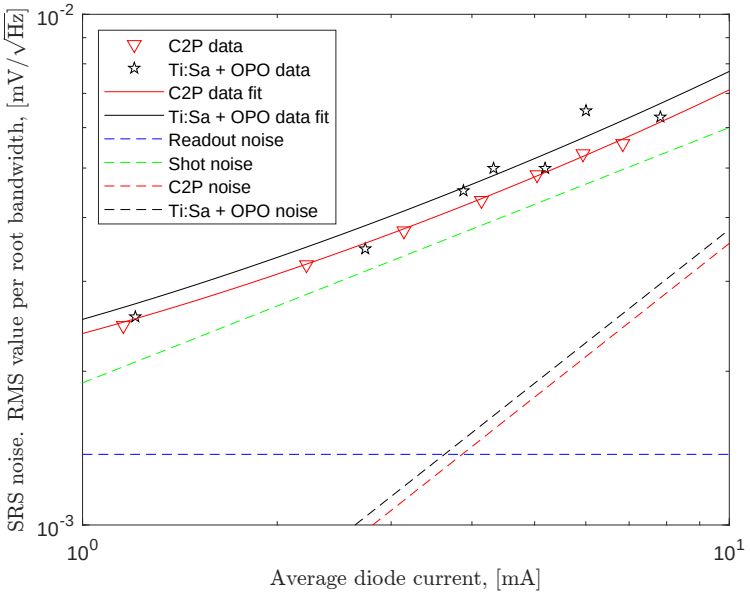

Figure 3.4: RMS comparison between OPOs. Red triangles with line and black stars with line are measurement data with corresponding fit of CRONUS-2P and Ti:Sa systems respectively. Blue, green, red and black dashed line are readout noise, shot noise, CRONUS-2P noise and Ti:Sa system noise respectively.

Table 3.1: Obtained coefficients after curve fitting.

	σ, $\left[\mu V/\sqrt{Hz}\right]$	P_0, [mA]	P_1, [mA]
CRONUS-2P	1.375	0.525	3.863
Inspire	1.375	0.435	3.628

3.2.3 Laser system noise spectral distribution

To check CRONUS-2P and Ti:Sa laser system stability reference, Stokes beam was blocked and only the pump beam was turned on. The objective was changed to 20x, 0.75 NA (Apo lambda series, Nikon). Pixel integration time was set to 0.1 ms for CRONUS-2P and 1 ms for Ti:Sa system. The signal was recorded by selecting a single pixel and registering pump beam. Normalized reference (NR) was calculated by obtaining lock-in signal data, calculating the current and dividing it by the average DC pump current: NR = I_{AC}/I_{DC}, where I_{AC} is the lock-in signal at a 2.5 MHz carrier and I_{DC} is the DC component. The power of the calculated NR was obtained from Fourier transform and is presented in Figure 3.5.

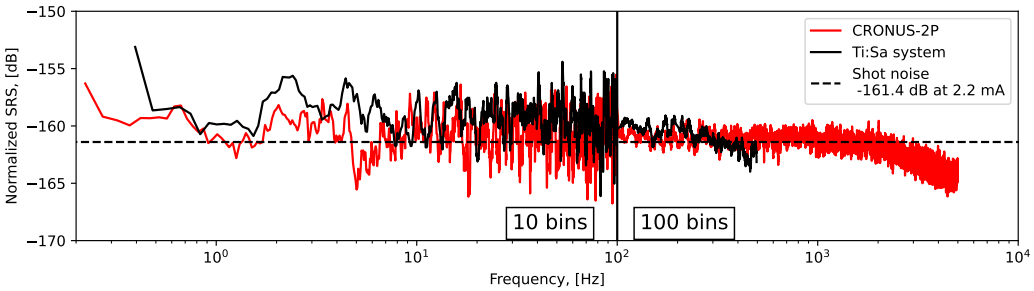

Figure 3.5: SRL signal noise spectrum for 1 Hz bandwidth sampled at 0.1 ms for CRONUS-2P, red line, and 1 ms for Ti:Sa system, black solid line, at 820 nm. Shot noise corresponding to 2.2 mA diode current is presented in black dashed line.

From Figure 3.5 we see that the 820 nm pump detected at 2.2 mA is shot-noise limited at 2.5 MHz modulation for both systems which is required for the highest sensitivity.

3.2.4 CRS with CRONUS-2P

A CRS spectroscopy experiment was conducted using the CRONUS-2P OPO. A sample of a thin polystyrene film was placed over the excitation objective, pump was tuned to 820 nm center wavelength, 10 mW and Stokes pulse was incrementally tuned from 1097 nm to 1069 nm center wavelength while keeping the power at 20 mW. This tuning range was selected to address the vibrational frequency range of the C-H stretching band. At each incremental wavelength position, the delay line was moved to scan the instantaneous frequency difference (IFD) and obtain the corresponding material spectrum. The spectral resolution was calculated to be 30 cm^{-1} with pump and Stokes durations streched from 150 fs and 138 fs to 1.32 ps and 1.37 ps respectively, corresponding to 105 cm^{-1}/ fs linear chirp parameter. The obtained data is presented in Figure 3.6.
It is interesting to note the different shapes of the spectra between CARS and SRS data. This is because the CARS signal contains non-resonant background which

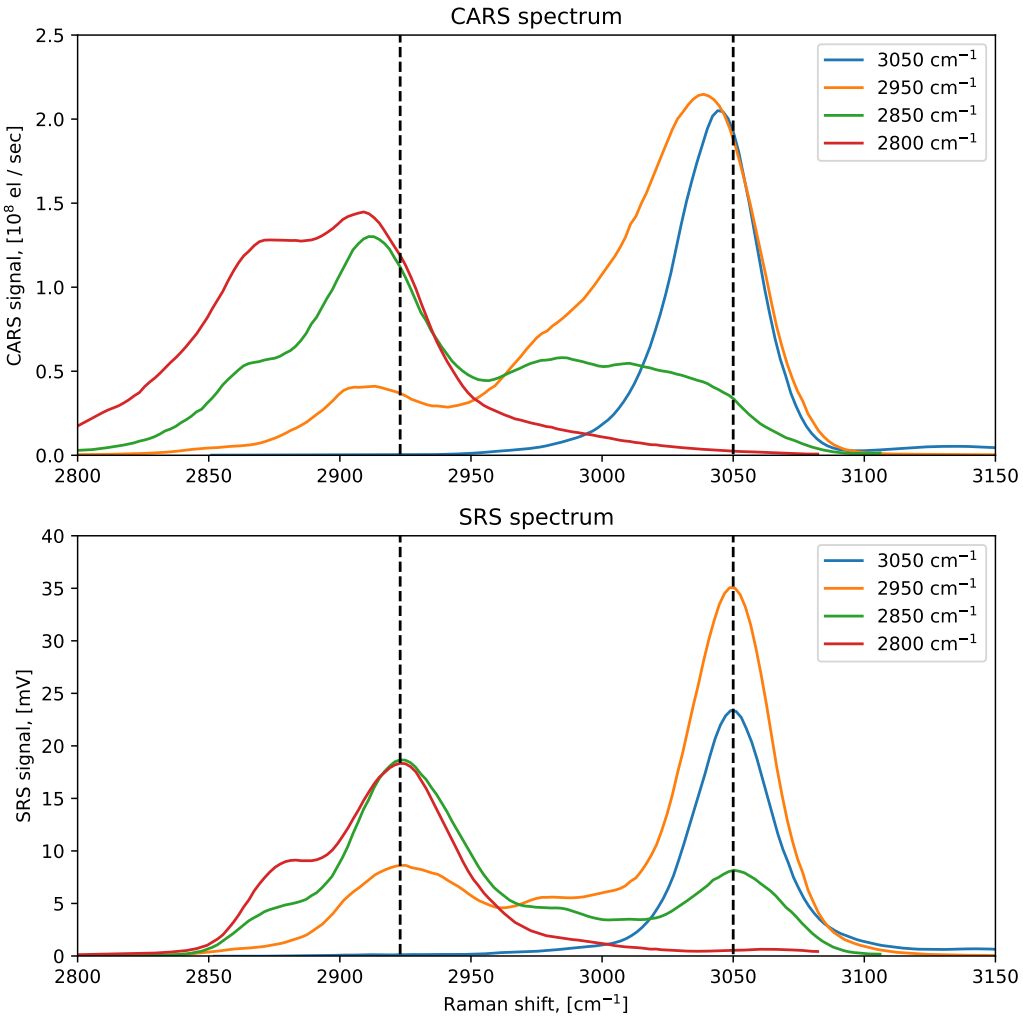

Figure 3.6: CARS and SRS polystyrene spectrum in the C-H stretching region obtained by using CRONUS-2P. Blue, yellow, green and red curves indicate 3050 cm^{-1}, 2950 cm^{-1}, 3850 cm^{-1} and 3800 cm^{-1} wavenumbers respectively. The black dashed lines show polystyrene vibrational bands at 2923 $cm^{-1}$and 3050 cm^{-1}.

interferes with the resonant CARS signal.

To observe CRONUS-2P capability of doing CRS microscopy, mounted Calu-3 cells (ATCC, UK) were grown (37 °C, 5% CO_2)) in a 35 mm culture dish with a glass bottom (Mattek, P35G-1.5-14-C) in EMEM medium (Life Technologies, UK) supplemented with 1 % pyruvate, 1 % glutamine and 10% (v/v) foetal bovine serum (FBS). Upon reaching 60% confluency, cells were fixed with 4 % paraformaldehyde (Affymatrix, UK) for 12 minutes. Phosphate buffered saline (PBS) was used to wash off the fixing agent. Fixed Calu-3 cells in PBS were covered and sealed with a cover glass (thickness 1.5) for imaging experiments. The excitation objective was set to 60×, 1.27 NA (Nikon, Lambda S series) for high spatial resolution. Pump and Stokes were set to 2936 cm^{-1} center IFD by tuning pump to 820 nm and Stokes to 1080 nm. Power just before the excitation objective was 12 mW for pump and 10 mW for Stokes. Images were taken by galvo scanning 26×26 µm area and recording CARS / SRS / pump transmission intensities with 0.1 ms integration time and 76.6 nm pixel

size. After this measurement, sample piezo xyz stage was moved by the scan size to enable tiling measurements over a larger area using 5×5 tiles. In total, an area of $107 \times 107\,\mu m^2$ consisting of 25 tiles is measured. A z-stack of this measurement with z increments of 5 µm and 4 planes was taken. SRS, CARS and pump transmission images of a cell adhered to the coverslip and a rouded up cell, which is ready for division, is presented in Figure 3.7. Such images can be compared to previous work done.

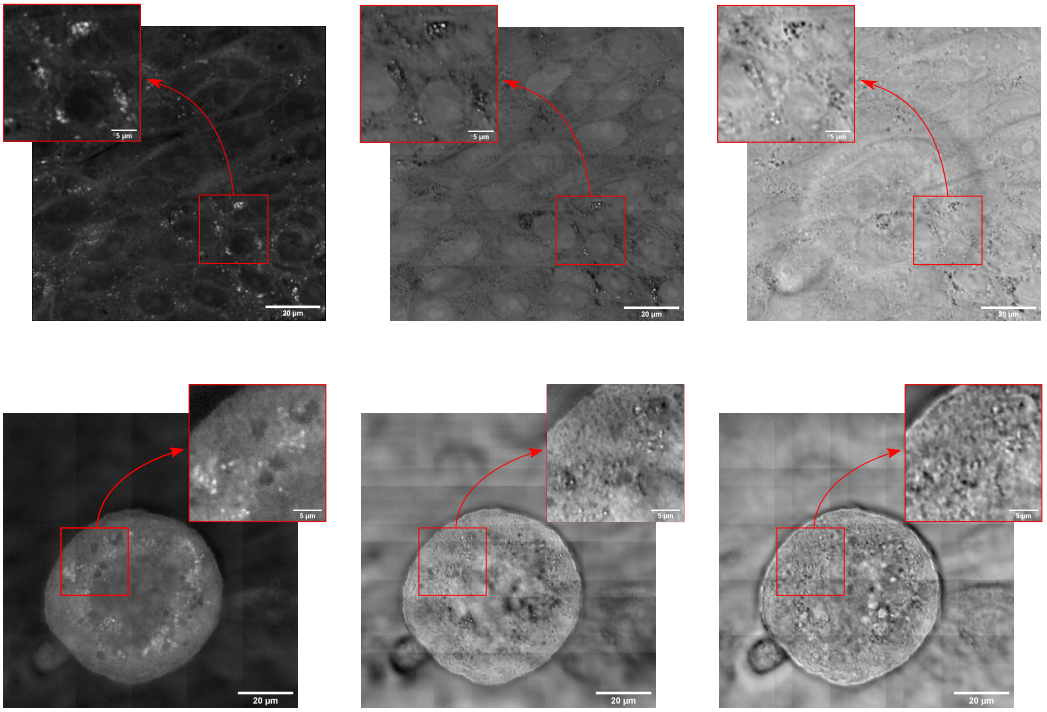

Figure 3.7: SRS, CARS and transmission images of cell surface (first row). SRS, CARS and pump transmission images of a rounded up cell getting ready for division can be seen (second row). First row and second row images are 15 µm apart in the z plane. For SRS, greyscale values range from 0 to 8 mV, CARS greyscale value ranges from 0 to 10^8 el/sec.

3.2.5 Electronically preresonant stimulated Raman scattering (SRS) with CRONUS-2P

SRS is relatively weak but can be enhanced when pump and/or Stokes photon energy approaches an electronic excitation of the material probed, for example a dye molecule, which allows higher sensitivities and increase SNR ratio up to 190 times [73]. The pre-resonant Raman scattering cross section, assuing the pump being close to electronic resonance σ, is then expressed [74]

$$\sigma = K\omega_p\omega_S^2 \left(\frac{\omega_p + \omega_0^2}{(\omega_0^2 - \omega_p^2)^2} \right)^2 , \tag{3.10}$$

where K are frequency-independent terms; ω_p, pump angular frequency; ω_S, Stokes angular frequency; ω_0, frequency of the electronic absorption.

To perform preresonant experiments, a setup was constructed at the University of Konstanz where my main responsibility was to install the laser system together

with the EOM and assist with the initial experiments. All other work was performed by Prof. Andreas Zumbusch and co-workers. The IR beam leaving the OPO (CRONUS-2P by Light Conversion), is frequency doubled by a periodically poled lithium niobate crystal (by HC Photonics) and acts as a pump beam with center wavelength of 640 nm. The visible (tunable from 680 to 960 nm) OPO beam enters electro-optic modulator (by Light Conversion) where pulse picking is happening and changes Stokes beam repetition rate to 19.27 MHz. Both beams were chirped with different amount of glass to match the linear chirp parameter and to improve spectral resolution. Pump and Stokes beams are combined by a dichroic mirror and sent to the excitation objective (63 × 1.2 N.A. by Leica Microsystems). The signal from the sample is collected by a condenser (1.4 N.A. by Leica Microsystems). The Stokes signal is then delivered to a lock-in amplifier where stimulated Raman gain is recorded. The setup is presented inf Figure 3.8.

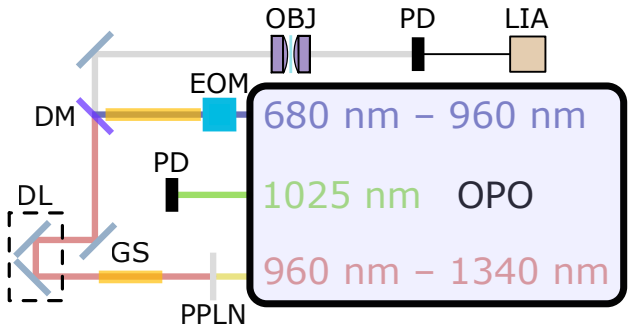

Figure 3.8: Preresonant SRS experiment setup. Here: PPLN, periodically poled lithium niobate; PD, photodetector; GS, glass slabs; DL, delay line; EOM, electro-optical modulator, DM, dichroic mirror; OBJ, objectives; LIA, lock-in amplifier.

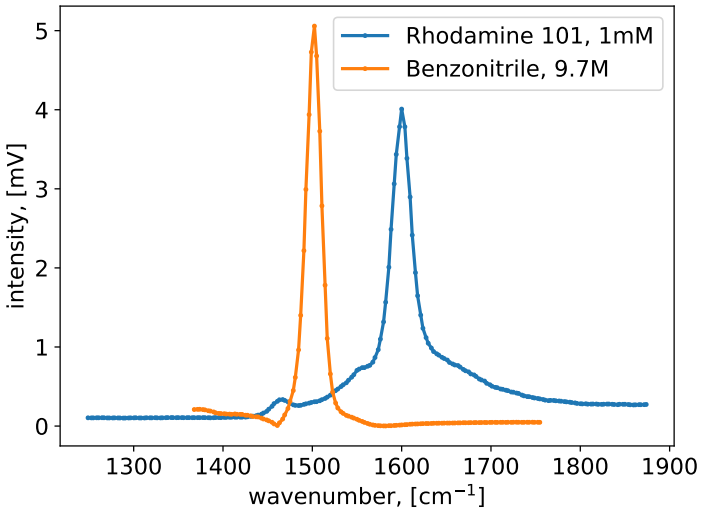

Figure 3.9: SRS signal from pure benzonitrile and 1mM rhodamine 101 dye with absorption wavelengths 271 nm and 565 nm respectively. Despite different concentrations, materials have comparable SRS signal strength due to to preresonance condition.

Some result by using setup in Figure 3.8 are shown in Figure 3.9. Interestingly,

despite having concentration differences in order of 10^4, benzonitrile and rhodamine 101 samples exhibit comparable SRS signal levels due to preresonance. This is because absorbtion of benzonitrile is around 271 nm while rhodamine 101 has absorbtion wavelength of 565 nm which is closer to the pump wavelength of 640 nm. This shows that preresonance SRS is capable of detecting molecules with concentration down to 1µM. To learn more about the samples used and results obtained, please refer to the paper [75].

3.3 Conclusion

Both systems are shot noise limited which is crucial for sensitive SRS imaging. The advantage of Inspire is broader spectrum which should allow after applying spectral focusing scheme. The two independently tunable CRONUS-2P channels allows more flexibility when designing an experiment. Dual channel CARS could be applied by using 800 nm as a pump and 1025 nm, 1100 nm pulses as Stokes which would allow to image C-H stretching band simultaneously with the cell silent region and this feature is demonstrated later in this thesis. Additionally, by having two independently tunable channels and frequency doubling longest wavelength channel, allows to access preresonant SRS regime which enhances the signal in orders of magnitude. Theoretically, same signal enhancement with electronic preresonance can be demonstrated with CARS.

Chapter 4

Point scanning SHG/THG and dual coherent anti-Stokes Raman scattering (CARS)

4.1 SHG/THG

4.1.1 Setups

Experimental layouts are presented in Figure 4.1. The initial setup (setup a) for SHG and THG imaging used an oscillator with 1030 nm centre wavelength, 76 MHz pulse repetition rate, 1 W average power and about 110 fs pulse duration (FLINT by Light Conversion). A half-wave plate and a polarizer (custom by Altechna and GT10-B by Thorlabs) allows to controllably reduce the power, and a long-pass filter (FELH0700 by Thorlabs) ensures no light at wavelength below 700 nm, which could be detected by SHG and THG detectors enters the excitation port. After this the beam passes through a galvo-mirror pair (6215H by Cambridge Technology) and a 4f system consisting of achromatic doublet pairs (AC300-100-B and AC508-200-B-ML by Thorlabs) with 4 × expansion to fill the back aperture of an excitation objective. The beams are raster scanned over the sample by a focusing objective (20×0.75 N.A. Plan Apo lambda by Nikon), the light passes collimating lenses and fused silica lenses (LA4725 and LA4874 by Thorlabs) and SHG together with THG are separated by a dichroic mirror (DMLP550R by Thorlabs). SHG and THG seperately pass through the filters (FBH520-40 for SHG and FGUV11 325-100 for THG by Thorlabs) to separate the generated light from the residual fundamental laser beams. The light is registered by two photomultiplier tubes (H10682-210 by Hamamatsu) with photon counting electronics providing TTL pulses which are counted by a 16-bit digital acquisition unit (PCI-6122, National Instruments). The electronics are controlled by using LabView software. Images were obtained by using custom LabView code and processed using Python where the acquired raw data is converted into 8-bit image. The initial setup was built by Dr. Lukas Kontenis at Light Conversion.

Later, the setup was modified (setup b, Figure 4.1) changing the laser source to the CRONUS-2P. The first channel (VIS) of the OPO emits at wavelengths tuneable between 680 nm and 960 nm, the second channel (fixed) at 1025 nm and the third channel (NIR) between 960 nm and 1300 nm. The repetition rate of all channels is equal at 76 MHz with around 1 W average power for the used wavelengths and pulse duration are about 150 fs. An additional half-wave plate (custom by Altechna) was

added to change the linear polarization direction. To filter out SHG from shorter wavelength VIS channel, the band pass filter was exchanged to the (FGB7M 468-65 by Thorlabs).

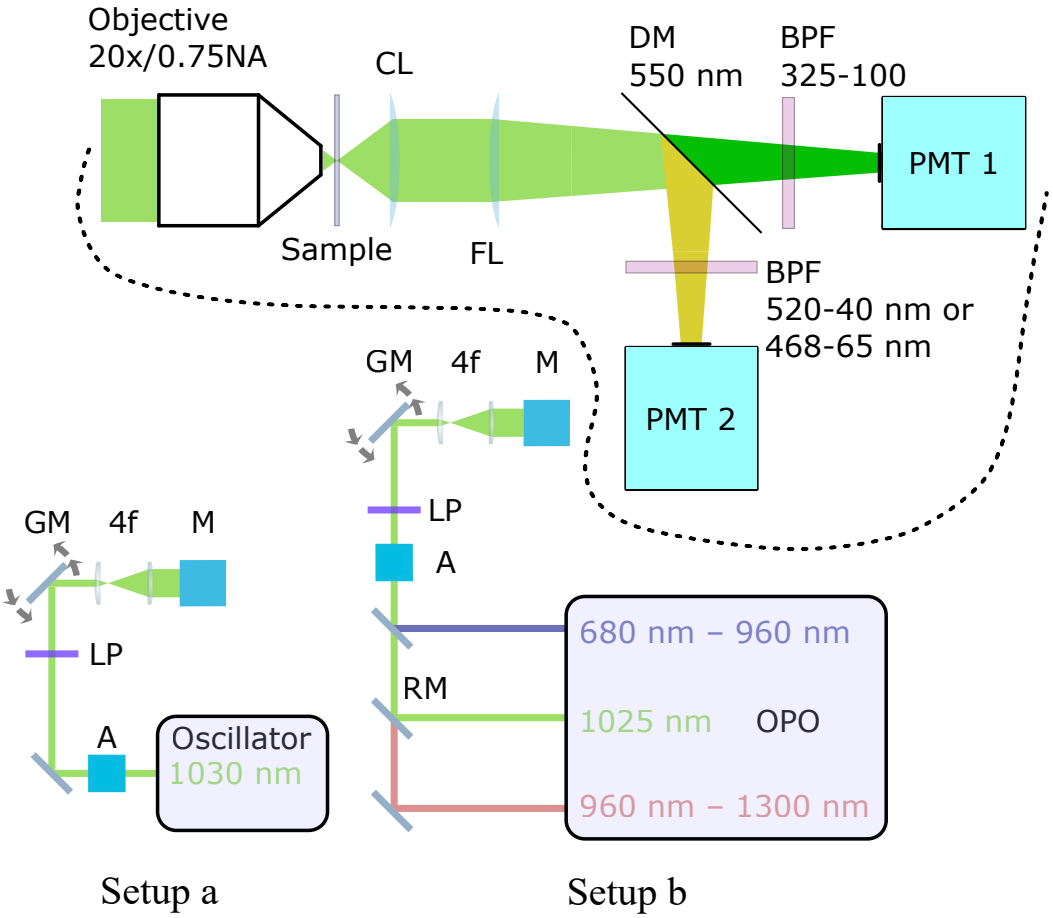

Figure 4.1: Experimental setups used for SHG and THG imaging with oscillator (Setup a) and OPO (Setup b). Here: A, power attenuator; RM, removable mirror; LP, long-pass filter; HWP, half-wave plate; GM, galvo mirrors; 4f, 4f system; M, microscope rack; CL, collimating lens; FL, focusing lens; BPF, band-pass filter, PMT, photomultiplier tube. A more detailed layout of M is presented in the upper part of the figure. Note, the band pass 468-65 nm filter was exclusively used for the VIS channel instead of 520-40 nm filter.

4.1.2 Results

A Biomax SK241a skin cancer tissue array was imaged with setup a, and the generated simultaneous SHG, THG and combined images are shown in the first row of Figure 4.2. Frame time was 10 s, pixel time 2.5 µs, laser power 15 mW. SHG and THG images are displayed 0 to 30 and 0 to 70 counts respectively, black to white greyscale. SHG signal is generated from collagen fibers in the sample while THG is generated from lipid droplets.

It is interesting to note that some of the structures which are visible in THG are not visible in SHG. This is because collagen bundles lack centrosymmetric properties and THG is not generated in bulk [41]. Structures with varying refractive index, such as lipid layers and cell walls generate THG signal. Different parts of the sample

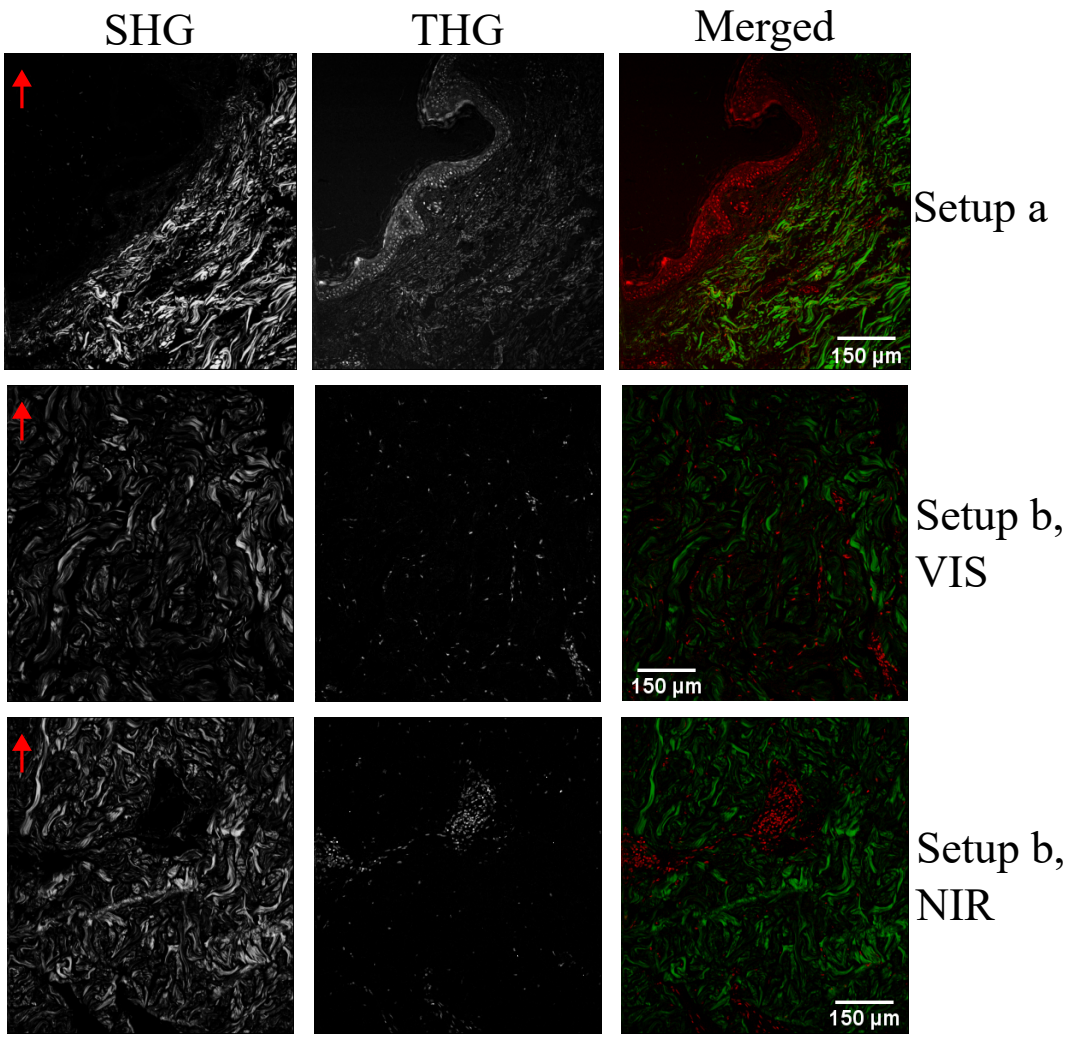

Figure 4.2: SHG and THG images of skin cancer tissue taken with setups a and b at different regions. Rows show SHG, THG and combined images respectively while columns show results of different setups. Red arrow indicates polarization direction. Wavelengths of setup b VIS and NIR were set 970 nm and 1050 nm respectively. For both setups frame time was 20 s, pixel time 5 µs, laser power for SHG and THG was 7 mW and 10 mW respectively. SHG and THG images are displayed 0 to 70 and 0 to 5 counts respectively, black to white greyscale.

can generate SHG and THG signals separately which shows that in combination, SHG and THG microscopy is a powerful tool for structural imaging.

To asses the setup performance, the SHG and THG results obtained from setup a and setup b were compared between each other. Each OPO channel was tested separately. Here, only the results from VIS and NIR channels are presented since the fixed channel is similar to the source used in setup a with only 5 nm center wavelength difference (1025 nm instead of 1030 nm). Also, 970 nm from the VIS and 1050 nm from the NIR were selected in order to keep similar mirror reflectance and to avoid filter changes. The beam diameter for the VIS channel is around 4 mm, fixed channel has a beam diameter of 5 mm and the NIR channel has a beam diameter of 7 mm (at $1/e^2$). Obtained results from the VIS channel are presented in Figure 4.2. Frame time was 20 s, pixel time 5µs, laser power for SHG and THG was 7 mW and

10 mW respectively. SHG and THG images are displayed 0 to 70 and 0 to 5 counts respectively, black to white greyscale.

THG in the second row of Figure 4.2 shows only small components with different refractive index where THG is generated. Most likely this is a lipid rich region. Results obtained using the NIR channel with 1050 nm are presented in the third row of Figure 4.2 where SHG and THG are generated by different parts of the sample which indicate different material properties separating collagen from lipid droplets.

To observe the dependence of the SHG on the linear polarization direction of the excitation beam, a half-wave plate was added to the setup just before the galvo scanners as depicted in Figure 4.1 (setup b). A different skin sample was used exhibiting a rich collagen fibre structure. It was imaged with different linear polarization angles from 0° to 180° in 30° degree steps. Average intensity values were recorded for each image in a selected area. The intensity values were normalized and together with the selected area are presented in Figure 4.3.

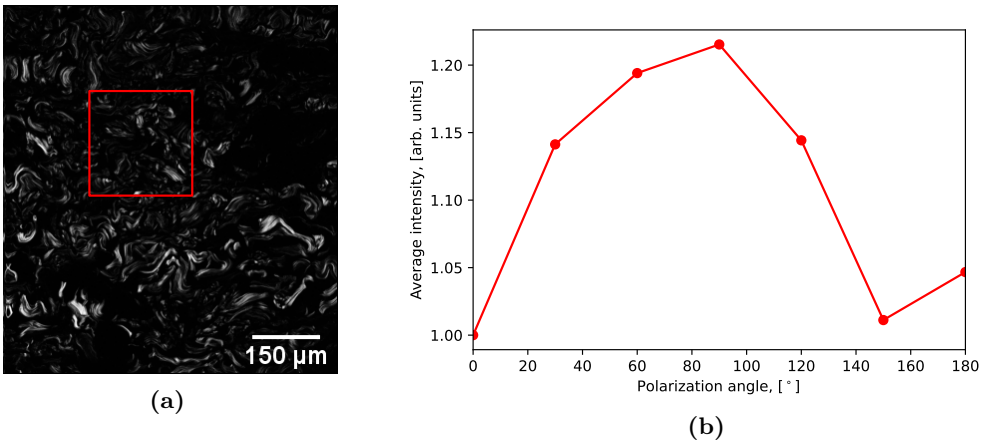

(a) (b)

Figure 4.3: SHG image of human skin sample with maximum pixel value corresponding to 50 counts at 0° (a). Frame time, 20 s; pixel time, 5 µs; average power at the sample, 7 mW. Normalized intensity values from the red rectangle area are shown in (b).

To highlight intensity changes with polarization direction, images were merged together to observe the differences. Image with 0° polarization was placed in the green channel and was separately merged with 90° image and 180° image placed in red and blue channels. In case of perfect intensity match, the resulting merged image would result in a greyscale image while intensity mismatch leads to visible colors. Obtained results are presented in Figure 4.4.

From Figure 4.4 it can be seen that having 180° polarization difference leads to small mismatch between images since the overlap is not perfect. One of the possible reasons is the slow drift. Another reason might be beam displacement from the original path when half-wave plate was moved to change the polarization. Duration between images was in the 10s of second range and the polarizer was moved manually which increases the probability for small accidental displacement in the sensitive system. Results obtained from 90° mismatch lead to conclusion that the sample is sensitive to polarization angle and the thermal sample drift is a problem when time delay is present between two separate imaging sessions. Since simultaneous SHG and THG imaging was successfully demonstrated with the OPO, it was decided to

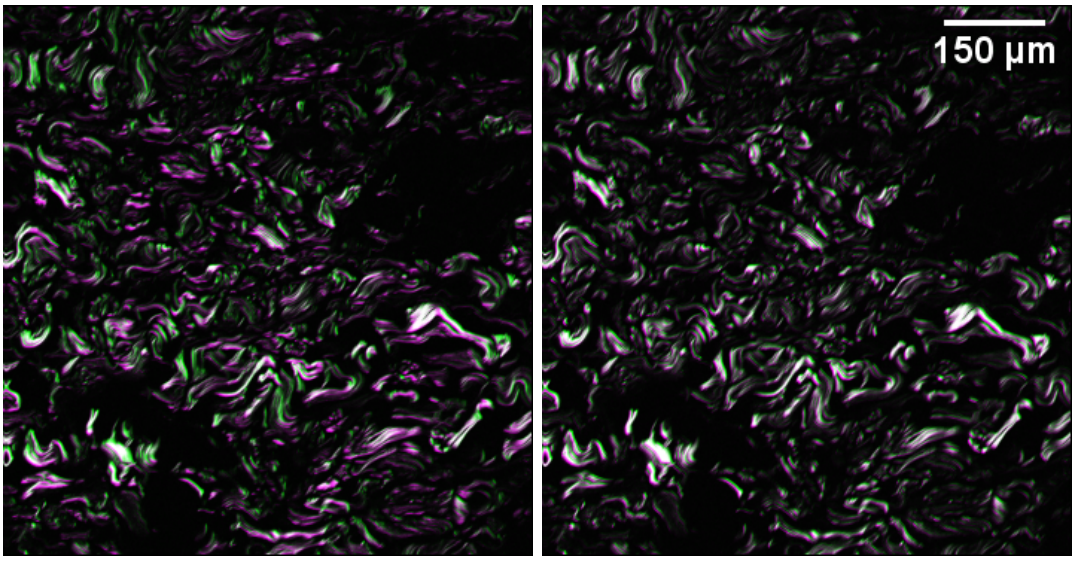

(a) (b)

Figure 4.4: Merged SHG images with different polarization. Two images merged with 0° in the green channel and 90° polarization in the red and blue channel. (b) shows 0° in the green channel and 180° polarization in the red and blue channel.

extend the imaging modalities of the microscopes from a single beam to multi-beam.

4.2 Dual CARS

4.2.1 Introduction

As mentioned in the previous chapter, having two strong electromagnetic fields with different frequencies allows to generate fields of combination frequencies as can be seen by expanding equation (2.35) to the third-order yielding the frequencies: ω_1, ω_2, $3\omega_1$, $3\omega_2$, $2\omega_1 - \omega_2$, $2\omega_1 + \omega_2$, $\omega_1 - 2\omega_2$, $\omega_1 + 2\omega_2$. In this chapter, CARS having the frequency $2\omega_1 - \omega_2$ is going to be investigated.

Two independently tunable channels with one fixed wavelength not only allows SHG/THG imaging, but also CARS imaging in three different vibrational frequency regions: fingerprint (fixed and NIR), cell silent (VIS and fixed) and C-H stretch (VIS and NIR). This is desirable as it allows to image two regions without time delay which sometimes causes motion artifacts. Therefore, a setup was constructed which allows to image the cell silent and C-H stretch regions while the fingerprint region was omitted due to complications of detecting wavelengths longer than 800 nm.

CARS setups measuring two, or more, vibrational frequencies simultaneously were reported previously [76, 77, 78]. A simple way to isolate the resonant response in CARS is to measure at two vibrational frequencies simultaneously, probing the dispersive response, either by wavelength modulation [79] or using spectral focusing [71, 80]. The spectral focusing approach is also able to address significantly shifted frequencies, but not spanning from silent to C-H stretch region due to laser bandwidth [71]. A broadband single wavelength pulse was used for differential CARS together with other non-linear microscopy modalities [80]. Two individual OPOs have been used [81, 82] to provide two independently addressable vibrational frequencies simultaneously without any motion artifacts. Recently, dual band CARS

using Fourier-transform excitation employing a Ti:Sa oscillator and a synchronised Yb fibre laser was shown to cover both fingerprint and C-H stretch region [83].

4.2.2 Setup

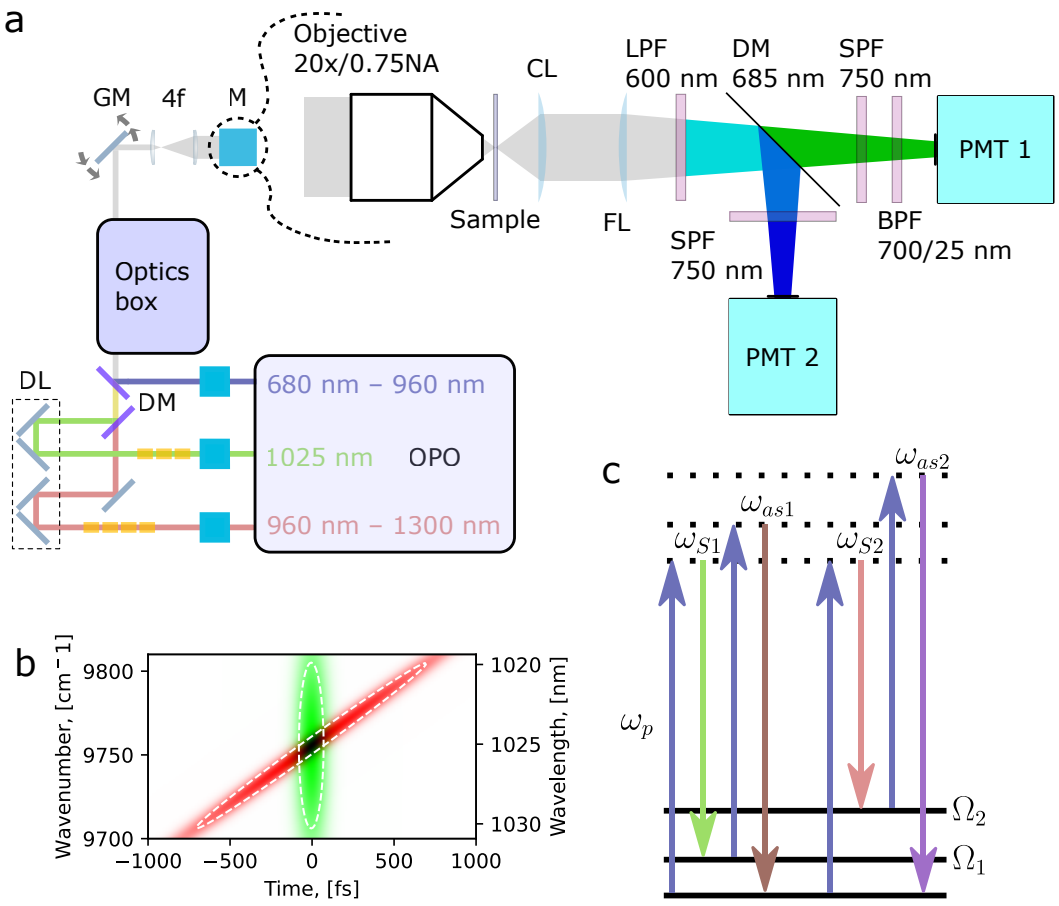

Figure 4.5: a) Experimental setup with the components: A, power attenuator; DL, delay line; DM, dichroic mirror; DB, dispersion blocks; GM, galvo mirrors; 4f, relay from GM to objective back focal plane; M, microscopy rack; CL, condenser lens; FL, focusing lens; LPF, longpass filter; SPF, shortpass filter. b) Calculated Wigner-Ville distributions of Fourier-limited 150 fs pulse at 1025 nm center wavelength in green stretched to 1.4 ps in red. Dashed white line shows intensity FWHM contours. c) Dual CARS energy level diagram.

To perform dual CARS microscopy some changes are required for the setup b in Figure 4.1. Removable mirrors were replaced with two dichroic mirrors (custom by Eksma and 87-041 by Edmund Optics) to spatially combine three different wavelength beams. The delay line (VT-80 by Physik Instrumente) was added for the fixed and NIR channels to match temporal delay between all three beams. Dispersion blocks (SF57, N-SF66 by II-VI incorporated and ZnS by Castech) were added to extend the pulses to picosecond range for spectral focusing. Because GVD depends on wavelength as depicted in Figure 2.23, different amounts of glass were added to each beam path inside the optics box. Additionally, the optics box (layout is presented in appendix Figure A.1) approximately matches the delay between each beam path so that it can be fully compensated with the delay lines. Fixed and NIR

beams traversed 100 mm and 160 mm N-SF66 glass respectively before recombining with VIS beam and traversing additional 145 mm of SF57, 140 mm of N-SF66 and 30 mm of ZnS, resulting in a calculated GDD of 81089 fs^2 for the 831 nm VIS 76312 fs^2 for the 1025 nm fixed and 78189 fs^2 for the 1093 nm NIR. The coefficients for the Sellmeier equation (2.51) were taken from the manuals [84, 85]. For the ZnS crystals, we use the expression [86]

$$n^2(\lambda) = \epsilon_0 + \frac{A}{\lambda^2 - \lambda_U^2} + \frac{\epsilon_0 - \epsilon_\infty}{\lambda^2/\lambda_I^2 - 1}, \tag{4.1}$$

with $\epsilon_0 = 8.393$, $\epsilon_\infty = 5.105$ $\lambda_U = 0.2421\,\mu m$, $\lambda_I = 36.71\,\mu m$, and $A = 0.14383\,\mu m^2$.

The OPO has a built-in GDD control for the VIS and NIR channels which allows to fine adjust the GDD most optimal spectral resolution which is calculated to be 12.2 cm^{-1} [60]. Using initial spectrally-limited pulse duration and the applied linear chirp, the Wigner-Ville distribution was calculated by using equation (2.50) and is presented in Figure 4.5b for reference. The PMT used for the THG detection (PMT 1) was replaced by an extended red multialkali photocathode (H10721-20 by Hamamatsu) in order to detect wavelengths longer than 700 nm. The CARS signal from the sample was separated from SHG and THG signals by a long pass filter (FEL0600 by Thorlabs). The two CARS signals were separated by a dichroic mirror (T685lpxr, Chroma Technology) and were filtered by 750 nm shortpass filters (FES0750, Thorlabs). The silent region CARS signal (around 699 nm) is filtered by a 25 nm wide bandpass filter centred at 700 nm (86-658, Edmund Optics) and detected by PMT 1. Since H10721 does not have a photon counting circuitry, the PMT current is amplified by a current-to-voltage converter (C9999 by Hamamatsu) with 10 MHz bandwidth and 50 kΩ transimpedance. The signal bandwidth was limited by a 100 kHz low pass filter (EF502 by Thorlabs) before being digitised by the digital acquisition unit. The C-H stretch signal (around 670 nm) is detected by the PMT 2. The CARS signal created by the two Stokes pulses, probing IFDs in the finger print region, is not detected in the present setup because of the difficulty to register CARS signal which is around 800 nm. The setup layout is presented in Figure 4.5a with dual CARS energy diagram presented in Figure 4.5d.

4.2.3 Axial focus overlap

While the transversal overlap can simply adjusted by the beam direction using the mirrors, the axial overlap requires adjusting the beam divergence. For the maximum CARS generation, all three beams must focus at the same sample plane which is affected by input beam collimation and longitudinal chromatic errors of the 4f lenses and the objective. To determine the focus position of each beam THG generation at the glass-air interface, a coverslip was used. This experiment can show the exact beam focus position since the third harmonic is only generated at the surface of the glass as discussed in Section 4. Results showing initial VIS and NIR beam focal positions are presented in Figure 4.6a revealing a 6 µm offset. Also, noise is present when THG was 267 nm because of the used filter (Thorlabs FGUV11) which has around 5 % transmission at fundamental 800 nm wavelength. To surmount the axial focus mismatch problem, a relay lens system, which transfers real image on an optical path, was added to change beam collimation closer to the objective. This allows to change beam collimation closer to the objective and achieve axial overlap but keep the beam size constant. The lens system is presented in Figure 4.7a where red rectangle shows a telescope which uses to change beam collimation by moving

one of the lenses while green rectangle shows relay lens which relays beam divergence closer to the excitation objective.

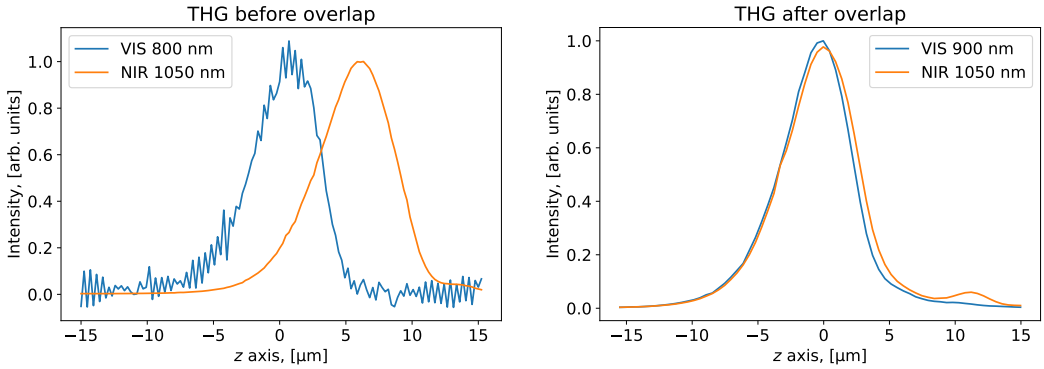

(a) **(b)**

Figure 4.6: THG axial profiles before (a) and after (b) installing relay lenses. The results obtained in (a) by using the 800 nm fundamental are noisy due to difficulty of recording the signal at 267 nm. Average pulse power was set to 10 mW for each beam.

Since moving one of the telescope lens is required, a custom lens holder was designed which has an additional in plane movement ability provided by a dovetail translational stage (DT12/M by Thorlabs). By moving the lens on the translational stage, beam collimation is alterated which is relayed closer to the objective and in turn changes focal position. For initial testing, the holder was 3D printed by using polylactic acid to test stability and performance. The computer aided design model with 3D printed part is presented in Figure 4.7b. The improved beam overlap is presented in Figure 4.6b where 900 nm wavelength was used to avoid low signal level. Note, that fixed channel was not adjusted as it was axially overlapping with the NIR channel.

The 3D printed lens holder raised stability issues as the plastic was easily deformable when touched and was susceptible to temperature changes which led to signal fluctuations and required constant beam realignment. Additionally, glass blocks and other optical components started to cramp-up the limited space on the optical table. Therefore, it was decided to place all optical components into a single optics box to make the setup more stable and less space-consuming. Image showing optical setup before and after optics box is presented in Figure 4.8.

4.2.4 Sample preparation

4.2.4.1 Beads

Due to high bond concentration, PS and PMMA beads are great for CARS imaging. The sample was prepared by pipetting 10 µL of 1% solid suspension of 20 µm diameter PMMA beads (MMA20K, Phosphorex, USA) and 10 µL of 1% solid suspension of 10 µm diameter PS beads (118, Phosphorex), onto a glass coverslip (#1.5, 24 × 50 mm, Thermo Scientific), and mixing them before covering with a further glass coverslip and sealing the edges with an adhesive coating (OP-4-20641, Dymax, USA).

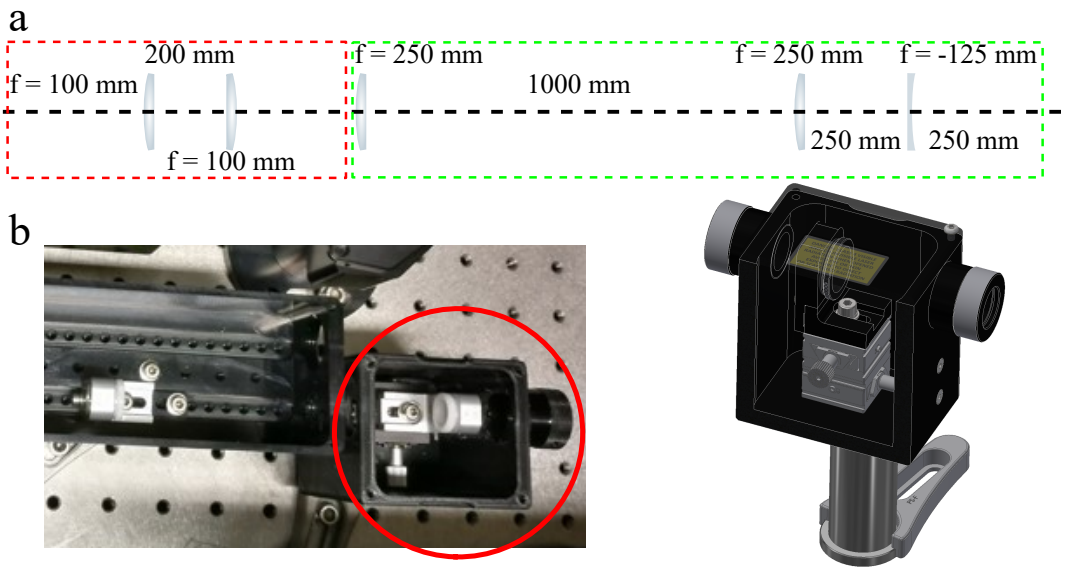

Figure 4.7: a) Schematics of the relay system used to transfer the laser diameter to the galvo mirror location and b) 3D printed lens mount on optical table and computer aided design model.

4.2.4.2 Oil - water - heavy water reverse emulsion

A sample containing heavy water (99% purity, Sigma Aldrich), water and olive oil (mechanically extracted extra virgin olive oil with mostly oleic acid) was prepared. Dishwashing liquid (Hand Dishwash, Neutral) was added to olive oil at 0.1% v:v as surfactant. To prepare a reverse emulsion, 1% v:v of water and heavy water were added, and the sample was vigorously shaken by hand in a test tube for 1 min. 10 µL was pipetted onto a glass coverslip (#1.5, 24 × 25 mm by Thermo Scientific) before covering the sample with another glass coverslip. The surfactant is stabilising the small water droplets, hindering their coalescence.

4.2.4.3 Deuterated HeLa cells

Deuterated lipids in fixed Human cervical carcinoma (HeLa) cells were prepared by using the protocol [87]. The cells (by ATCC) were cultured in minimum essential medium (MEM) supplemented with GlutaMAXTM (Life Technologies), 10% (v/v) foetal bovine serum (FBS) (Life Technologies), 1x Non-Essential Amino Acids (Life Technologies) and 1 mM sodium Pyruvate (Life technologies) directly onto glass coverslips (thickness #1.5, 25 mm diameter, VWR International, USA). Following overnight attachment, cells were transferred to MEM containing supplements and a complex of bovine serum albumin (BSA) (Sigma Aldrich) and the investigated fatty acid at a concentration of 47 µg/ml. Fatty acid-BSA complexes were formed by adapting a published protocol, which involved combining 5% BSA/PBS solutions with 20 mM sodium-fatty acid solutions to form fatty acid-BSA complexes with a final concentration of 1.656 mg/ml. Following an 18-hour incubation period in fatty acid-BSA-supplemented media, coverslips were fixed in a 4% formaldehyde-PBS solution (Affymetrix) for 20 minutes and mounted onto standard glass microscope slides using a 13 mm hole diameter, 120 µm thick adhesive imaging gasket (Grace BioLabs) filled with water containing Anti-Anti (Life Technologies).

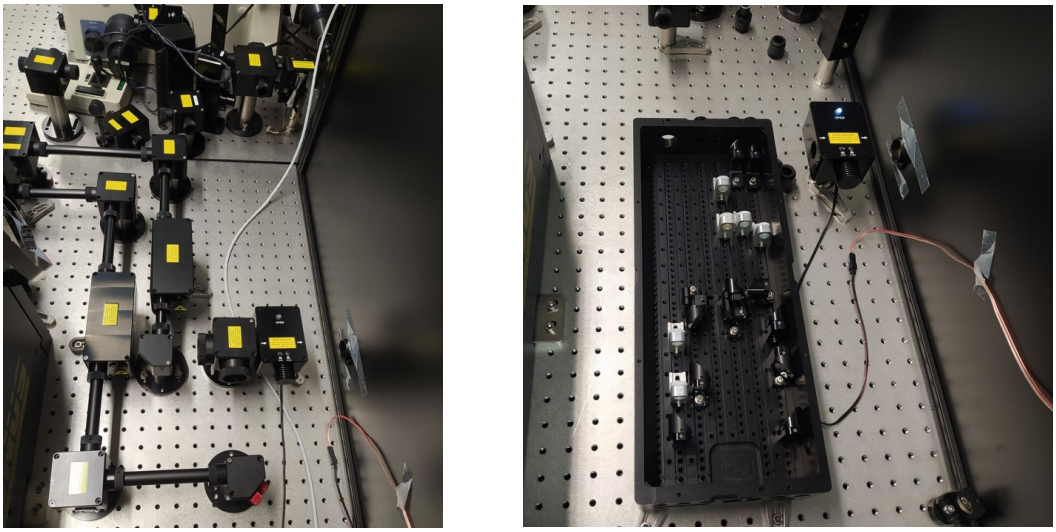

(a) (b)

Figure 4.8: a) Setup before breadboard, with all components in separate casings b) setup after the optics box was placed, still under construction.

4.2.5 Setup characterization

To understand the system better and to make sure that the laser works as expected it was important to measure pulse duration as close to the OPO as possible, before pulse acquires additional GDD which allows to measure shortest possible duration. Also, it was important to characterize the internal group delay compressor and to make sure that it was calibrated and works as expected. Also, for measurement convenience, it is useful to know the delay between all three channels and how it changes when wavelength and GDD values are changed.

4.2.5.1 Pulse duration measurement

First, the transform-limited pulse duration from all three channels was measured by changing the GDD values and setting it to 0. The measurement was performed by placing a non-collinear scanning auto-correlator (GECO by Light Conversion) right after the power attenuator. Since it generates SHG and provides non-colinear intensity traces and since pulse energy is in the nJ range, 1 mm thickness Beta Barium Borate (P49945-2 BBO by Castech) crystal was used. By moving the delay line, intensity traces are recorded and by fitting Gaussian function allows to calculate intensity FWHM value. An example for a 831 nm pulse is provided in Figure 4.9a. In cases when zero GDD not accessible using the internal pulse compressor, dens flint glass (N-SF66 by II-VI incorporated) was added to the system to compensate for the negative GDD values (tunable from -3000 fs^2 to -20000 fs^2 at 800 nm). The same procedure was repeated for other wavelengths both from VIS and NIR channels and wavelength versus duration is plotted which is presented in Figure 4.9b. Fixed channel pulse FWHM assuming Gaussian shape was recorded to be 179 fs.

Figure 4.9b shows sharp changes in pulse duration at around 800 nm and 1150 nm. Both of the changes are due to OPO configuration and internal optical component switch when this wavelength threshold is reached. Figure 4.9c shows that spectral

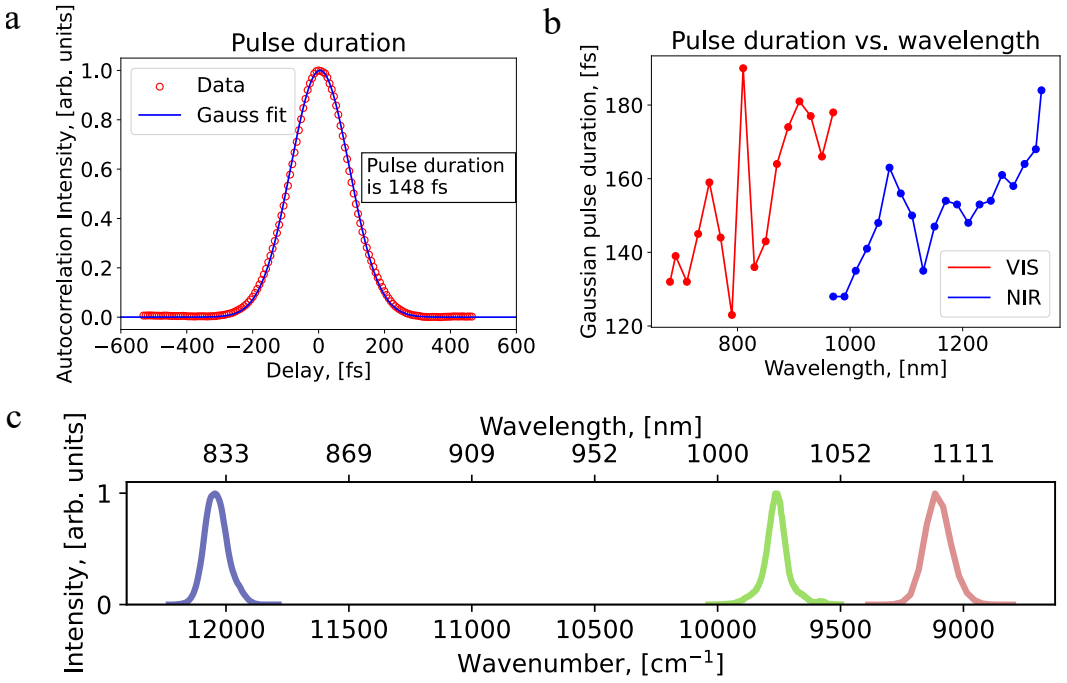

Figure 4.9: a) Intensity auto-corellation trace of a femtosecond pulse with Gaussian fit and 148 fs intensity FWHM duration recorded at 831 nm center wavelength. b) Spectrally-limited pulse intensity durations of various wavelengths in FWHM. c) Spectral plots of VIS, fixed and NIR channels tuned to 831 nm, 1025 nm and 1100 nm center wavelengths with corresponding FWHM of 7 nm, 8 nm and 12 nm respectively.

FWHM values for 831 nm, 1025 nm and 1100 nm are 7 nm, 8 nm and 12 nm respectively which corresponds to spectrally limited Gaussian pulse duration of 145 fs, 193 fs, 148 fs respectively which is consistent with the pulse duration measurements.

4.2.5.2 Spectra measurement

Another important measurement is the beam spectra measurement. It is important to know that the correct wavelength is selected when performing the experiments and the shortest pulse duration can be estimated which should confirm pulse duration measurements performed before. The experiment was performed by placing a beamsplitter (custom by Eksma optics) which reflects 80 % of the light just after the power attenuators which were attenuating the remaining power. The remaining light was directed into a spectrometers (AvaSpec-NIR256-1.7 by Avantes for the NIR channel and Qmini AFBR-S20M2XX by Broadcom for the VIS and fixed channels). VIS and NIR channels were tuned to 831 nm and 1100 nm respectively. The recorded spectra plots are presented in Figure 4.9c

4.2.5.3 Internal group delay dispersion measurement

It is important to understand the group delay dispersion system and to make sure that the device is calibrated accordingly. Therefore, pulse duration was measured at the very end of the optical path, near the galvo-mirrors. The measurement procedure was identical as described in previous subsection except that the 1 mm BBO crystal was changed to 2 mm BBO crystal (P49665-2 BBO by Castech). Thicker crystal

was used as nJ pulses are stretched to ps range and since SHG efficiency is inversely proportional to pulse duration squared, conversion efficiently drops significantly. Wavelengths were set to 800 nm and 1050 nm and intensity FWHM duration was measured while changing GDD values. Since the type of glass and its total length is known, it is possible to calculate total GDD added to the system by using equation (2.56). As pulses around 150 fs are relatively long, optical components as mirrors and lenses do not add significant amount of dispersion so they were excluded from the calculation. Knowing spectrally limited pulse duration and total GDD added, one can calculate theoretical final pulse duration by using equation (2.57) which is show in Figure 4.10 as a black dashed line. Red and blue curves are VIS and NIR channels respectively.

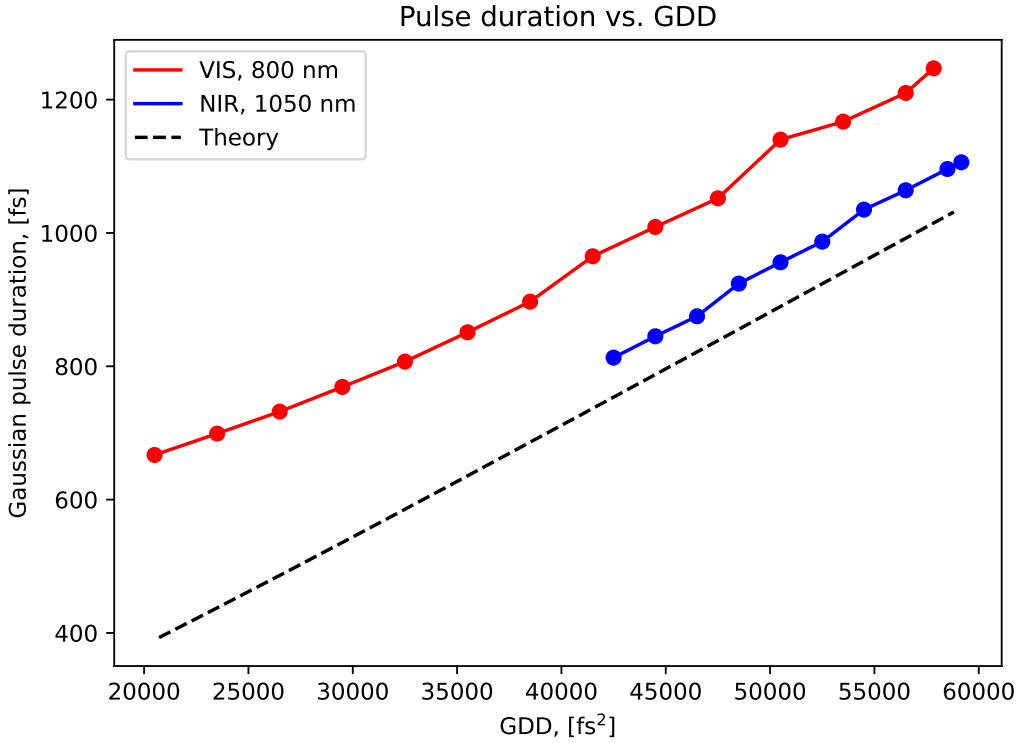

Figure 4.10: Intensity FWHM duration as a function of GDD at the end of optical path, near galvo-mirrors. GDD was changed by adding fixed amount of glass in the optical path and then changing GDD inside CRONUS-2P. Results indicate that additional GDD is added to pulses before they leave the OPO. The amount of GDD added is higher for the VIS channel.

Offsets in the graphs indicate that the pulses leaving OPO are not transform limited but are leaving with additional GDD values even when there should be no GDD indicated by the software. Also, because VIS, NIR and theoretical curve slopes are very similar it can be concluded that initial pulse duration is close to 150 fs. The issues described here were taken into account when performing the experiments with the OPO by accounting for the GDD offset.

4.2.5.4 Delay between channels

It is important to know the delay line position where the temporal overlap is generated between various wavelengths. To investigate it, a 2 mm BBO crystal was placed close to galvo mirrors for efficient non-linear generation. VIS and fixed channels were turned on and SFG was generated by moving the delay line of the fixed channel. As SFG is in the visible region, no detector is required and SFG was observed from the scattering on a paper. SFG was generated with various VIS wavelengths while fixed channel delay line position was recorded. An identical procedure was repeated with the NIR and fixed channels as the SFG is also in the visible. To investigate GDD influence on the delay, VIS channel was tuned to 900 nm and GDD was changed incrementally. After each GDD change, pulse overlap was corrected by moving the delay line of the fixed channel and generating SFG. Identical procedure was repeated at 1100 nm for the NIR channel. Results showing relative delay between channels are presented in Figure 4.11. Note, positive delay values indicate that the fixed pulse is leading the other pulse and zero delay is when pulses are generating SFG. For example: 670 nm from VIS is lagging in time from fixed by 7 ps when compared with 710 nm VIS. 790 nm VIS is leading in time the fixed beam by 9.5 ps when compared to 710 nm VIS. The gap between 950 nm and 1040 nm in Figure 4.11a is due to dichroic mirror present in the setup which did not allow to combine selected beams with the fixed channel.

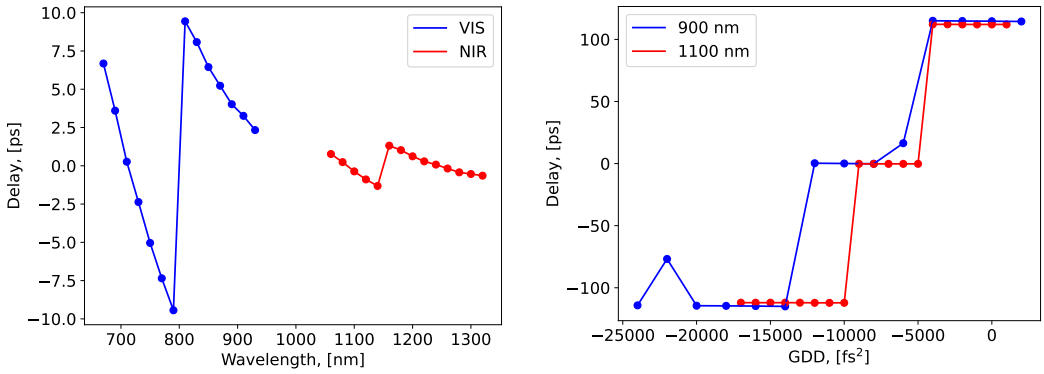

(a) **(b)**

Figure 4.11: a) Fixed channel relative delay dependency on OPO wavelength when GDD is zero. b) Fixed channel relative delay dependency on GDD. Since the delay line step size in known, it is possible to calculate the delay in ps.

The sharp changes in Figure 4.11a at arround 800 nm and 1150 nm is again attributed to the optical element changes in the OPO. The main reason for the element changes in the OPO is to keep high power output of various wavelengths which requires high transmission/reflection optics and they work in a narrow wavelength range. The sharp delay jumps when internal GDD values are changed are caused by the design choice of the compressor. To provide broadest GDD control range, glass slabs are added to the beam path which add group delay to the VIS and NIR beams and causes temporal mismatch.

4.2.5.5 Fixed channel polarization

When performing routine measurements, an interesting behavior was noticed when VIS and fixed wavelengths were used to generate non-resonant CARS from the glass coverslip. VIS channel was tuned to 831 nm to target 2278 cm^{-1} wavenumber and the delay line of the fixed channel was moved to perform a spectral scan. Since glass does not have any resonant peaks at the region, a Gaussian non-resonant background was expected. However, two peaks were recorded in the measurement as depicted in Figure 4.12a. It was assumed that the polarization of the fixed channel beam was not purely linear as it is used to pump the OPO. Due to birefringent properties of the materials inside the OPO, different polarization pulse components are separated in time and cause two peaks in the CARS signal when the fixed channel power is strongly attenuated. The problem was solved by placing a Glan-Taylor polarizer (GT10-B by Thorlabs) just after the pulse exit which blocks the unwanted polarization and works as a filter. The improved results are presented in Figure 4.11b.

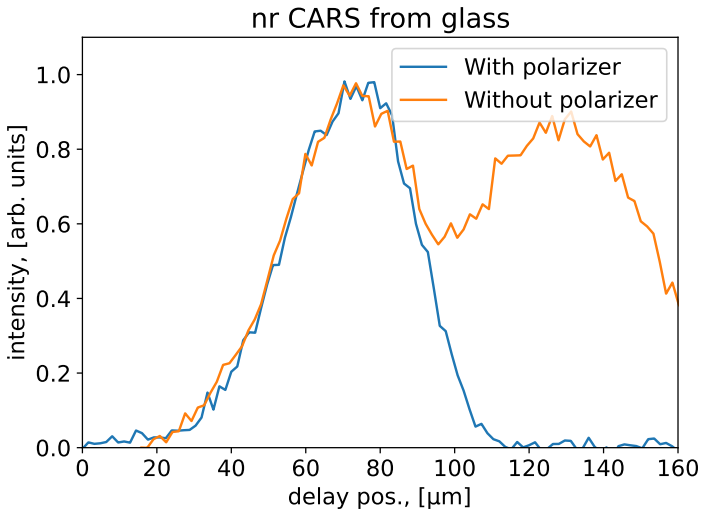

Figure 4.12: During delay scan at strong attenuation, two CARS non-resonant background peaks are observed. The problem was solved by placing a Glan-Taylor polarizer in front of the fixed channel which filters out the unwanted polarization and only leaves linear polarization.

4.2.5.6 Setup transmission

After assembling the setup, the transmission of the beam preparation up to the galvo mirrors was measured For the measurements, a power-meter was used (2A-V1-SH-VYC by Ophir). The transmission versus wavelength for both VIS and NIR beam is presented in Figure 4.13. The fixed wavelength channel power was measured to be 0.7 W.

Some power fluctutations were visible in the VIS channel in the range from 800 nm to 900 nm. After investigation, it was found out that the fluctutations come from the OPO and the problem was fixed by performing OPO calibration. The gap from 950 nm to 1050 nm arises from the dichroic mirrors used to combine all three beams. The transmission, starting from 1 W, is between 30 and 50%. The dominant

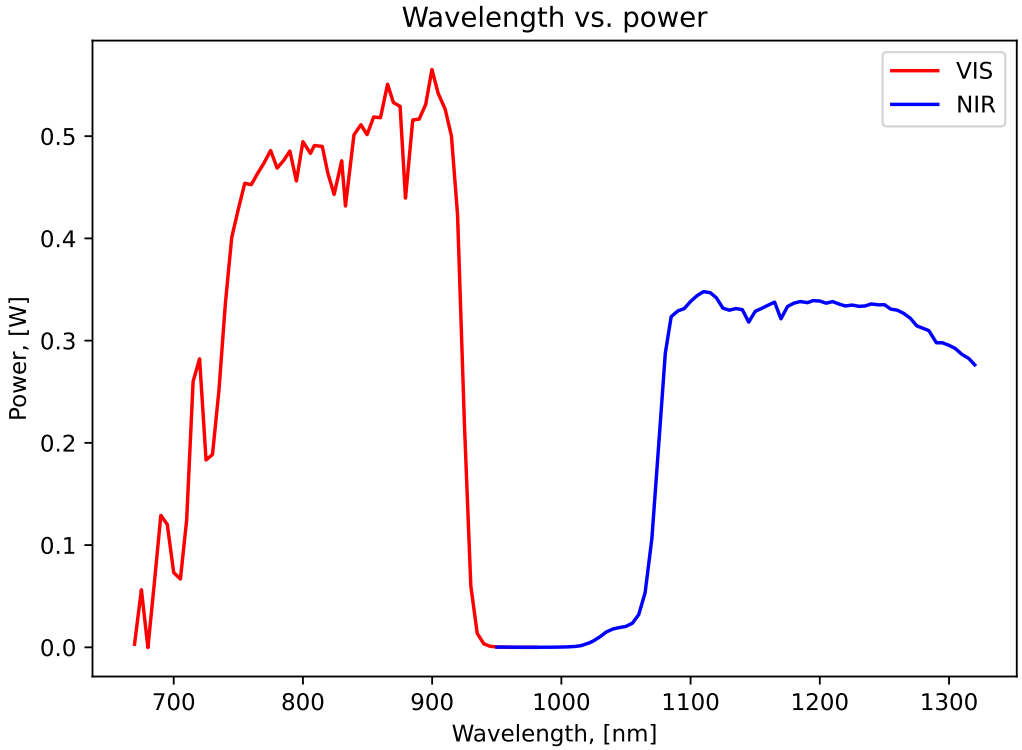

Figure 4.13: The transmission for VIS (red curve) and NIR (blue curve) beams versus their wavelength. Power was measured just before the galvo-mirrors. The initial powers from the source were around 1 W

losses are and the reason is multiple glass blocks which are in the setup and cause reflections from the surfaces. However, the power is sufficient for SHG/THG/CARS microscopy.

4.2.6 Delay line calibration

The delay line calibration relating displacement to wavenumbers is an important step for measurement accuracy. It was performed by using 4-Nitrophenylacetonitrile ($> 98\%$, Sigma Aldrich) sample for the silent region with a well distinguished peak at 2250 and olive oil (mechanically extracted extra virgin olive oil) sample for the C-H stretching peak at $2850\,\mathrm{cm}^{-1}$. For the C-H channel, pump and variable Stokes beams were set to the designated wavenumbers for which the calibration procedure needs to be performed and the power was set to 10 mW each. The PMT 2 integration time was set to 50 ms and the delay line was moved incrementally by 12.5 µm across the region of pulse overlap. Since the delay line begin p_b, end p_e and spectral peak position p_p in steps together with spectral peak position in wavenumbers d_p is known, it is possible to convert them into the wavenumber begin d_b and end d_e positions using $d_\mathrm{b} = d_\mathrm{p} - (p_\mathrm{p} - p_\mathrm{e})2t_\mathrm{s}b$ and $d_\mathrm{e} = d_\mathrm{p} - (p_\mathrm{e} - p_\mathrm{p})2t_\mathrm{s}b$ where $t_\mathrm{s} = 4.17\,\mathrm{fs/step}$ and $b = 0.035\,\mathrm{cm}^{-1}/\mathrm{fs}$ which is calculated from (2.61) relates temporal delay with delay line step. Points $d_\mathrm{b} < x < d_\mathrm{e}$ were linearly interpolated. For the silent region PMT 1 calibration, the pump and Stokes power was set to 2 mW and a 50 kHz electrical filter (EF124 by Thorlabs) was placed directly after the PMT 1 to filter out unwanted noise. The power was reduced due to avoid sample damage. The rest

of the procedure was identical. Delay line and GDD calibration graphs are presented in Figure A.2.

4.2.7 Results

4.2.7.1 Beads

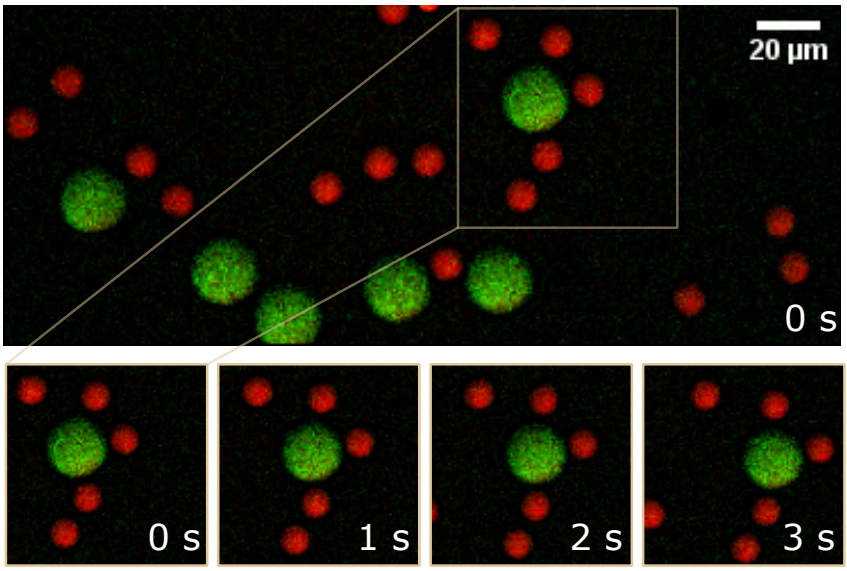

Figure 4.14: CARS images of flowing PS and PMMA beads taken with 0.5 s frame time, 400 × 400 total pixels and 3.125 µs pixel dwell time. The maximum registered intensity of PMMA beads with PMT 2 was 15 counts per pixel which was converted into an 8-bit image and placed in the green channel. The maximum registered intensity of PS beads with PMT 1 was 0.98 V per pixel with 2×10^6 gain which was converted into an 8-bit image and placed in the red channel. Bottom images show a time-course of a selected area as indicated with 1 s intervals to exemplify the flow.

To demonstrate the absence of motion artifacts in dual CARS, a sample containing flowing polystyrene (PS) and polymethyl methacrylate (PMMA) beads (see section 4.2.4.1) was measured. The pump and tunable Stokes beam were set to 827 nm and 1093 nm centre wavelength, respectively, and to 20 mW power each at the sample. By adjusting the delay line, the IFD was set to about 3050 cm^{-1} where the PS vibrational resonance provides strong CARS while CARS from PMMA is suppressed due to the destructive interference of resonant and non-resonant contributions [71]. The fixed Stokes beam was also set to 20 mW and its IFD to about 2336 cm^{-1}, non-resonant for both PMMA and PS. Acquiring both CARS signals simultaneously allows to color-code the beads without having motion artifacts even when the beads are moving. An image illustrating artifact-free imaging of a dynamic sample is presented in figure 4.14. The 20 µm PMMA beads have a dominant PMT 1 signal shown in the green channel, while their signal in PMT 2 shown in the red channnel is suppressed as expected. Conversely, the 10 µm PS bead have a strong PMT 2 and are therefore appearing red, while their green channel PMT 1 is much weaker. The two bead materials are thus well separated by the dual CARS. To exemplify the flow dynamics of the beads, a time-sequence with 1 s time step is shown for a selected region. Clearly, the beads are moving significantly, with a

speed of a few microns per second, without creating motion artefacts in the chemical assignment seen by the color.

4.2.7.2 Oil / water / heavy water emulsion

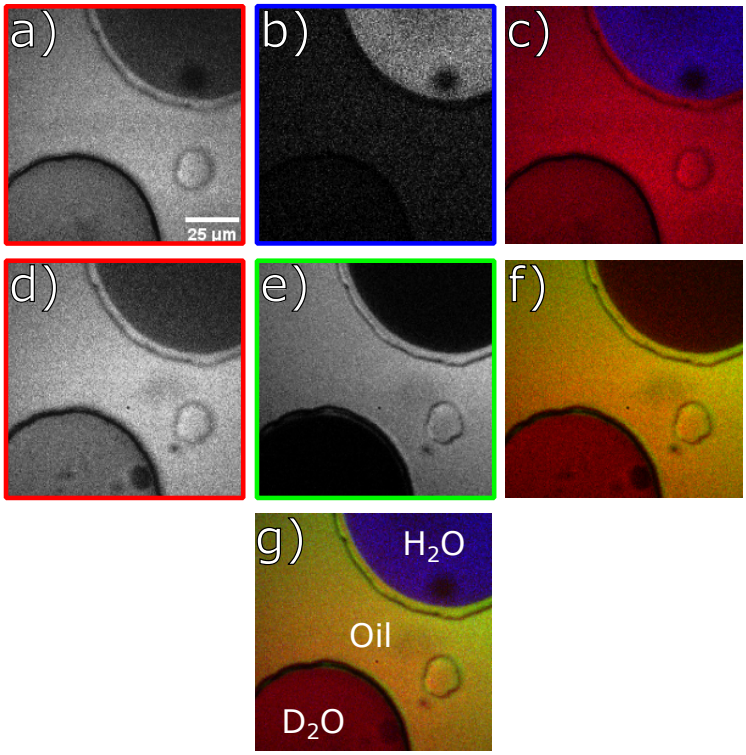

Figure 4.15: CARS imaging on a oil / water / deuterated water reverse emulsion showing water droplets inside oil. Images (a) and (d) show PMT 1 at 2400 cm^{-1} resonant to the C-D stretch of deuterated water, on a scale from 0 (black) to 0.68 V (white). (b) shows PMT 2 at 3080 cm^{-1} obtained simultaneously with (a), at the minimum of the oil CARS signal, on a scale from 0 to 25 counts. (c) is a RGB color overlay with (a) in the red and (b) in the blue channel. (e) shows PMT 2 at 2850 cm^{-1} providing the highest oil CARS signal, on a scale from zero to 100 counts and is obtained simultaneously with (d). (f) is a RGB color overlay with (d) in the red and (b) in the green channel. (g) is a combined overlay of (a) in red, (b) in blue and (e) in the green channel, revealing water in blue, deuterated water in red, and oil in yellow. Interestingly, not only water droplets, but also a water vesicles can be seen, stabilised by the surfactant. Frame time was 2 s with 400 × 400 pixels and 12.5 µs pixel dwell time. Pump and fixed Stokes beam power was set to 20 mW while the variable Stokes power was set to 15 mW.

To demonstrate the imaging of a three component mixture with resonances in the silent region, a sample containing an oil - water - heavy water reverse emulsion (see Sec. 4.2.4.2) was measured. To target water, deuterated water and oil vibrational frequencies, the pump beam was tuned to 831 nm to address with the fixed Stokes beam the deuterated water C-D stretch[88] at 2400 cm^{-1}. Both delay lines were calibrated according to the procedure described in the previous subsection. An example of a resulting PMT 1 image is given in Fig. 4.15(a). Simultaneously, the pump and the variable Stokes beam at 1110 nm addressed at 3080 cm^{-1} a minimum

of the oil signal[88] due to the destructive interference of the resonant signal and the non-resonant background. The resulting PMT 2 is shown in (b), and combined with (a) in the red-blue color overlay in (c). The variable Stokes beam together with the delay line was then tuned to 1072 nm to address the oil resonance at 2850 cm^{-1}, and the resulting simultaneously acquired PMT 1 and PMT 2 are given in (d) and (e), respectively, with a red-green color overlay in (f). Using all three IFDs measured, the overlay of (a) in red, (b) in blue, and (e) in green shown in (g) clearly identifies the three different materials. The advantage of having a two variable wavelength beams with one fixed wavelength beam is the ability to distinguish three different materials with two independent scans.

4.2.7.3 Deuterated Human cervical carcinoma cells

Dual CARS imaging capabilities were tested by imaging deuterated lipids in fixed human cervical carcinoma (HeLa) cells which were prepared as detailed in previous section. The HeLa cells were imaged with a pump at 831 nm and the tuneable Stokes at 1093 nm to address the non-deuterated lipid region, while using the fixed Stokes at 1025 nm for the deuterated lipid region. The power at the sample was 27 mW for the pump, 18 mW for the tunable Stokes and 16 mW for the fixed Stokes beams. A sequence of 20 images of 400×400 pixels with 375 µs pixel dwell time were taken at different IFDs by moving both delay lines by 62.5 µm between images, corresponding to 29 cm^{-1} IFD shift. Results are given in Figure 4.16. The spectra averaged over a selected lipid droplet (see squares Figure 4.16c,d) showing signal from deuterated lipids are presented in Figure 4.16a for the C-H signal at PMT 2 and in Figure 4.16b for the C-D signal at PMT 1. CARS spectra of deuterated lipids are given in [88], showing vibrations across the region 2070—2200 cm^{-1}.

The ratio between signal at droplets and away from droplets is shown as black line—featuring the typical dispersive shape of a weak resonance in CARS. In order to extract a better contrast, images I_1 and I_2 at two IFDs, indicated by the vertical dashed lines, have been selected and their weighted difference $I_\Delta = I_1 - \alpha I_2$ using a weight α has been calculated to provide contrast for the lipid droplets both in the C-H and C-D range. Images in Figure 4.16c and d show these spectrally unmixed data, using $\alpha = 1.26$ for the C-H region and $\alpha = 2.29$ for the C-D region to match the mode of the image values before subtraction. Color overlays of αI_2 and I_Δ image are also shown.

From the I_Δ images it can be observed that the setup is sensitive to deuterated lipids which are imaged simultaneously with the regular lipids inside HeLa cells. The CARS signal from the deuterated lipid region is weak due to small amount of C-D bonds in the sample.

4.3 Conclusions

To summarize, SHG and THG imaging was performed with CRONUS-2P and the results were compared with a single output FLINT oscillator. Comparable performance allowed to proceed and introduce dual CARS imaging modality and image cell silent together with C-H stretch regions simultaneously with calculated 12.2 cm^{-1} spectral resolution by applying spectral focusing scheme [60]. Experiments were performed on PS, PMMA, water, heavy water, regular HeLa cells and deuterated HeLa cells. It can be concluded that the system is sensitive enough to separate deuter-

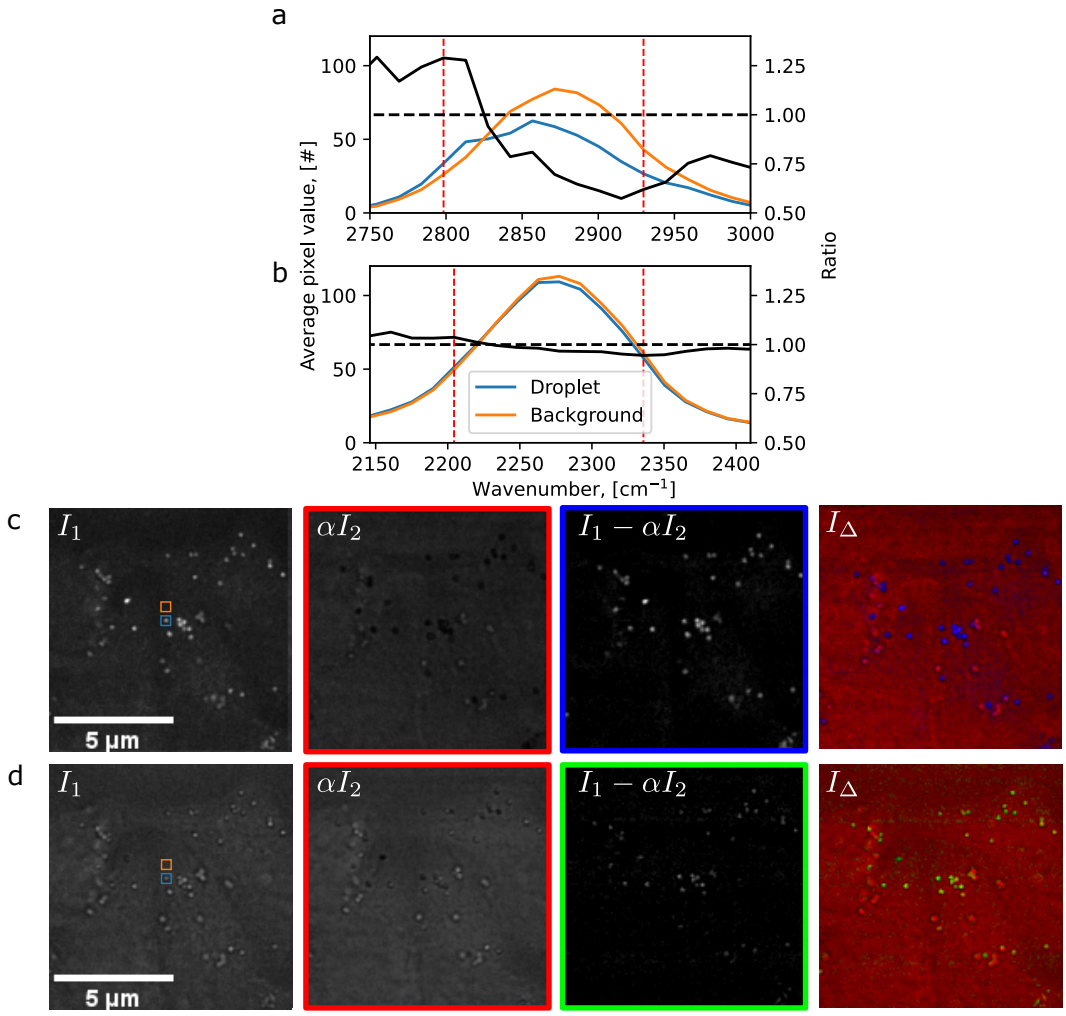

Figure 4.16: Deuterated lipid droplets in fixed HeLa cells imaged with dual CARS. The average signal over a 6×6 pixel square of background (orange) or a droplet (blue) regions of PMT 2 (a) and PMT 1 (b) are given as solid lines, with the ratio droplet and background given as black line. The vertical red dashed lines indicate the spectral positions of the images I_1 and αI_2 shown in (c) and (d), with $\alpha = 1.26$ and $\alpha = 2.29$, respectively. Greyscale black to white over 0 to 5 counts in (c) and 0 to 0.22 V in (d). $I_\Delta = I_1 - \alpha I_2$ is shown, and the color-coded images to the right are overlays of αI_2 in red and I_Δ in blue (c) and green (d).

ated Hela cells from regular HeLa cells and to perform imaging without introducing motion artifacts on rapidly moving beads.

Chapter 5

Wide-field CARS

5.1 Introduction

Wide-field CARS microscopy is a relatively unexplored method which does not get as much attention as raster-scanning. The most attractive part of the wide-field imaging is the wide field of view with low power density. However, the drawbacks are a strong background as signal is generated not only the image plane and the corresponding missing z sectioning of the sample. Also, the phase matching condition is harder to fulfill as beams instead of being focused and thereby containing a wide wavevector range with a short interaction length, are rather collimated, having a well defined wavevector and a long interaction length across the whole sample. One of the ways to do wide-field CARS is by using non-colinear pump and Stokes excitation beams resulting in a dark-field configuration due to the lack of phase matching condition when a homogeneous sample is used [89, 90, 91]. By introducing an angle between pump and Stokes beams, phase matching condition is only completed when the sample is not homogeneous and introduces scattering, providing a required wavevector for phase matching to take place. This allows measurements with good signal-to-noise ratio with reduced non resonant background.

5.2 Collimated wide-field CARS

5.2.1 Setup

A classical wide-field setup was assembled at Light Conversion facility to test the light sources consisting of amplified oscillator (PHAROS by Light Conversion) and OPA (ORPHEUS-F by Light Conversion). The laser emits 280 fs pulses at 1020 nm and operates at a maximum 200 kHz repetition rate which can be reduced by pulse-picking. The pulse energy is 100 µJ resulting in a maximum average power at 20 W. The signal of the OPA is tunable from 640 nm to 940 nm and the idler accordingly tunes from 2300 nm to 1200 nm. The OPA is able to produce broadband signal pulses which can be compressed to 60 fs by an external compressor or spectrally limited 280 fs pulses. For a better spectral resolution, narrowband pulse was used throughout the experiments. The power of pulses is controlled by a half-wave plate and a Glan-Taylor polarizer. The Stokes beam is delayed by an external delay line (8MT50 by Standa) to adjust the temporal pulse overlap with the pump. The size of the beams is matched by using convex-concave (+200, -50 and +200, -100 focal distance by Eksma optics) lens pair which work as a telescope and pulses are spatialy

overlapped by a dichroic mirror (87-041 by Edmund optics). The pulses are then collimated onto the sample where CARS signal is generated. The CARS signal is filtered by band-pass filters (LP0700, SP0750 and BP645-75 by Thorlabs) and collected by a low N.A. obective (CFI Plan Fluor 10×/0.30 N.A. by Nikon). The generated signal is directed to camera (Orca fusion, C14440-20UP by Hamamatsu). The setup is presented in Figure 5.1.

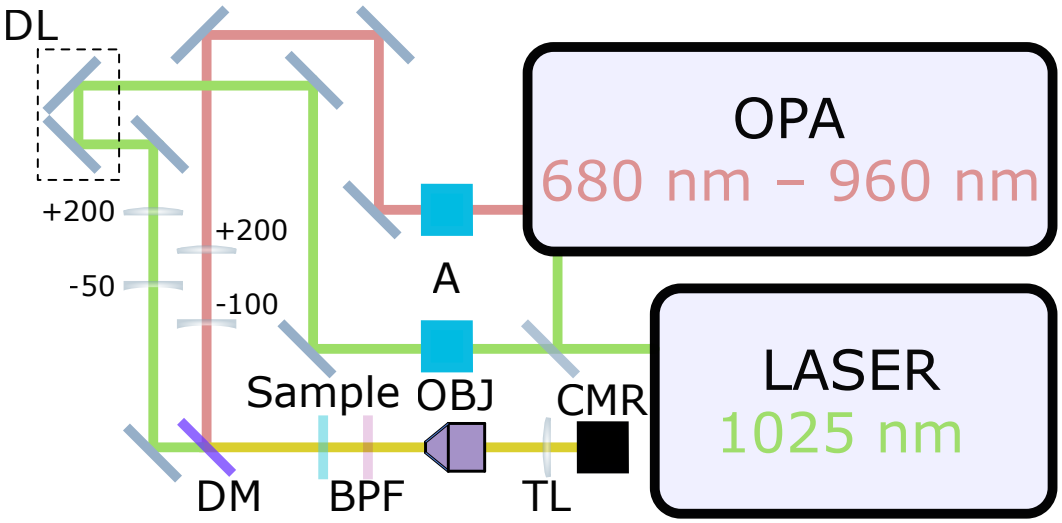

Figure 5.1: Wide-field setup (a) used for SHG and CARS microscopy. Here: A, power attenuator; DL, delay line; DM, dichroic mirror; BPF, band-pass filters; OBJ, objective; TL, Nikon tube lens. Numbers show focal distances of the lenses that were used to reduce the beam size.

It is important to mention that due to limited space the light sources were placed on a different optical table than the rest of the setup. For this reason, it was crucial to make sure that the laser stability sufficient. To test this, a camera was placed just after the power attenuators with multiple neutral density filters and beam coordinates were recorded for 5 minutes. The results were compared with the reference data taken when the camera was placed on the separate optical tables. Also, in between measurements, table pneumatic damping mechanism was turned on and off to observe any possible differences. The experimental setup is presented in Figure 5.2a,b. The obtained results are presented in Figure 5.3. Placing light sources and microscope on different optical tables does not influence beam stability significantly. In the worst case scenario, when the OPA is on a different optical table with pneumatic damping, the beam center offset motion is 120 μm at worst. Since the beam size is around around 8 mm this corresponds to 1.5 % of the beam diameter. In the reference plot, when the light sources and the camera is placed on the same optical table, the beam center fluctuation is 1 %. For the laser, when the optical table is with pneumatic damping, the beam center offset is 0.8 %. The data shows that having light sources and microscope on different tables does not cause significant stability problems. Therefore, it was decided to keep the instruments on different optical tables with pneumatic damping turned off.

5.2.2 Results

SHG image obtained with wide-field laser excitation by replacing filters described in the setup with a BP520-40 by Thorlabs. The obtained results of unstained human

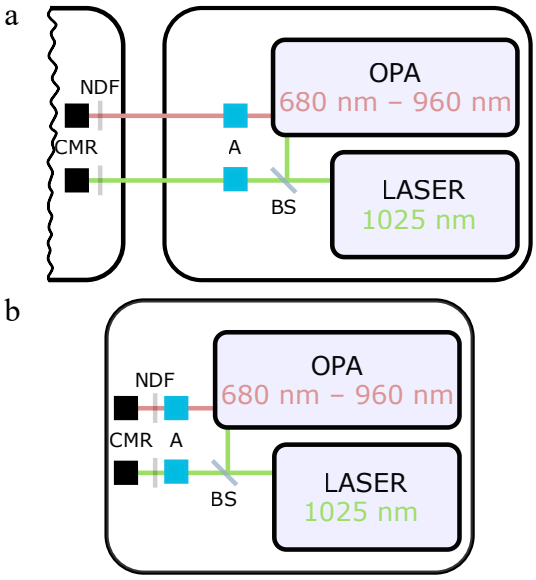

Figure 5.2: Beam stability measurements. a) detection and light sources are on different optical tables. Here: BS, beamsplitter; NDF, neutral density filters; CMR, camera. b) Light source and detection camera are on the same table.

skin tissue sample are presented in Figure 5.4.

Figure 5.4 shows a small SHG signal and a high background. It was reasoned that the background comes from the fundamental laser beam which is insufficiently blocked by the filters. To investigate further, the sample was removed and only the background from the laser was measured by changing the pulse energy of the laser and keeping the same repetition rate. By doing this, one can measure the nature of the rising background. The plot showing background signal dependency on the pulse energy is presented in Figure 5.5a. SHG should scale with the square of the pulse energy and linear with the repetition rate, while linear dependency is observed which means that fundamental laser wavelength is the main cause of the signal.

To get quantative measurement of the image quality, signal-to-noise ratio (SNR) was calculated. The calculations were performed by taking two images: image of the sample and image of the background without the sample. the mean pixel value is calculated from the image of the sample and standard deviation is calculated from the image of the background. The signal-to-noise ratio is defined by equation (5.1).

$$\mathrm{SNR} = \frac{(\bar{x} - \bar{y})\sqrt{(n-1)}}{\sqrt{\sum_{i=1}^{n}(y_i - \bar{y})^2}}, \tag{5.1}$$

where $\bar{x}$ is the image pixel value average, $\bar{y}$ is the background pixel value average, y_i is the ith pixel of the background image and n is the total number of pixels in an image.

The calculated SNR from wide-field SHG images as a function of laser repetition rate or pulse energy is presented in Figure 5.5b,c.
The SNR is increasing linearly with repetition rate and with pulse energy. Since repetition rate controls how many photons are scattered by the sample per time duration, increasing repetition rates increases signal-to-noise ratio linearly.

To investigate other non-linear microscopy modalities, CARS microscopy was carried out. For wide-field CARS, the OPA beam was collinearly combined with the laser beam and sent to the sample. Temporal delay was compensated with the delay

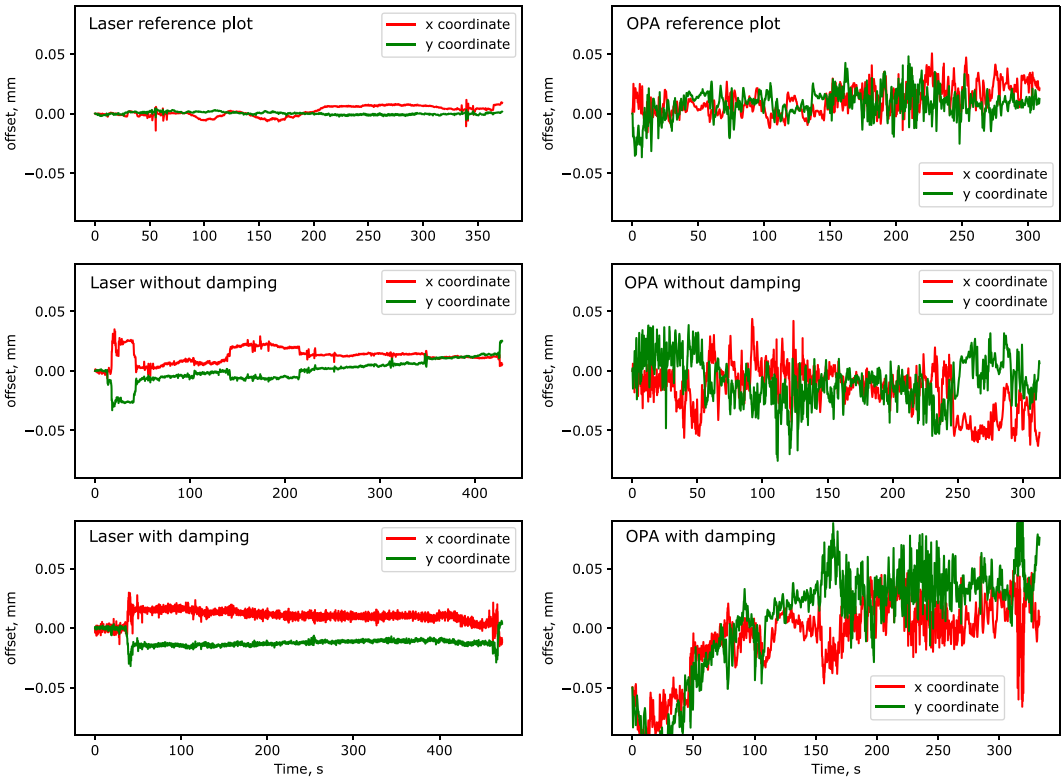

Figure 5.3: Laser and OPA beam stability measurements. Reference plot indicates when the laser and the OPA were placed on the same optical table as the camera. With and without damping measurements indicate when the laser together with the OPA were placed on different damped / undamped optical table than the camera.

line. CARS images of PS beads and unstained breast tissue sample are presented in Figure 5.6. From the initial experiments it was found out that the light sources are suitable for non-linear microscopy. It was decided to ship a similar system to the Institute of Fresnel to continue the experiments.

5.3 Conclusions

By constructing a wide-field CARS microscope and conducting initial experiments, it led to the conclusion that amplified laser system presented in this chapter together with an OPA are suited for wide-field CARS. Since typical CARS microscope uses a single beam to scan the sample and produces pulses in the nJ range, approximately an order of magnitude higher energy is required fo a successful wide-field approach. The drawback of wide-field approach, is a lack of discrimination between z sections of the sample. However, lack of z sectioning capability can be solved by applying other methods, like random illumination microscopy as presented in previous study [34].

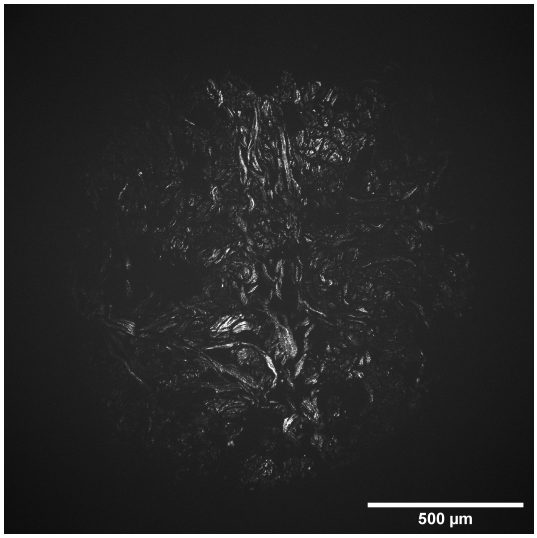

Figure 5.4: Wide-field SHG image of human skin tissue. Integration time, 2 s; laser repetition rate, 50 kHz; SHG wavelength, 510 nm; pulse energy, 4 µJ; greyscale ranges from 0 to 65500 counts; field of view is around 1.7 mm

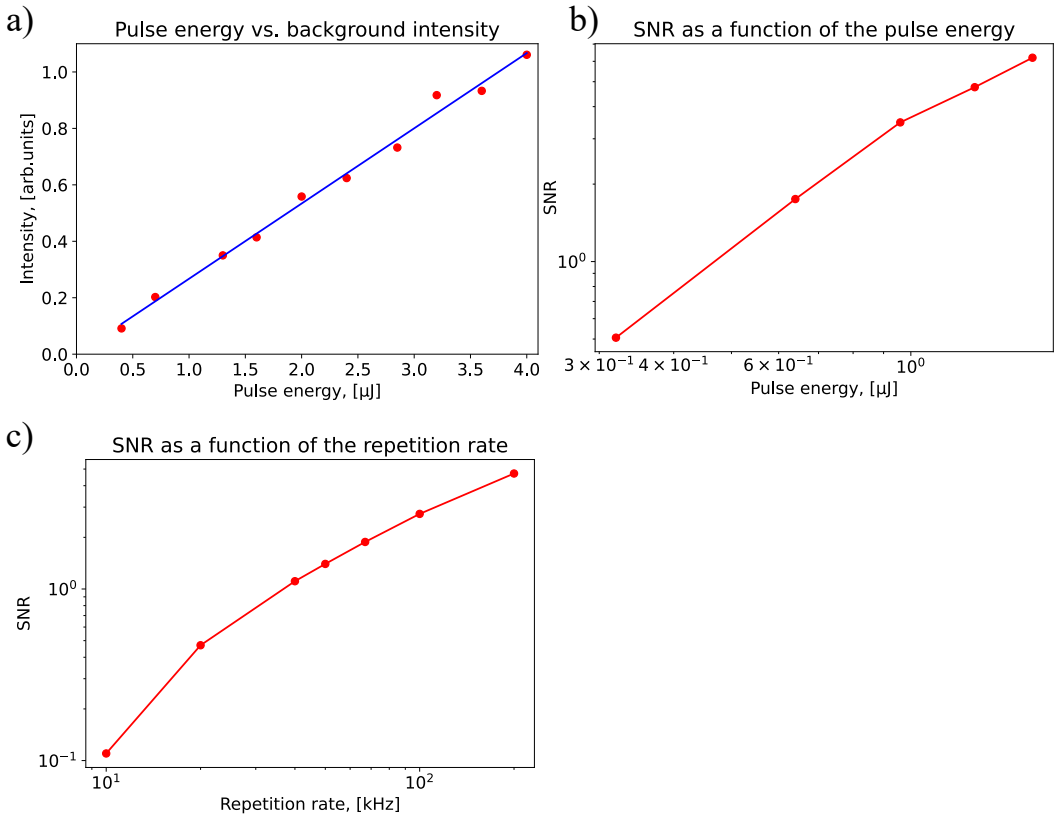

Figure 5.5: Intensity and SNR dependency on pulse energy and repetition rate. Background intensity linear dependency on the pulse energy showing linear fit in blue line a) SNR as a function of repetition rate on pulse energy b) and repetition rate c) of the setup with different camera and different objective. SNR increases with increasing pulse energy since SHG scales quadratically and background is linear with increasing pulse energy.

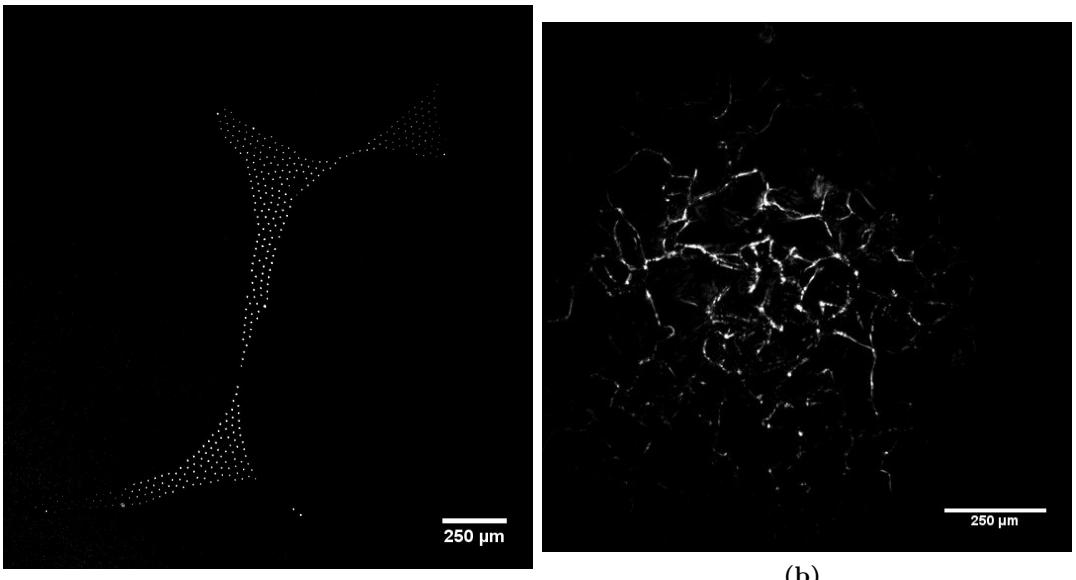

(a) **(b)**

Figure 5.6: (a) dark-field PS bead CARS image. Integration time, 10 ms; repetition rate, 20 kHz; pump wavelength, 784 nm; Stokes wavelength, 1030 nm pulse energy, 1.6 µJ for both beams. (b) wide-field breast tissue CARS image. Integration time, 5 ms; laser frequency, 20 kHz; pump wavelength, 790 nm; Stokes wavelength, 1030 nm pulse energy, 1.6 µJ. Beam size on the sample was around 1 mm. Greyscale ranges from 0 to 300 pe.

Chapter 6

Multifocal CARS

Conventional single focal point raster scanned CARS microscopy is a well established method capable to demonstrate video rate imaging with high resolution. The imaging speed limit for such technique is now set by CARS saturation when 100 mW of average power is used at 80 MHz repetition rate [24]. To circumvent this problem, energy of the pulse can be distributed into multiple focal points which leads to multifocal microscopy. The concept of multifocal confocal and multiphoton imaging is known, but has not been exploited for CARS microscopy apart from one publication 15 years ago [92]. This is due to the requirement of high pulse energy lasers which only recently emerged as simple to use systems. As the camera can be used as a multi-segment detector, the spatial resolution of the resulting multifocal CARS image is created by the multiphoton excitation process, as in single point scanning techniques, allowing for deeper penetration into scattering samples. The multi-segment detection suppresses the influence of scattering in the detection imaging leading to a clearer final image. With a high-speed camera and a powerful laser system, multifocal approach can potentially lead to megapixel CARS imaging with >100 Hz frame rate. Here, we present the first demonstration of multifocal CARS with an amplified laser system and with a large number of foci (>1000).

6.1 Setup

The experimental setup used is sketched in Figure 6.1a. An amplified laser system (PHAROS, Light Conversion) provides transform-limited 290 fs pulses of 1020 nm center wavelength at 200 kHz repetition rate and 20 W average power. 5 W of the beam are used as Stokes beam for CARS, and the remaining power is used for an optical parametric amplifier (OPA) (ORPHEUS-F, Light Conversion) which provides 130 fs pulses tunable from 650 to 900 nm used as the pump beam for CARS with 1 W average power at 800 nm. The powers of pump and Stokes are controlled by attenuators consisting of a half-wave plate (by Castech) and a Glan-Taylor polarizer (GT10-B by Thorlabs). The Stokes beam is transmitted through 60 mm of SF-66 glass blocks (II-VI incorporated) and an optical delay line (VT-80 by PI) with silver retroreflectors (by Eksma optics) to control the temporal overlap of pump and Stokes at the sample. Both beams are combined into the same spatial mode by a dichroic mirror (high reflection from 600 to 950 nm and high transmission from 970 to 1300 nm by Eksma Optics) and then pass trough 145 mm of SF-57 glass blocks (II-VI incorporated) for spectral focusing [60]. The pump at 785 nm accrues 33350 fs^2 of GDD, which stretches it to 723 fs, while the fixed Stokes accrues

34450 fs^2 GDD which stretches it to 439 fs. Both beams then pass a long-pass filter (FEL0700, Thorlabs) to remove components below 700 nm wavelength, spectrally overlapping with the CARS signal (mostly residuals of the white-light generation seed of the OPA) and a Galilean beam expander (-50 mm focal length plano-concave lens and 150 mm focal length plano-convex lens by Casix) which expands the beam from 3 mm to 9 mm. The beams then are focussed by a silica microlens square array (15-811, Edmund Optics) of 10×10 mm^2 size, 300 µm pitch, and 8.7 mm focal length, creating 33×33 focal spots. The generated beamlets are collimated by an achromatic doublet (PO-PK-L3 by II-VI incorporated) of 100 mm focal length, and are merging at its back-focal plane, which is located between the x-y galvo mirrors (6215H, Cambridge Technology) scanning the beam directions. The beamlets are then relayed with four-times magnification (closely-spaced pair of AC300-100-B and a AC508-200-B-ML, Thorlabs), expanding the beamlets to 13.8×13.8 mm^2 square size and imaging the galvo mirror mid plane to the 15 mm diameter back focal plane of the excitation objective (plan apo lambda 20× 0.75 NA, MRD00205, Nikon), which focuses the beamlets into the sample. The transmitted light is collected by a second objective (plan apo VC 20× 0.75 NA, 1501-9398, Nikon) and passes through a short-pass and a band-pass optical filter (FESH0750 and FB650-40, Thorlabs) to isolate the CARS signal. A tube lens of 50 mm focal length and F/2.8 opening (NMV-50M23 by Navitar) then images the sample with a magnification of 5 onto a camera of 2448×2048 pixels of 3.45 µm size, $\sigma_r = 2.44$ e read noise, 10 ke full well capacity, USB3.1 interface (BFS-U3-51S5M-C by Flir). The F/2.8 opening provides a 18 mm aperture, accommodating the 15 mm diameter of the collection objective back focal plane and allowing for some off-axis beam walk-off. We note that the 5 times magnification onto the camera is below the 7 times required for Nyquist sampling. This reduces the number of pixels to be read per focal spot, improving read noise and speed. The camera is triggered via the software driving the galvos with a frame rate ν_f, and the exposure time τ_e is set to allow this frame rate, which requires $\tau_e + \tau_d < 1/\nu_f$ using a delay time $\tau_d = 75$ µs. The camera is read at 8-bit pixel format for highest speed, via a software written in LabView, and the frames are saved as bitmaps and processed off-line. For detection, a camera was used with analog gain g_c of 10dB, 20dB or 30dB, providing 14.6, 4.61, or 1.46 e/count in 8-bit readout, respectively. A digital offset of 5 counts was used to avoid zero-clipping. The dark signal was measured by averaging 900 frames was subtracted from each frame before further processing. Powers of excitation beams given are measured at the sample. A more visual sketch of excitation and detection part is presented in appendix Figure B.7.

6.2 Sample preparation

Sample O used as a homogeneous reference was prepared by pipetting 10 µL of olive oil (Bio Basso by Basso Fedele & Figli srl) onto a glass coverslip (#1.5, 24×50 mm^2, Thermo Scientific) and was spread across by adding a second equal coverslip for imaging.

Sample A was prepared by pipetting 10 µL of 1% solid suspension PS beads of 2 µm diameter (124, Phosphorex) onto a glass coverslip (#1.5, 24×50 mm^2, Thermo Scientific). The mixture was left to dry at ambient conditions and 10 µL of distilled water was pipetted onto the coverslip and spread across the sample by adding a second equal coverslip for imaging.

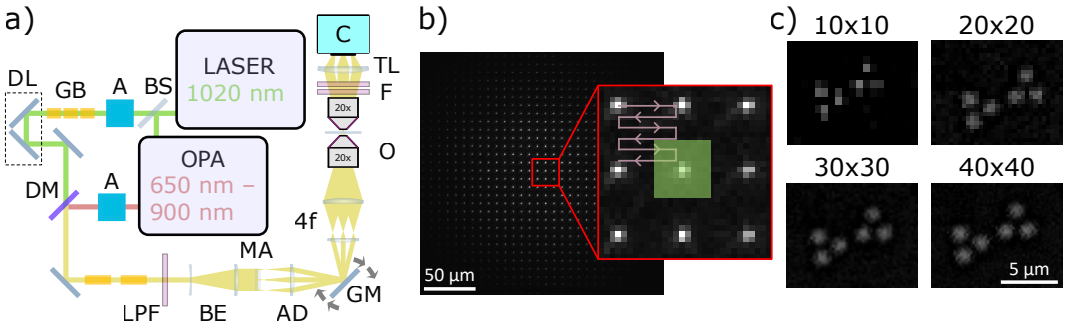

Figure 6.1: a) Multifocal CARS experimental setup. BS, beamsplitter; A: power attenuator; GB, glass blocks; DL, delay line; DM, dichroic mirror; LPF, long-pass filter; BE, beam expander; MA, microlens array; AD, achromatic doublet; GM, galvo mirrors; 4f, 4f relay system; O, objective; F, spectral filters; TL, tube lens; C, camera. b) Multifoci raster-scan pattern. At each galvo-mirror position an image of the signals from all focal points is acquired. The pixel values within an square area (green) of $S_{\mathrm{int}} = 10$ pixels side length centred each focal point are summed to provide the focal point signal. $g_{\mathrm{c}} = 20\,\mathrm{dB}$, $\tau_{\mathrm{e}} = 4\,\mathrm{ms}$, $\nu_{\mathrm{f}} = 195\,\mathrm{Hz}$, grey scale black to white 0 to 1382 pe. c) Examples of reconstructed images of 2 µm PS beads (sample A) for position grids of $N_{\mathrm{g}} \times N_{\mathrm{g}}$ points for N_{g} of 10, 20, 30, and 40.

Sample B was prepared by mixing 10 µL of 1% solid suspension of polymethyl methacrylate (PMMA) beads of 20 µm diameter (MMA20K, Phosphorex) and 10 µL of 1% solid suspension polystyrene (PS) beads of 10 µm diameter (118, Phosphorex) on a glass coverslip as above. The mixture was left to dry under ambient conditions for 30 mins. Subsequently, 10 µL of olive oil was pipetted onto the coverslip and spread across the sample by adding a second equal coverslip for imaging.

Sample C used to demonstrate PSF was prepared by pipetting 10 µL of 1% solid suspension PS beads of 0.5 µm diameter (108, Phosphorex) onto a coverslip as above and dried at ambient conditions.

Sample D was prepared by slicing a thin piece of potato and rubbing it on a coverslip (#1.5, $24 \times 50\,\mathrm{mm}^2$, Thermo Scientific). The moist substance left on the coverslip was closed with a second coverslip and placed under a microscope for multifocal imaging procedure.

Human skin samples were prepared by fixing them with 10 % formalin and dehydrating with ethanol. The embedding was performed by using paraffin and the sample was sectioned with a microtome. The sample was stained by using a standard eaosin and hematoxylin staining procedure [93].

6.3 Image acquisition

The CARS signal generated in the sample is imaged onto the camera, showing the 33×33 grid of beamlet foci, as shown in Figure 6.1b for the homogeneous sample O. The intensity of each focus is varying across the array due to the variation of the beam intensity across the lenslet array considering the pump and Stokes excitation beams of Gaussian beam diameter (at $1/e^2$ intensity) around 9 mm, entering the array, resulting in a gradual reduction towards the periphery of the array. Notably, CARS is a third-order signal proportional to $I_{\mathrm{p}}^2 I_{\mathrm{s}}$, with the pump intensity I_{p} and the Stokes intensity I_{s}, resulting in a diameter of the CARS intensity a factor of

$\sqrt{3}$ smaller, of about 5 mm. In this work, two imaging methods were used named excitation imaging and detection imaging. Excitation imaging works by selecting a certain area around each focal point and finding a total number of pixel counts in that area. Each area around a focal point represents a single pixel in the final image so the final image is populated by moving galvo mirrors. Detection imaging works by recording an image at each galvo mirror position and summing all images into a final image.

The galvo-mirrors are used to shift the foci in a raster-scan pattern with N_g steps in each direction, filling the space between foci, as sketched in Figure 6.1b. An image P_{kl} is acquired at each rasterscan index (k, l) in x and y direction for $k, l = 0, 1, .., N_g - 1$. The foci are separated by 7.5 µm on the sample, which corresponds to $S_g = 10.9$ pixels on the camera. The focal point positions $\mathbf{r}_{nm}$ of the beamlets of index (n, m) in x and y directions, $n, m = 0, 1, .., 32$, are determined using the signal peak positions fin the image P_{00} from the homogeneous sample. The camera centering and rotation is aligned so that the central row and column of foci are straight and deviating by less than 0.5 pixels from the horizontal and vertical direction. A second-order polynomial $x(n) = x_0 + x_1 n + x_2 n^2$ is then fitted to the horizontal positions of the central row of peaks ($m = 16$), and equivalently $y(m) = y_0 + y_1 m + y_2 m^2$ to the vertical positions of the central column of peaks ($n = 16$), and the position of any peak is then taken as $\bar{\mathbf{r}}(n, m) = (x(n), y(m))$ for image reconstruction. The second-order terms cater for small cushion distortions of the imaging. The nominal focus positions in P_{kl} are then taken as $\bar{\mathbf{r}}(n+kS_g/N_g, m+lS_g/N_g)$ and are providing the signal for the pixel position $(i, j) = (nN_g+k, mN_g+l)$ in the reconstructed image, having a pixel size on the sample of 7.5 µm$/N_g$.

The pixel value p_{ij} of the reconstructed image is evaluated by summing the pixel values of P_{kl} over a square area with edge size S_{int} centred on the nominal focus positions $\bar{\mathbf{r}}$ (see green area in Figure 6.1b), noting that avoiding overlap between foci requires $S_{int} < S_g$. The number of pixels summed is S_{int}^2, providing a read noise of $\sigma_s = S_{int}\sigma_r$, proportional to S_{int}. The variation of p_{ij} with S_{int} depends on the extension of the imaged signal in P_{kl}. In homogeneous samples the extension is below 2 pixels, as seen in Figure 6.1b, thus choosing $S_{int} = 3$ seems appropriate to achieve highest signal to noise. However, the extension is affected by sample inhomogeneities in the path from the beamlet focus to the camera, as exemplified in Figure B.5. Thus the immunity of p_{ij} against sample inhomogeneities increases with S_{int}, and is maximised for $S_{int} = 10$. Comparison between different S_{int}numbers is presented in Figure B.4. Reconstructed CARS images of 2 µm PS beads (sample A) at 2950 cm^{-1} are given in Figure 6.1c using different N_g, showing the increasing definition of the imaged beads with N_g. Nyquist sampling is achieved for $N_g \approx 30$, providing a resulting pixel size of 250 nm.

The use of the camera to define a multi-segment detector separating the signal of each focus, as opposed to direct imaging, results in significantly improved spatial resolution and signal to noise when imaging inhomogeneous samples. This is exemplified in Figure 6.2a, where the multi-segment analysis is compared to direct imaging given by the sum of all P_{kl}, the latter resembling the image analysis method used in previous multifocal approaches [92, 94]. We used sample A and selected a region with stacked patches of closely packed 2 µm PS beads in water, imaged at different axial planes. A significant blurring and reduced contrast in direct imaging compared to multi-segment imaging is observed. It is noted that the direct imaging pixel size of 0.69 µm is sufficient to resolve the beads. Thus, while the multisegment

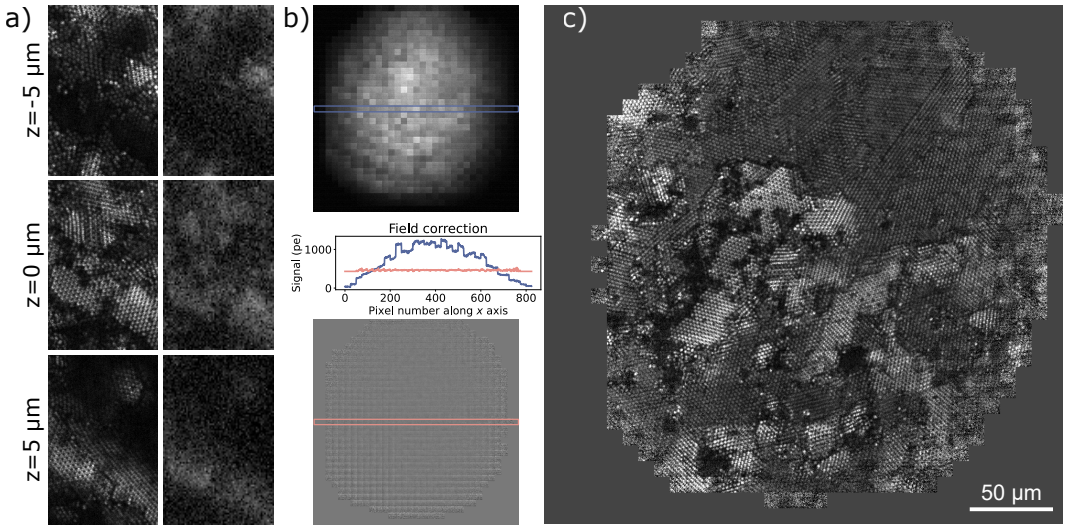

Figure 6.2: a) Excitation imaging (left) compared to detection imaging (right) at different z planes as indicated. CARS of sample A (2 µm PS beads) at 2950 cm^{-1} with 20 mW pump power and 50 mW Stokes power. $N_\mathrm{g} = 30$, $\nu_\mathrm{f} = 195$ Hz, $\tau_\mathrm{e} = 4$ ms, $g_\mathrm{c} = 30$ dB, $S_\mathrm{int} = 8$, greyscale 0 to 1399 pe (left) and 0 to 19575 pe (right). b) Correction of beamlet-dependent signal strength. CARS imaging of the homogeneous sample O (oil) at 2850 cm^{-1} with 20 mW pump power and 50 mW Stokes power. Top: image p_{ij} shows a tile structure from imperfections in the microlens array, and vignetting by the excitation beam. $N_\mathrm{g} = 25$, greyscale 0 to 1856 pe. The center cross-section (blue line) is shown below. Applying a flat-field correction (see equation 6.1), the resulting image $\tilde{p}_{ij}$ is rather uniform (bottom, greyscale 0 to 1114 pe) as confirmed by the cross-section (red line). c) Example of a flat-field corrected image $\tilde{p}_{ij}$ of sample A, greyscale 0 to 466 pe, $v = 1/3$, settings as in a).

imaging results in a PSF given by the excitation focus as in single point scanning, direct imaging results in blurring due to sample inhomogeneities, an issue intrinsic to the previous multifocal approaches.

6.4 Image post-processing

Variations between microlenses and different local field distortions lead to variations in the CARS signals from different foci, visible as a vignetting and tile pattern in the image of a homogeneous sample as shown in Figure 6.2b. Moreover, these differences are modulated by sample inhomogeneities. Static, sample independent variations can be corrected using an image of a homogeneous sample and calculating the ratio h_{nm} of the average pixel value over the tile from an individual focus $A_{nm} = \langle p_{(nN_\mathrm{g}+k,mN_\mathrm{g}+l)} \rangle$ to the average value of all tiles $\langle A_{nm} \rangle$. To exclude tiles of low signal, exhibiting excessive noise after correction, tiles with a ratio h_{nm} lower than a threshold value v are set to the average value of the other tiles $\bar{A}_\mathrm{v} = \langle A_{nm} \rangle_{h_{nm}>v}$. The corrected pixel values are accordingly defined by

$$\tilde{p}_{ij} = \begin{cases} p_{ij}/h_{nm}, & \text{if } h_{nm} \geq v \\ \bar{A}_\mathrm{v}, & \text{if } h_{nm} < v \end{cases} . \tag{6.1}$$

The uncorrected pixel values for the homogeneous sample O are presented in Figure 6.2b. A tile structure from imperfections in the microlens array, and vignetting by the excitation beam are visible, and clear in the center cross-section (blue line). Applying a correction for each beamlet (see equation 6.1), the image $\tilde{p}_{ij}$ is rather uniform (Figure 6.2b bottom), confirmed by the cross-section (red). There is a remaining gradient of some ±5% across the tiles, which is attributed to clipping of the excitation beams and the CARS signal by the NA of the objectives and could be reduced optimising the optical layout.

A corrected image for sample A with 2 µm PS beads is presented in Figure 6.2b, showing the high imaging quality achieved. Notably, even after correction, some tiling pattern is still present here, and also in images of other samples which have inhomogeneities. It is attributed to a distortion of the individual foci by the sample, which can reduce or increase the CARS signal depending on the distortions present without the sample due to the imperfection of the microlens array. Therefore the relative intensity of the foci does depend on the refractive index inhomogeneities of the sample itself, and thus cannot be fully cancelled by a reference measurement on a homogeneous sample. These effects could be mitigated using a higher quality microlens array and optimising the optical layout.

As alternative and addition to hardware improvements, an algorithm was developed to minimise the tile pattern *a posteriori*. This algorithm determines correction factors C_{nm} for each beamlet which are minimising the step heights at the tile edges over all tiles. To do so, we determine the edge ratio of a tile (n,m)

$$u_{nm\rightarrow} = \frac{\sum_l \tilde{p}_{((n+1)N_\mathrm{g}-1,mN_\mathrm{g}+l)}}{\sum_l \tilde{p}_{((n+1)N_\mathrm{g},mN_\mathrm{g}+l)}} \tag{6.2}$$

for the right edge to tile (n, $m+1$), and

$$u_{nm\downarrow} = \frac{\sum_k \tilde{p}_{(nN_\mathrm{g}+k,(m+1)N_\mathrm{g}-1)}}{\sum_k \tilde{p}_{(nN_\mathrm{g}+k,(m+1)N_\mathrm{g})}} \tag{6.3}$$

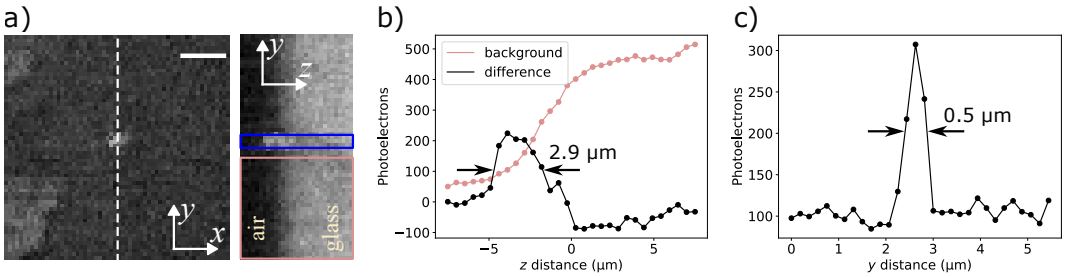

Figure 6.3: a) CARS PSF measured on a 0.5 µm PS bead (sample C) using 30 z-planes with 0.5 µm step. Pump 785 nm, 20 mW and Stokes 50 mW, 3050 cm^{-1}. $N_\mathrm{g} = 40$, $S_\mathrm{int} = 10$, $g_\mathrm{c} = 30\,\mathrm{dB}$, $\nu_\mathrm{f} = 100\,\mathrm{Hz}$. τ_e=8 ms. a) xy and yz sections, greyscale 0 to 583 pe, scale bar 2 µm. b) z-dependent signal of the glass-air interface without PS bead (pink, averaged over pink rectangle in a), with the PC bead (blue, averaged over blue rectangle in a), and their difference (green), showing the axial PSF. c) signal along white dashed line in a) showing the lateral PSF.

for the bottom edge to tile $(n+1, m)$. These edge ratios are modified by applying the tiling correction factors C_{nm}, which are found by minimizing the deviation of the modified ratios from unity defined as

$$C_{nm} = \operatorname{argmin} \sum_{n,m} \left| \log\left(\frac{u_{nm\rightarrow} C_{nm}}{C_{n+1,m}} \right) \right| + \left| \log\left(\frac{u_{nm\downarrow} C_{nm}}{C_{n,m+1}} \right) \right|. \tag{6.4}$$

The double corrected data is then given by $\breve{p}_{ij} = \tilde{p}_{ij} C_{nm}$. An example of values of the tiling correction C_{nm} is shown in Figure 6.5. The working principle of the algorithm was tested on a randomly generated data that simulates different intensity distribution and is presented in the appendix Figure B.1.

6.5 Results

6.5.1 Point spread function

To measure the experimental three-dimensional point spread function (PSF) of the setup, a 0.5 µm diameter PS bead on glass in air (sample C) was imaged. Flat-field corrected images $\tilde{p}_{ij}$ in the x-y as well as y-z planes are presented in Figure 6.3. The in-plane PSF full width at half maximum (FWHM) is 0.5 µm, while the axial PSF FWHM is 2.9 µm, comparable to previous single point scanning data using an 0.75 NA objective [95].

6.5.2 Tilling correction

To demonstrate the efficacy of the tiling correction on biomedical samples of interest, a human skin sample (see section 6.2) was imaged at 2935 cm^{-1} and 2970 cm^{-1}. The resulting data p_{ij} using $S_\mathrm{int} = 10$ is presented in Figure 6.4a. The vignetting due to the excitation beam profiles is clearly visible, together with the tiling. After flat-field correction using h_{nm} from sample O and $v = 1/3$ (see Figure 6.2), shown in Figure 6.4d, the resulting $\tilde{p}_{ij}$ given in Figure 6.4b shows that the vignetting has been corrected, but the tiling, while somewhat reduced, is still clearly visible. The

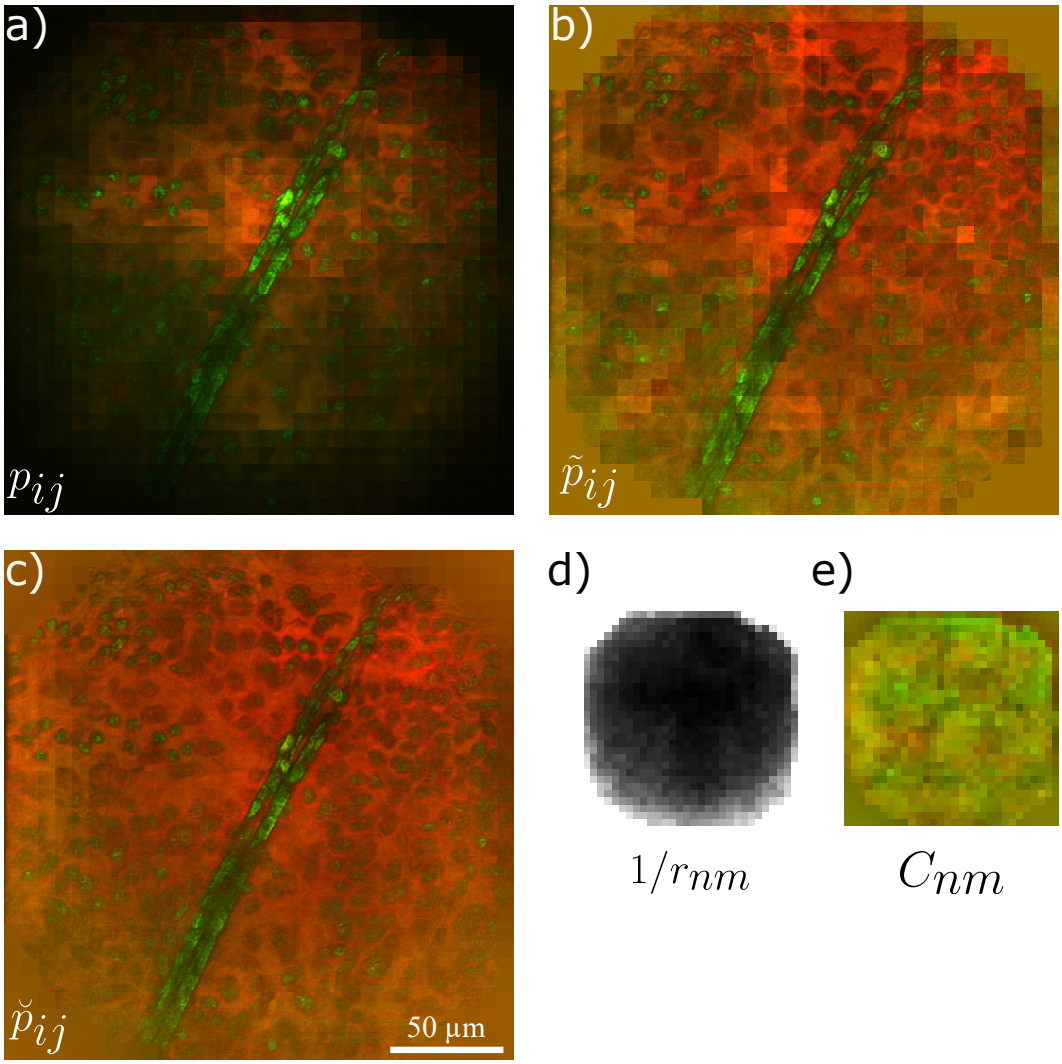

Figure 6.4: CARS false color RGB image of a human skin sample demonstrating the tile-correction. $\nu_\mathrm{f} = 50\,\mathrm{Hz}$, $\tau_\mathrm{e} = 15\,\mathrm{ms}$, $g_\mathrm{c} = 20\,\mathrm{dB}$, $N_\mathrm{g} = 30$, $S_\mathrm{int} = 10$. Pump 785 nm, 18 mW; Stokes 48 mW. CARS was imaged at $2935\,\mathrm{cm}^{-1}$ (red) and then $2970\,\mathrm{cm}^{-1}$ (green) by changing the pump-Stokes delay. a) Uncorrected p_{ij}, range $0 - 10138$ pe for $2935\,\mathrm{cm}^{-1}$ and $0 - 5530$ pe for $2970\,\mathrm{cm}^{-1}$. b) Flat-field corrected data $\tilde{p}_{ij}$, range 0 to 3226 pe for $2935\,\mathrm{cm}^{-1}$ and 0 to 5529 pe for $2970\,\mathrm{cm}^{-1}$. c) Tiling corrected $\breve{p}_{ij}$, same range as in c). d) Flat-field correction factors $1/h_{nm}$ using the glass coverslip of the sample as homogeneous reference, represented as greyscale image from 0 to 4. e) Tiling correction factors C_{nm} with color coding as c) on a range from 0 to 2.

change in the tile pattern shows that the origin of the remaining pattern is different from the tiling in a homogeneous medium. Applying the tiling correction algorithm, yielding the factors C_{nm} shown in Figure 6.4e, the corrected $\breve{p}_{ij}$ given in Figure 6.4c is void of significant tiling. Thus the tiling correction algorithm enables post correction of the images suited for further processing.

6.5.2.1 Three-dimensional bead imaging

To demonstrate the z-sectioning capability on strongly scattering structures, sample B hosting a mixture of 20 µm PMMA beads and 10 µm PS beads in oil was imaged. A z-stack over 10 position with 2 µm increments was measured. Using the different pump-Stokes delays, CARS stacks at 2930 cm^{-1} dominated by oil, at 2950 cm^{-1} dominated by PMMA, and at 3050 cm^{-1} dominated by PS were sequentially recorded. Flat field and tiling correction was applied, and the resulting $\breve{p}_{ij}$ is shown in Figure 6.5. We can see that the method is able to create well resolved z-sectioning also for these samples. Comparing this with the result for image averaging in Figure B.3, the significant advantage of using images created by the non-linear exitation PSF as compared to the PSF of the detection imaging previously used [92, 94] is evident. Nevertheless, the 10 µm PS beads with their large index contrast to olive oil (1.59 to 1.46) provide such large deviations in the detection imaging that the signals from different foci are mixed. This is clearly seen by the shadowing of the lower PS beads by the beads lying on top of them in Figure 6.5a 1-3. Increasing the NA of illumination and detection would likely improve this as the shadowing depends on the collection direction, and averaging over a larger directional range blurs the sharp shadowing.

6.5.3 Potato starch imaging

As potato starch has a high content of carbohydrates which could be targeted with CARS imaging. Initially, CARS signal was recorded. Afterwards, pump beam was turned-off and SHG was recorded by switching CARS filter to SHG filter (FBH520-40 by Thorlabs). Finally, purely transmission data was collected by using only Stokes beam. A composite image was created from the collected data with flat-field and tiling corrections. The resulting images are presented in Figure 6.6. It is noted that even after image corrections, the tile pattern is not fully corrected. This can be explained by the structure of the sample as the starch granules are heavily scattering the light and relatively thick which makes them not well suited for multifocal imaging. Scattering could be improved by embedding starch granules in a better refractive index matched medium.

6.5.4 CARS and SHG imaging of human skin

To demonstrate the performance of the multifocal approach with medically relevant scattering samples, a human skin tissue was imaged (see section 6.2). First, non-resonant CARS was recorded at 2935 cm^{-1} and then the delay was moved to target protein region at 2970 cm^{-1} where CARS resonance images were recorded. To measure SHG of the Stokes, the FB650-40 filter was replaced by a BP520-40 Thorlabs, and the pump was blocked. The glass blocks were not removed for convenience, but we note that the SHG signal would be increased about 4 times by doing so.

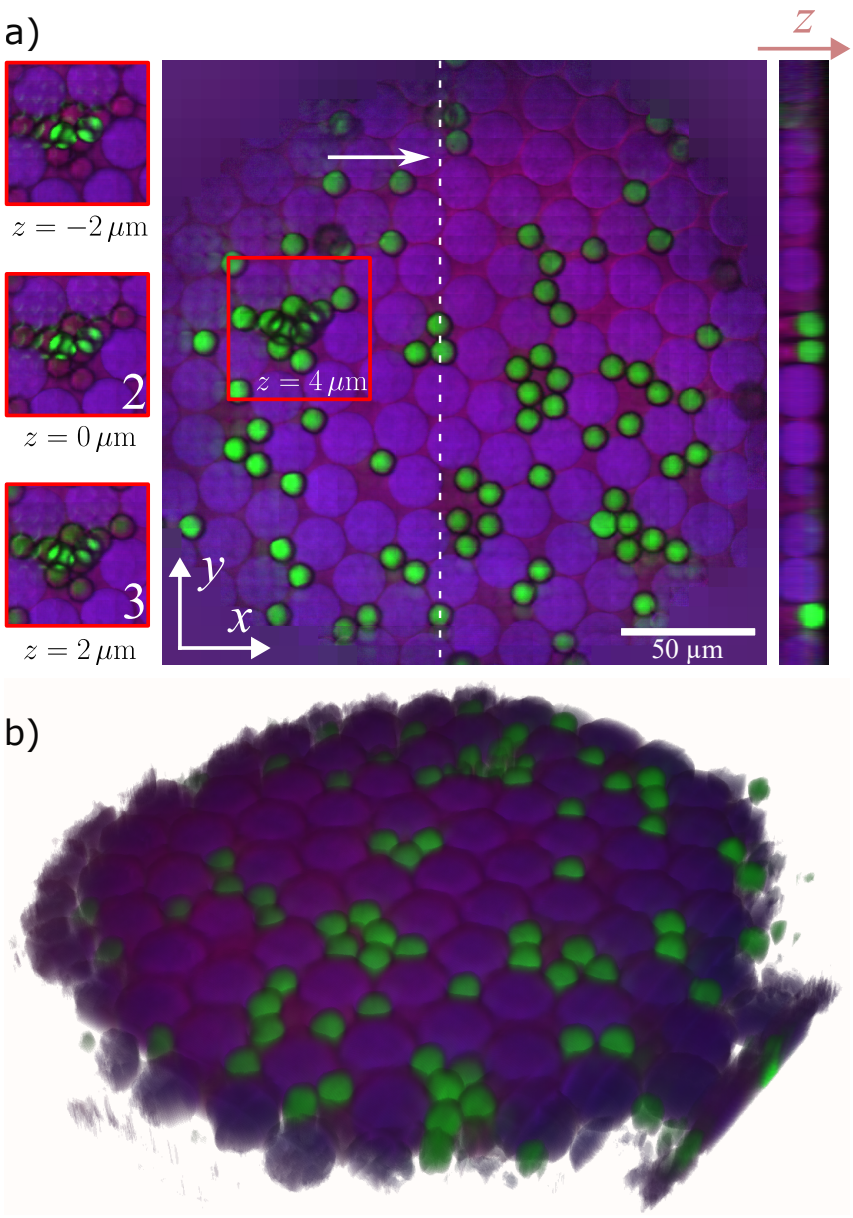

Figure 6.5: Three-dimensional CARS imaging of sample B at 3050 cm^{-1} (green) highlighting the 10 µm PS beads, at 2950 cm^{-1} (blue) highlighting the 20 µm PMMA beads, and at 2930 cm^{-1}(red) showing the oil used as embedding medium. $\nu_\mathrm{f} = 100\,\mathrm{Hz}$, $\tau_\mathrm{e} = 5\,\mathrm{ms}$, $g_\mathrm{c} = 10\,\mathrm{dB}$, $N_\mathrm{g} = 30$, $S_\mathrm{int} = 10$. Pump 785 nm, 10 mW Stokes 50 mW. Stack of 10 z-steps of 2 µm size. a) Images $\breve{p}_{ij}$ after flat-field ($v = 1/5$) and tiling correction using value ranges of 0 to 14600 pe for 2930 cm^{-1}, 0 to 17520 pe for 3050 cm^{-1}, and 0 to 29142 pe for 2950 cm^{-1}. a) $x-y$ section, with a zoom of an area indicated as red square at different z planes with 2 µm increments shown on the left, and a $y-z$ section shown on the right. The white dashed lines indicate the x and z position of the $y-z$ and $x-y$ sections. b) 3D reconstruction of $\breve{p}_{ij}$.

The resulting image encoding all three data as false color is presented in Figure 6.7. Additional CARS and SHG results are presented in appendix Figure B.2.

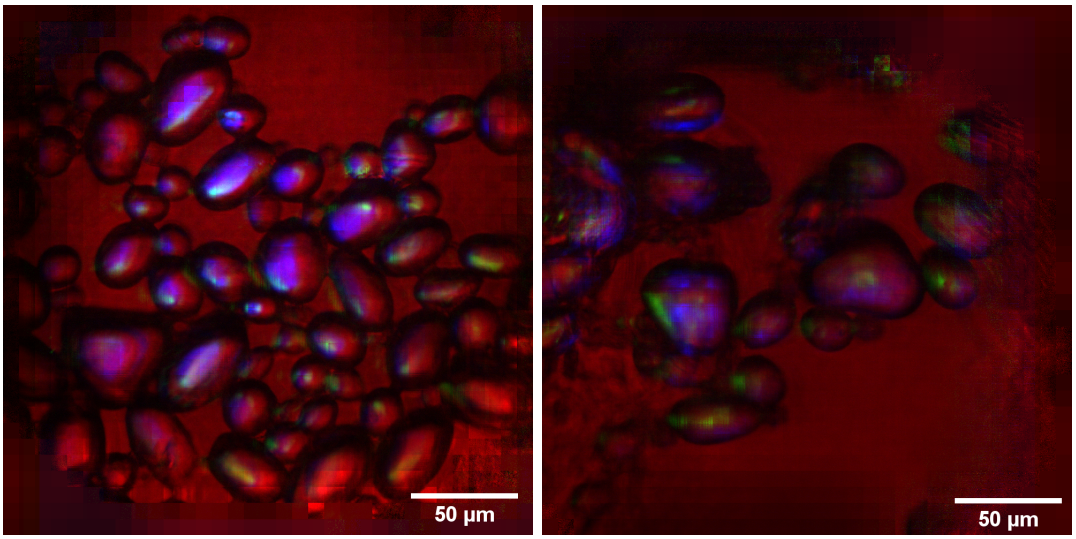

(a) **(b)**

Figure 6.6: Starch granules imaged with Stokes transmission (red), SHG (green) and CARS at 2850 cm^{-1} (blue). $\nu_f = 100$ Hz, $\tau_e = 9$ ms, $g_c = 20$ dB, $N_g = 30$, $S_{int} = 10$. Pump 800 nm, 48 mW. Stokes 18 mW Highest pixel value for transmission and CARS images ranges from 0 to 280 pe.Value for SHG ranges from 0 to 180 pe.

6.6 Conclusions

Different from previous multifocal approaches [92, 94], the camera is used only to seperate the signals of the different foci, not for direct imaging. This keeps the insensitivity to sample scattering afforded by the non-linear excitation point-spread function created by longer wavelength light which is the hallmark of point-scanning CRS. Additionally when compared to speckle wide-field CARS[26, 28] the intrinsic speckle noise is avoided. The speed of the technique in the presented setup is mainly limited by the camera readout, while the laser source caters for up to ten times higher excitation powers, and correspondingly 1000 times higher CARS powers, allowing to increase the speed accordingly, up to 100 frames per second.

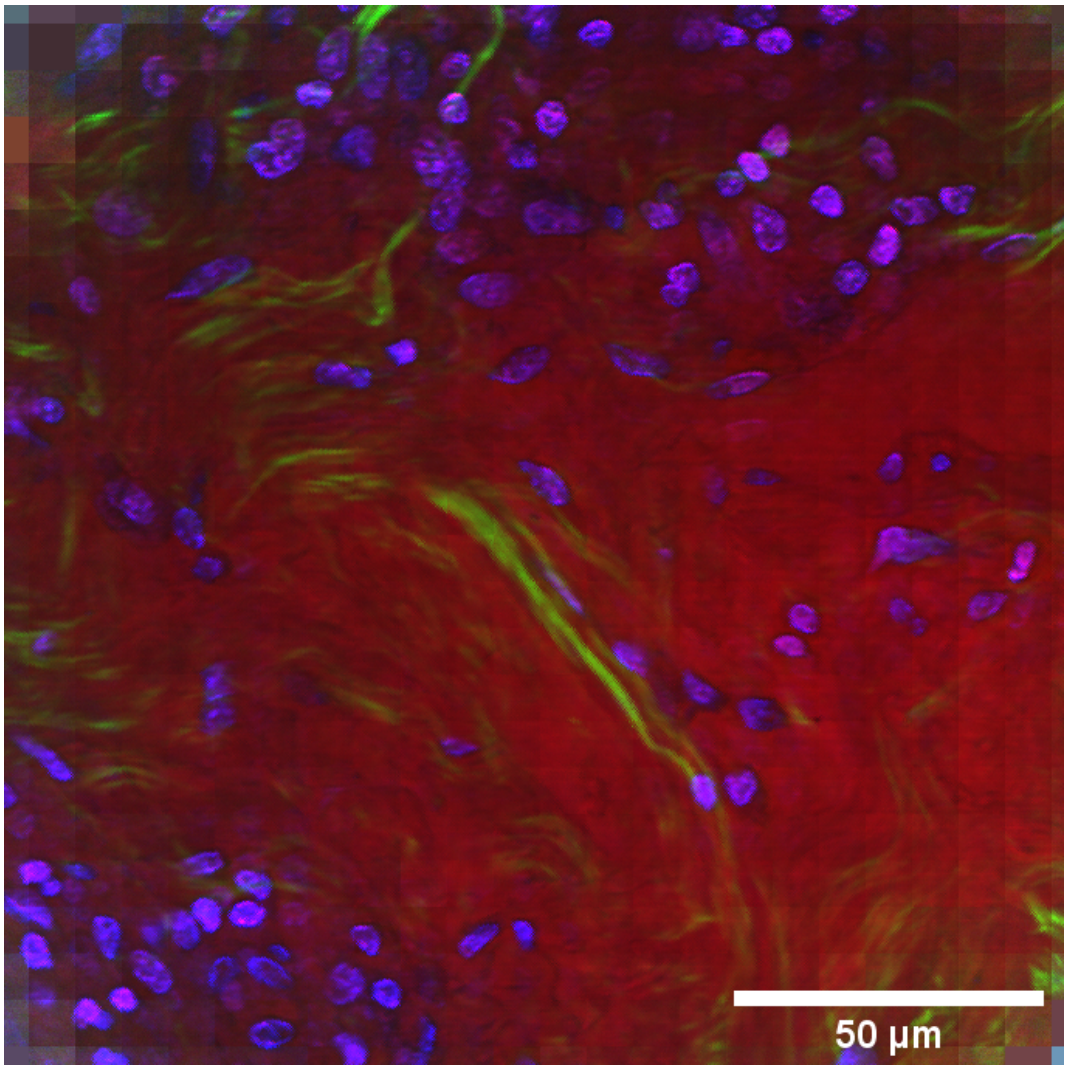

Figure 6.7: CARS and SHG imaging of human skin tissue. $\nu_\mathrm{f} = 200\,\mathrm{Hz}$, $\tau_\mathrm{e} = 4\,\mathrm{ms}$, $g_\mathrm{c} = 20\,\mathrm{dB}$, $N_\mathrm{g} = 30$, $S_\mathrm{int} = 10$. Pump 785 nm 20 mW, Stokes 50 mW. Flat field ($v = 1/5$) and tiling correction. Blue color shows protein and nucleic acids CARS resonance at $2970\,\mathrm{cm}^{-1}$ red shows non-resonant CARS signal at $2935\,\mathrm{cm}^{-1}$, and green the SHG signal. Value ranges are 0 to 8294 pe for the red, 0 to 4608 pe for the green, and 0 to 3686 pe for the blue channel.

Chapter 7

Summary and Outlook

CARS and SRS microscopy combined with SHG/THG is a powerful label-free imaging method which was demonstrated in this thesis with various experimental setups. CRONUS-2P OPO with two independently tunable channels was compared with a classical Ti:Sa system in terms of noise parameters and the ability to perform SRS imaging. It was concluded that both systems are shot-noise limited at 2.5 MHz modulation frequency when sampled at 0.1 ms and detected at 820 nm. SRS and CARS imaging was demonstrated with fixed Calu-3 cells by targeting lipid region.

The the two independently tunable channels with one fixed wavelength channel of CRONUS-2P allows to target three vibrational regions of a cell (fingerprint, cell silent, lipid) with high spectral resolution achieved by applying a spectral focusing scheme. Simultaneous imaging was demonstrated by adapting the setup at Light Conversion from SHG/THG imaging to two-channel (cell silent and lipid region) CARS imaging. Artifact-free imaging was demonstrated using flowing PS and PMMA beads in water where two different wavenumbers were detected with 0.5 s frame time and allowed to spectrally separate PS from PMMA. Additionally, a water, deuterated water and oil mixture was imaged in two different spectral regions, and taking two simultaneous images of the sample allowed to identify the three different materials imaged. The imaging modality was further demonstrated by imaging deuterated HeLa cells simultaneously in the cell silent and lipid regions which showed that the system is sensitive enough to detect deuterated lipids inside a human cell. Additionally, the high power output of CRONUS-2P allows to frequency double the beams and perform pre-resonant SRS experiments which uses light of shorther wavelength close to electronic transitions of fluorescent proteins [75]. Exiting closer to the electronic excitation, allowed to increase the SRS speed by a factor of 20 and achieve chromophore sensitivities as low as 1µM when compared to conventional SRS.

Another approach to potentially increase imaging speed was demonstrated by using random speckle illumination CARS which allows optical sectioning capability, higher spatial resolution than conventional bright-field imaging and is a robust method [28]. It was reported that the axial and lateral resolution was 3 µm and 0.3 µm respectively with real-time imaging capability. As an alternative for the random illumination method, a multi focal approach was presented which uses 33×33 focal point grid instead of the single focal point of a classical raster-scanning method. The biggest advantage is the excitation imaging as in raster-scanning method. The performance of the method was demonstrated by imaging PS and PMMA beads, and human skin tissue sample. The imaging speed was limited by the camera readout

speed which was 200 Hz.

The speed of multifocal CARS technique in the presented setup is mainly limited by the camera readout, while the laser source caters for up to ten times higher excitation powers, and correspondingly 1000 times higher CARS powers, allowing to increase the speed accordingly, up to 10^5 frames per second. This provides a 100 Hz frame rate for megapixel CARS images, corresponding to 10 ns pixel rate, about an order of magnitude faster than the fastest present single point scanning systems. Notably, due to the 1000 foci, this is achievable with similar single focus power densities using a 100 times lower repetition rate than single point systems. Since the camera only has to separate the different foci rather than imaging the sample at the Nyquist limit, the pixel number required is limited, and 100×100 pixels would suffice for 1000 foci, which can be read by present camera technology at up to 10^6 frames per second, opening the perspective to megapixel CARS imaging with 1000 Hz frame rates. In the future, the multifocal approach could be improved by adding glass blocks just after the lenslet array so that every individual beamlet would arrive at different times at the camera. This would reduce the cross-talk between different channels and could lead to the final image with less artifacts. Also, this could be used to apply different amount of linear chirp to each beamlet and address different IFDs of the sample by using galvo-mirrors. Another method to reduce image artifacts could be implemented in the reconstruction algorithm. Instead of hard-coding foci peak locations, an adaptive algorithm, which re-calculates foci peak locations at each frame, could be used. In that case, distance between focal points could vary, which is the case of heavly-scattering sample, and would be captured by the algorithm.

In general, current dominating method for CARS microscopy is the raster-scan method due to high-speed imaging, z sectioning, high spatial resolution capabilities and due to wide-selection of OPOs with nJ pulse energy. With highly increasing availability of high-power laser sources and OPAs it is expected that non-linear wide-field microscopy methods are going to be more popular in the future.

Appendices

Appendix A

Dual CARS supplement

Optics box layout

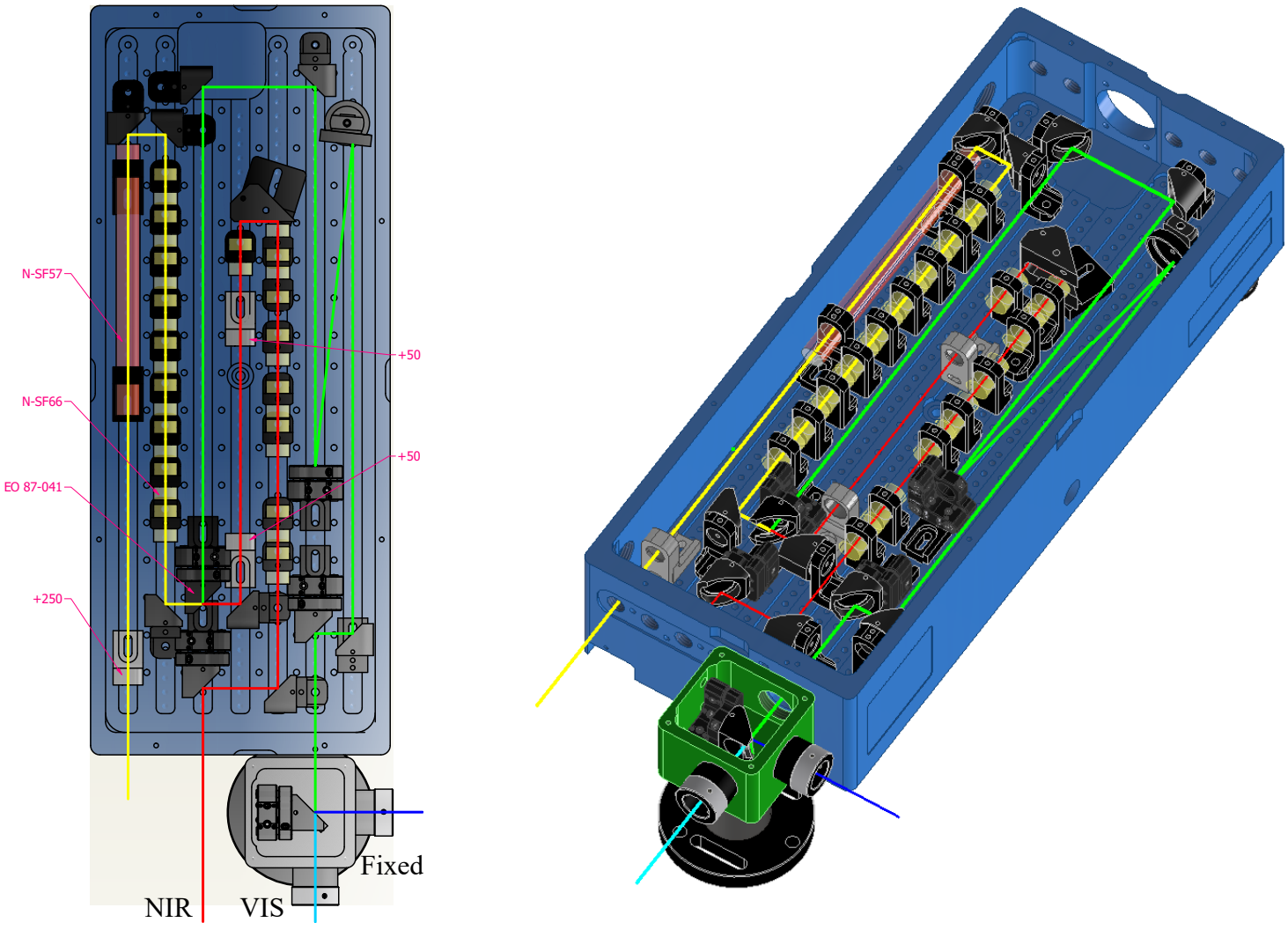

Figure A.1: a) Detailed layout of optics box. b) 3D view of optics box.

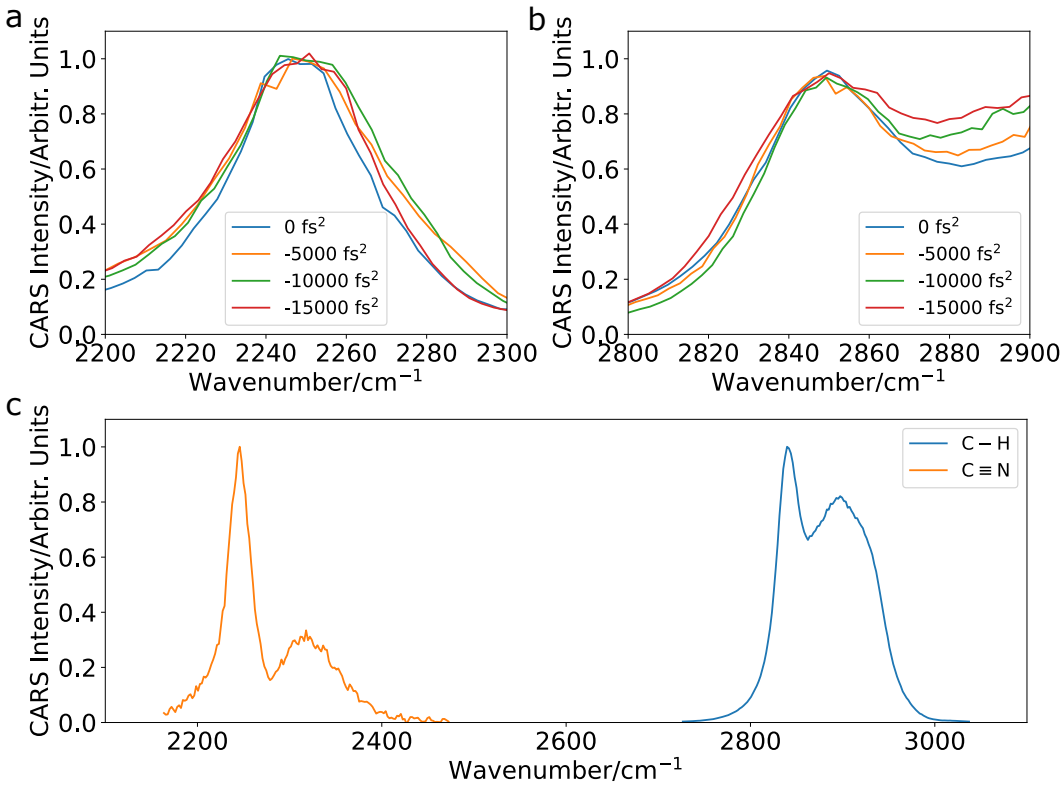

Figure A.2: Spectral focusing chirp matching and calibration. CARS intensity versus delay calibrated as IFD using the pump at 831 nm and different GDD settings of the CRONUS-2P as indicated. (a) cell-silent region (PMT 1) on 4-Nitrophenylacetonitrile with a peak at 2251 cm^{-1}using the fixed Stokes at 1025 nm and 2 mW of pump and Stokes at the sample. (b) C-H region (PMT 2) on oil with a peak at 2850 cm^{-1}using the variable Stokes at 1100 nm and 10 mW of pump and Stokes at the sample. (c) CARS on calibration samples as in (a) and (b) at zero GDD of the CRONUS-2P over the full spectral range.

Appendix B

Multifocal CARS supplement

Correction algorithm example

The correction algorithm minimizes scalar functions of multiple variables by using BFGS algorithm. The algorithm performance is presented in Figure B.1.

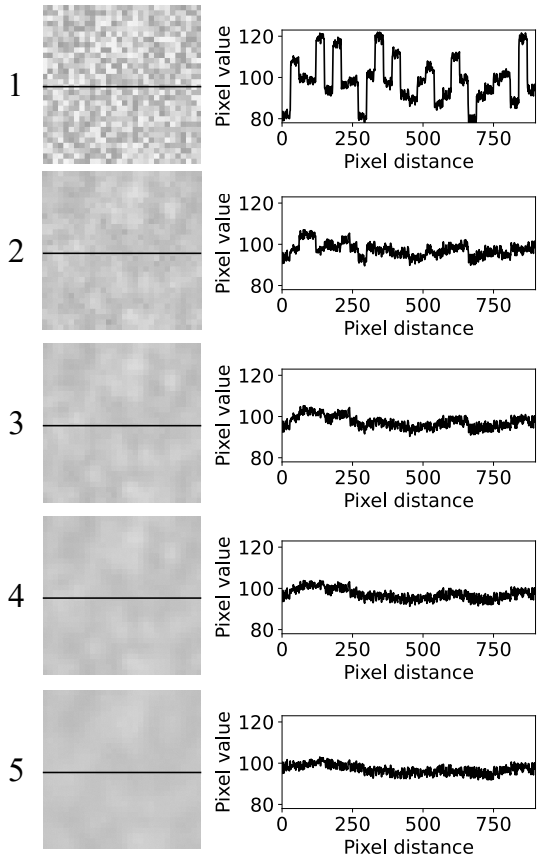

Figure B.1: Correction algorithm working principle. Artificially generated tiles with $N_g = 30$ and random ground value taken from a discrete distribution varying from 80 to 230. Each tile contains 30×30 pixels with values taken from a discrete distribution varying from -3 to 3 around the tile value. Left column shows increasing number of algorithm iterations with greyscale value ranging from 0 to 125. Right column shows corresponding pixel values along the black line.

Additional CARS and SHG results

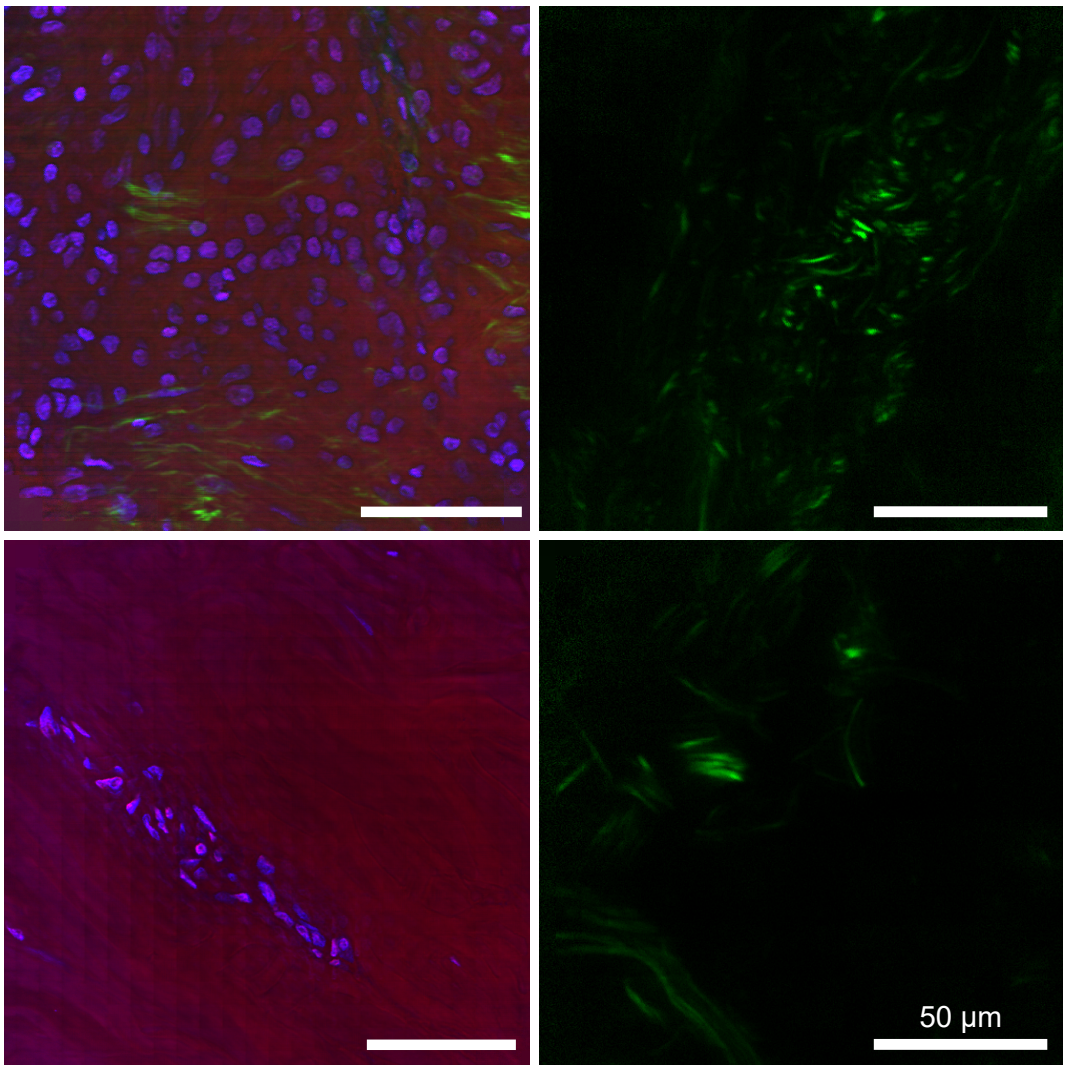

Figure B.2: Results obtained by using multifocal microscopy. Left column show CARS/SHG imaging of human skin sample, right column shows purely SHG imaging of human skin sample together with PS and PMMA bead imaging. $\nu_\mathrm{f} = 200\,\mathrm{Hz}$, $\tau_\mathrm{e} = 4\,\mathrm{ms}$, $g_\mathrm{c} = 20\,\mathrm{dB}$, $N_\mathrm{g} = 30$, $S_\mathrm{int} = 10$. Pump 785 nm 20 mW, Stokes 50 mW. Flat field ($v = 1/5$) and tiling correction. Left column CARS images: blue color shows CARS at $2970\,\mathrm{cm}^{-1}$ red shows CARS at $2935\,\mathrm{cm}^{-1}$, and green the SHG signal. Value ranges are 0 to 8294 pe for the red, 0 to 4608 pe for the green, and 0 to 3686 pe for the blue channel. Right column SHG images: same imaging parameters, value ranges are 0 to 3211 pe.

Comparison between excitation and detection imaging

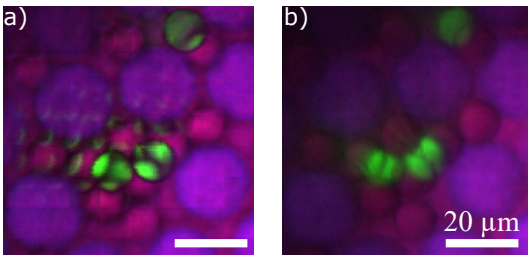

Figure B.3: Comparison between excitation imaging a) and detection b). Imaging parameters are described in Figure 6.5. Direct imaging red, green and blue channel range from 0 to 219 pe, 146 pe and 437 pe respectively.

Excitation imaging dependence on detection area size

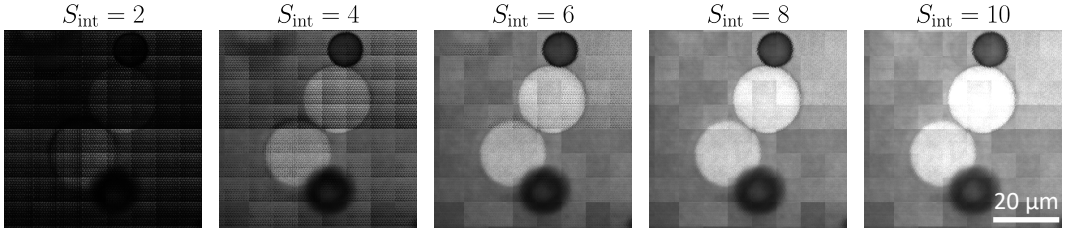

Figure B.4: CARS excitation imaging of sample B at 2950 cm^{-1} with $\nu_{\mathrm{f}} = 195\,\mathrm{Hz}$, $\tau_{\mathrm{e}} = 4\,\mathrm{ms}$, $g_{\mathrm{c}} = 10\,\mathrm{dB}$, $N_{\mathrm{g}} = 30$ using different values of S_{int} to reconstruct the final image as labeled. Black stripes appear with low S_{int} number as the averaging area is failing to capture the signal completely. Greyscale ranges from 0 to 2186 pe, 19728 pe, 35072 pe and 54800 pe for S_{int}values of 2, 4, 6, 8 and 10 respectively.

Sample scattering

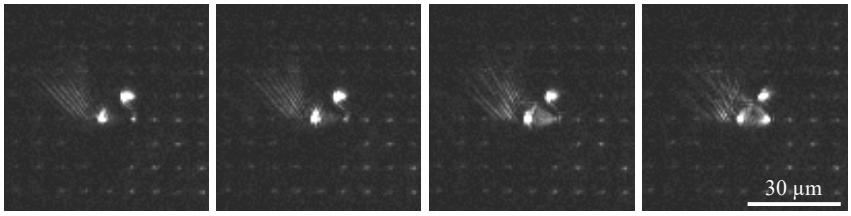

Figure B.5: Selected frames P_{kl} of CARS imaging of sample B (data from Figure 6.5a1) containing 20 µm PMMA and 10 µm PS beads showing strong signal scattering for some foci. From left to right (k, l) is $(1, 6)$, $(1, 29)$, $(3, 26)$, and $(4, 2)$. Greyscale 0 to 437 pe, g_{c}=10 dB, $\tau_{\mathrm{e}} = 5\,\mathrm{ms}$, $\nu_{\mathrm{f}} = 100\,\mathrm{Hz}$, $N_{\mathrm{g}} = 30$. Pump 785 nm, 20 mW, Stokes 50 mW, addressing PS resonance at 3050 cm^{-1}.

Multifocal CARS excitation and detection layout

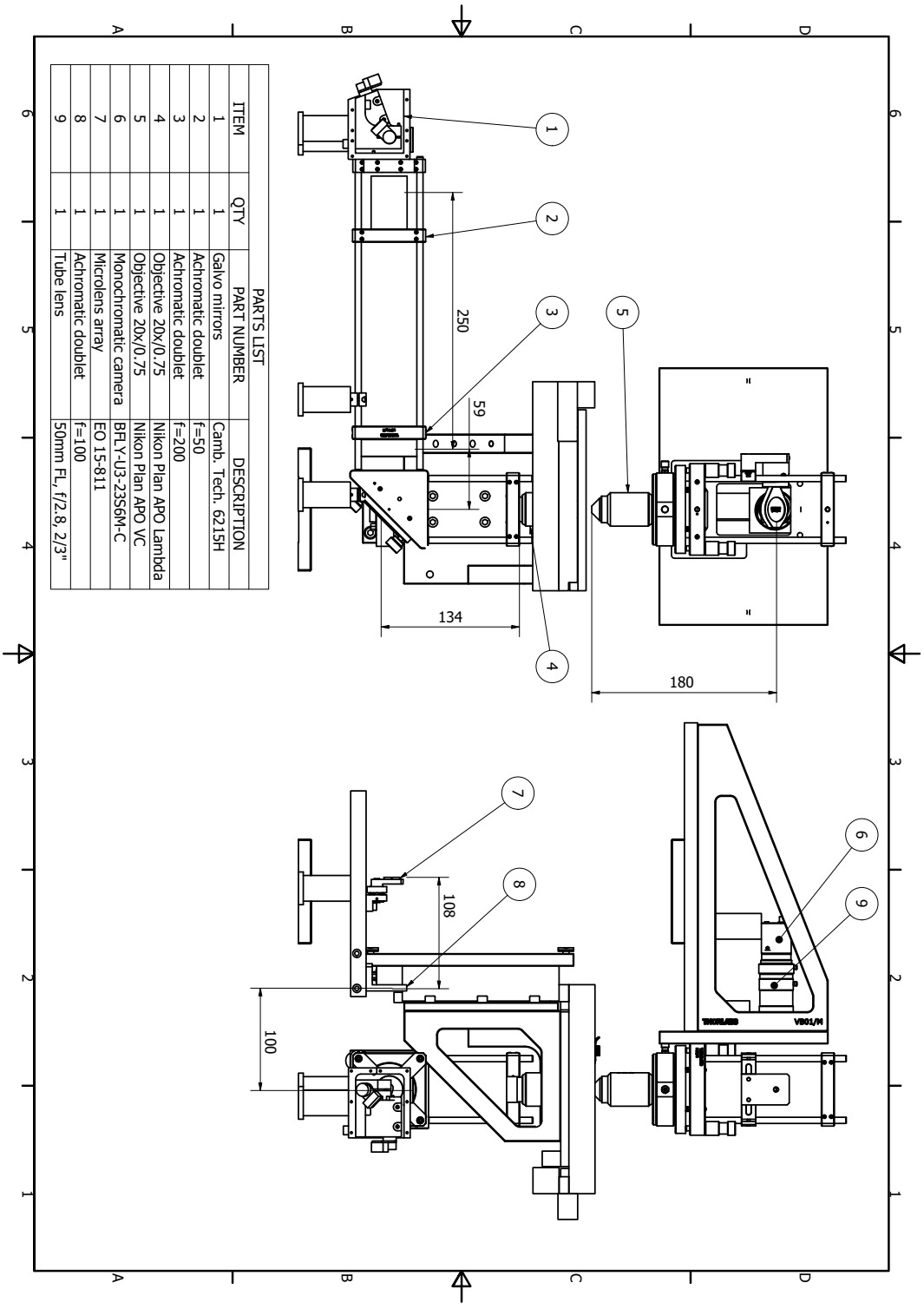

Figure B.6: Multifocal CARS excitation and detection layout.

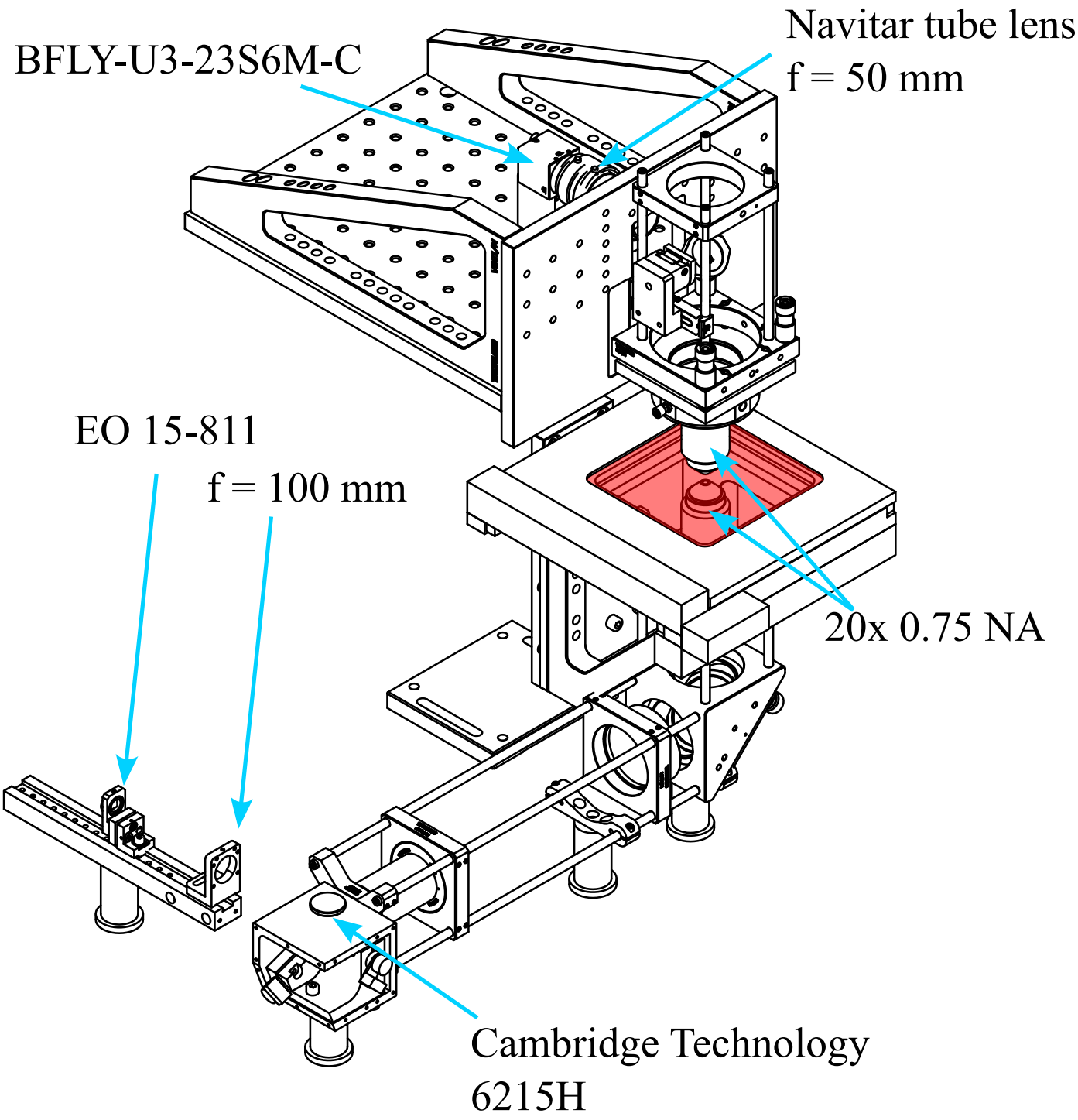

Figure B.7: Multifocal CARS excitation and detection layout in side view. Red area indicates sample plane.

Image reconstruction algorithm

```
1 from PIL import Image
2 import numpy as np
```

```
3  from skimage.feature import peak_local_max
4  from skimage import img_as_float
5  import matplotlib.pyplot as plt
6  import time
7  import math
8
9
10 def get_peaks(fname: str, loc: str, coordinate='x') -> np.ndarray:
11     """
12     This function takes the location of the calibration image
13     and returns foci locations. It also saves the images with
14     marked centre positions.
15     """
16     with Image.open("{}\{}".format(loc, fname)) as img:
17         peaks = peak_local_max(img_as_float(img), min_distance=7,
18                     threshold_rel=0.05)
19         for peak in peaks:
20             img.putpixel((peak[1], peak[0]), 0)
21
22         img.save(r'{}/saves/test_{}.bmp'.format(loc, coordinate))
23
24     if coordinate == 'x':
25         return np.sort(peaks[:,1])
26     elif coordinate =='y':
27         return np.sort(peaks[:,0])
28     else:
29         print("Unknown coordinate: {}".format(coordinate))
30
31
32 def fit_peaks(peak_loc: np.ndarray, xlabel=r'unknown') -> np.ndarray:
33     """
34     This funcion takes peak location array, performs polynomial fit
35     and returns polynomial coefficients in an array form. There is a
36     possibility to display the fit with matplotlib.
37     """
38     peak_num = np.linspace(0, len(peak_loc)-1, len(peak_loc))
39     poly = np.polyfit(peak_num, peak_loc, deg=2)
40
41     plt.scatter(peak_num, peak_loc, label='raw data')
42     plt.plot(np.polyval(poly, peak_num), 'red', label='polynomial fit')
43     plt.xlabel("peak number, [#]")
44     plt.ylabel(r"{} axis coordinates, [px]".format(xlabel))
45     print("polynomial coefficients for {} axis: {}".format(xlabel, poly))
46     return poly
47
48
49 def generate_peaks(x_poly: np.ndarray, y_poly: np.ndarray,
50                    peak_seed=[133,56], peak_dim=[15,15]) -> np.ndarray:
51     """
52     Generates and returns peak array with dimensions provided
53     by peak_dim list and polynomial fit coefficients. It also
```

```
    provides peak colum and row locations.
    """
    peaks = []
    for row in range(0, peak_dim[1]):
        for column in range(0, peak_dim[0]):
            peaks.append([(peak_seed[0] + int(column**2*x_poly[0]
                                             + column*x_poly[1]),
                           peak_seed[1] + int(row**2*y_poly[0]
                                              + row*y_poly[1])), (column, row)])
    return np.array(peaks)


def find_average(img: Image.Image, peaks: np.ndarray,
                 window_size=[10,10]) -> list:
    """
    Finds an average pixel value in the image with defined
    centre location and window size. peaks variable stores
    centre location while the window_size variable stores the average.
    """
    avg_list = []
    for peak in peaks:
        pix_num = 0
        sum_val = 0
        for i in range(0, 2*window_size[0]):
            for j in range(0, 2*window_size[1]):
                sum_val += img.getpixel((peak[0][0]+window_size[0]-i,
                                         peak[0][1]+window_size[1]-j))
                pix_num += 1
        avg_list.append(sum_val / pix_num)
    img.close()
    return [peaks, np.array(avg_list)]


def cycle_corrector(cycle: int, tile_size: list,
                    spc_x:int = 1, spc_z:int = 1) -> list:
    """
    Defining the raster scan pattern which is followed by the algorithm with
    the possibility to change set size.
    """

    jump_frame = [i for i in range(tile_size, tile_size**2, tile_size)]
    cycle += 1

    if cycle in jump_frame:
        return [0, 1*spc_z]

    ratio = math.floor(cycle / tile_size)
    if ratio % 2 == 0:
        return [-1*spc_x, 0]
    else:
        return [1*spc_x, 0]
```

```
105
106 def draw_rectangles(loc: str, img: Image.Image, peaks: np.ndarray,
107                      cycle: int, window_size=[10,10]) -> None:
108     """
109     Draws a rectangle defined by window_size around the peak location.
110     Used for debuging purposes, when you need to make sure that you are
111     calculating the average in the right area.
112     """
113     for peak in peaks:
114         for i in range(0, 2*window_size[0]):
115             for j in range(0, 2*window_size[1]):
116                 img.putpixel((peak[0][0]+window_size[0]-i,
117                               peak[0][1]+window_size[1]-j), 0)
118     img.save(r"{}\debug\test_{}.bmp".format(loc, cycle))
119
120 def populate_image(img: Image.Image, img_created: Image.Image,
121                    peak_pos: np.ndarray, peak_data_sc: np.ndarray) -> None:
122     """
123     Placing calculated average value into the corresponding pixel of the
124     final image.
125     """
126     peak_data = find_average(img, peak_pos, window_size=[5,5])
127     for x, y, avg in zip(peak_data_sc[:, 0], peak_data_sc[:, 1], peak_data[1]):
128         img_created.putpixel((x, y), avg)
129
130
131 def main_loop(PATH: str, peak_pos: np.ndarray, no_of_images: int,
132               number_of_peaks:int, tile_size: int, peak_data_sc: np.ndarray,
133               spc_x: float, spc_y: float, x_poly: np.ndarray,
134               y_poly: np.ndarray, x_seed: int, y_seed: int) -> None:
135     """
136     The main loop of the algorithm
137     """
138     img_created = Image.new("F", (number_of_peaks*tile_size,
139                                   number_of_peaks*tile_size))
140     for cycle in range(0, no_of_images):
141         print("Image number: {}".format(cycle))
142         try:
143             with Image.open(r"{}\{}.bmp".format(PATH, cycle)) as img:
144                 populate_image(img, img_created, peak_pos, peak_data_sc)
145         except Exception as e:
146             print(e)
147             break
148
149         x_seed += cycle_corrector(cycle, tile_size, spc_x, spc_y)[0]
150         y_seed += cycle_corrector(cycle, tile_size, spc_x, spc_y)[1]
151         peak_data_sc[:,0] += cycle_corrector(cycle, tile_size)[0]
152         peak_data_sc[:,1] += cycle_corrector(cycle, tile_size)[1]
153
154         peak_pos = generate_peaks(
155             x_poly, y_poly,
```

```
156             peak_seed=[math.floor(x_seed),
157                        math.floor(y_seed)], peak_dim=[33,33])
158     img_created.save(r"{}\final.tif".format(PATH))
159
160 def debug_loop(PATH, peak_pos, no_of_images, tile_size,
161                peak_data_sc, spc_x, spc_y, x_poly, y_poly,
162                x_seed, y_seed):
163     for cycle in range(0, no_of_images):
164         print("Image number: {}".format(cycle))
165         try:
166             with Image.open(r"{}\{}.bmp".format(PATH, cycle)) as img:
167                 draw_rectangles(PATH, img, peak_pos, cycle, window_size=[2,2])
168         except Exception as e:
169             print(e)
170             continue
171
172         x_seed += cycle_corrector(cycle, tile_size, spc_x, spc_y)[0]
173         y_seed += cycle_corrector(cycle, tile_size, spc_x, spc_y)[1]
174
175         peak_data_sc[:,0] += cycle_corrector(cycle, tile_size)[0]
176         peak_data_sc[:,1] += cycle_corrector(cycle, tile_size)[1]
177
178         peak_pos = generate_peaks(
179             x_poly, y_poly,
180             peak_seed=[math.floor(x_seed),
181                        math.floor(y_seed)], peak_dim=[33,33])
182
183 def main():
184     # Starting the timer
185     start_time = time.time()
186
187     # Path to the folder with raw and calibration images
188     PATH=r"PATH_TO_FOLDER\\"
189     # spc_x and spc_y are 0.35 for 30x30 and 0.40 for 25x25
190     spc_x = 0.35
191     spc_y = 0.35
192
193     # Providing initial x and y coordinates obtained from debug mode
194     # If in debg mode, making the initial guess
195     x_seed = 11
196     y_seed = 25
197
198     tile_size = 30
199     number_of_peaks = 33
200
201     no_of_images = 900
202     debug = True
203
204     # Obtaining peaks in the calibration image. Performing curve fitting.
205     peaks_x = get_peaks(r'x_calib.Bmp', PATH, coordinate='x')
206     peaks_y = get_peaks(r'y_calib.Bmp', PATH, coordinate='y')
```

```
207
208     x_poly = fit_peaks(peaks_x, 'x')
209     y_poly = fit_peaks(peaks_y, 'y')
210
211     # Generate peak location for the very first frame
212     peak_pos = generate_peaks(x_poly, y_poly,
213                               peak_seed=[x_seed, y_seed],
214                               peak_dim=[33,33])
215
216     # Perform pixel scaling for the final image.
217     # peak on the first row and first column must go
218     # to a certain coordinate on the final image.
219     peak_data_sc = tile_size*peak_pos[:,1,:]
220
221     peak_data_sc[:, 0] += tile_size - 1
222     if not debug:
223         try:
224             main_loop(PATH, peak_pos, no_of_images, number_of_peaks,
225                       tile_size, peak_data_sc, spc_x, spc_y, x_poly,
226                       y_poly, x_seed, y_seed)
227         except Exception as e:
228             print(e)
229     else:
230         try:
231             debug_loop(PATH, peak_pos, no_of_images, tile_size,
232                       peak_data_sc, spc_x, spc_y, x_poly, y_poly,
233                       x_seed, y_seed)
234         except Exception as e:
235             print(e)
236
237     end_time = time.time()
238     print("Execution time: {:.2f} s".format(end_time - start_time))
239
240 if __name__=="__main__":
241     main()
```

Tile correction algorithm

```
1
2  from PIL import Image
3  import time
4
5  def tile_average(x0: int, y0: int, tile_dim: list, img: Image.Image) -> float:
6      """Calculates average pixel value of each tile."""
7      val_sum = 0
8      val_pixels = 0
9
10     for y in range(y0, y0+tile_dim[1]):
11         for x in range(x0, x0+tile_dim[0]):
```

```
12              val_sum += img.getpixel((x, y))
13              val_pixels += 1
14      return val_sum / val_pixels
15
16  def image_average(path: str, fname:str) -> float:
17      """Calculates average pixel value of the whole image."""
18      with Image.open(path + fname) as img:
19          x_dim, y_dim = img.size
20          val_pixels = 0
21          val_sum = 0
22          for y in range(0, y_dim):
23              for x in range(0, x_dim):
24                  val_sum += img.getpixel((x, y))
25                  val_pixels += 1
26          return val_sum / val_pixels
27
28  def tile_calculation(path: str, fname: str, tile_dim: list) -> list:
29      """
30      Performs average pixel value calculations on the calibration image.
31      Outputs tile arbitrary numbering, tile start coordinates in pixels and
32      tile average pixel value
33      """
34      img_data = []
35
36      with Image.open(path + fname) as img:
37          x_lim, y_lim = img.size
38          no_tiles_x = int(x_lim / tile_dim[0])
39          no_tiles_y = int(y_lim / tile_dim[1])
40
41          x_start = [m*tile_dim[0] for m in range(0, no_tiles_x)]
42          y_start = [n*tile_dim[1] for n in range(0, no_tiles_y)]
43
44          for n, y0 in enumerate(y_start):
45              for m, x0 in enumerate(x_start):
46                  avg = tile_average(x0, y0, tile_dim, img)
47                  img_data.append([(m, n), (x0, y0), avg])
48          return img_data
49
50
51  def apply_corrections(img_calib: Image.Image, img_final: Image.Image,
52                        data: list, tile_dim: list, val_gavg: float):
53      pix_sum = 0
54      count = 0
55      ratio_limit = 5
56      correction_factor = val_gavg/data[2] if data[2] != 0.0 else 0
57
58      for y in range(data[1][1], data[1][1] + tile_dim[1]):
59          for x in range(data[1][0], data[1][0] + tile_dim[0]):
60              if abs(correction_factor) < ratio_limit:
61                  corrected_value = img_calib.getpixel((x, y)) * correction_factor
62                  img_final.putpixel((x, y), corrected_value)
```

```
                pix_sum += corrected_value
                count += 1
            else:
                img_final.putpixel((x, y), val_gavg)

def make_correction(path_sample: str, fname_sample: str, tile_dim: list,
                    tile_data: list, val_gavg) -> None:
    """ Performs corections on the sample image."""
    with (
        Image.open(path_sample + fname_sample) as img_calib,
        Image.new (mode="F", size=img_calib.size) as img_final,
    ):
        for data in tile_data:
            apply_corrections(img_calib, img_final, data, tile_dim, val_gavg)
        img_final.save(path_sample +"corrected.tif")

def main():
    tile_dim = [30, 30] # size of the tile

    # Path and file name of the calibration image
    path_calib = r'PATH_TO_CALIBRATION_IMG\\'
    fname_calib = r'Calibration.tif'

    # Calculates parameters from the calibration image.
    val_tile = tile_calculation(path_calib, fname_calib, tile_dim)
    val_norm = image_average(path_calib, fname_calib)

    # Path and file name of the sample image
    path_sample = r'PATH_TO_SAMPLE\\'
    fname_sample = r'Sample.tif'
    make_correction(path_sample, fname_sample, tile_dim, val_tile, val_norm)

if __name__=="__main__":
    start_time = time.time()
    main()
    end_time = time.time()
    print("Time taken: {:.2f} s".format(end_time - start_time))
```

Image optimization algorithm

```

from PIL import Image
import numpy as np
from scipy import optimize
import math
import time

class TileImage():
    """
```

```
    TileImage class loads an image and provides functions to calculate required
    parameters for the optimization algorithm.
    """
    def __init__(self, PATH: str, fname: str, tile_dim: list) -> None:
        """
        Initializer to set the class variables
        """
        try:
            with Image.open(PATH + fname) as image:
                self.tiles_no = (int(image.width / tile_dim[0]),
                                 int(image.height / tile_dim[1]))
                self.fname = fname
                self.image = np.asanyarray(image)
                self.tile_dim = tile_dim
                self.PATH = PATH
        except Exception as e:
            print("Init problem!")
            print(e)

    def get_edge_sum(self, tile_no_x: int,
                     tile_no_y: int , edge_no: int) -> float:
        """
        This function returns edge sum of the selected tile and selected edge.
        Edge diagram:

            edge_0
          _________
         |         |
    _3 |  tile    | _1
         |         |
         |_________|
              _2
        """

        edges = {
            "edge_0": [],
            "edge_1": [],
            "edge_2": [],
            "edge_3": [],
        }

        if tile_no_x < 0 or tile_no_y < 0 or tile_no_x > self.tiles_no[0] \
                        or tile_no_y > self.tiles_no[1]:
            print("Bad tile dimensions!")
            return

        x_start = tile_no_x*self.tile_dim[0]
        y_start = tile_no_y*self.tile_dim[1]

        for row in range(y_start, y_start + self.tile_dim[1]):
            for column in range(x_start, x_start + self.tile_dim[0]):
```

```
61                  if row == y_start:
62                      edges["edge_0"].append(self.image[row, column])
63                  if column == x_start + self.tile_dim[0] - 1:
64                      edges["edge_1"].append(self.image[row, column])
65                  if row == y_start + self.tile_dim[1] - 1:
66                      edges["edge_2"].append(self.image[row, column])
67                  if column == x_start:
68                      edges["edge_3"].append(self.image[row, column])
69
70          if edge_no == 0:
71              return sum(edges["edge_0"]) / self.tile_dim[0]
72          elif edge_no == 1:
73              return sum(edges["edge_1"]) / self.tile_dim[1]
74          elif edge_no == 2:
75              return sum(edges["edge_2"]) / self.tile_dim[0]
76          elif edge_no == 3:
77              return sum(edges["edge_3"]) / self.tile_dim[1]
78
79      def get_edge_ratios(self, x: int, y: int, edge_no: int) -> float:
80          """
81          This function returns selected edge ratio of two selected
82          neighbouring tiles.
83          """
84
85          ratios = {
86              "ratio_0": 1,
87              "ratio_1": self.get_edge_sum(x, y, 1) / self.get_edge_sum(0, y, 3),
88              "ratio_2": self.get_edge_sum(x, y, 2) / self.get_edge_sum(x, 0, 0),
89              "ratio_3": 1,
90          }
91
92          if y - 1 >= 0:
93              ratios["ratio_0"] = self.get_edge_sum(x, y - 1, 2) \
94                                  / self.get_edge_sum(x, y, 0)
95          if x + 1 < self.tiles_no[0]:
96              ratios["ratio_1"] = self.get_edge_sum(x, y, 1) \
97                                  / self.get_edge_sum(x + 1, y, 3)
98          if y + 1 < self.tiles_no[1]:
99              ratios["ratio_2"] = self.get_edge_sum(x, y, 2) \
100                                 / self.get_edge_sum(x, y + 1, 0)
101         if x - 1 >= 0:
102             ratios["ratio_3"] = self.get_edge_sum(x - 1, y, 1) \
103                                 / self.get_edge_sum(x, y, 3)
104
105         if edge_no == 0:
106             return ratios["ratio_0"]
107         if edge_no == 1:
108             return ratios["ratio_1"]
109         if edge_no == 2:
110             return ratios["ratio_2"]
111         if edge_no == 3:
```

```
112             return ratios["ratio_3"]
113
114     def get_correction_factors(self, x:int , y: int, base: int=1):
115         """
116         Finds correction factors which are an inverse of edge ratios.
117         """
118         return np.divide(base, self.get_edge_ratios(x, y))
119
120     def correct_pixel(self, x_tile: int, y_tile:int,
121                       new_img: Image.Image, c: list) -> Image.Image:
122         """
123         Corrects each individual pixel with the correction factor and returns
124         a corrected image.
125         """
126         for y_pix in range(y_tile*self.tile_dim[1],
127                            y_tile*self.tile_dim[1] + self.tile_dim[1]):
128             for x_pix in range(x_tile*self.tile_dim[0],
129                                x_tile*self.tile_dim[0] + self.tile_dim[0]):
130
131                 new_img[y_pix, x_pix] = new_img[y_pix, x_pix] * \
132                                         c[y_tile, x_tile]
133         return new_img
134
135     def make_corection(self, c: list) -> None:
136         """
137         Corrects each tile with correction factor.
138         """
139         new_img = self.image.copy()
140         for y_tile in range(0, self.tiles_no[1]):
141             for x_tile in range(0, self.tiles_no[0]):
142                 final_img = self.correct_pixel(x_tile, y_tile, new_img, c)
143         Image.fromarray(final_img).save(self.PATH +
144                                         "optimized_{}".format(self.fname))
145
146 def test_function(c: list, ux:list, uy: list, timage: Image.Image) -> float:
147     """
148     Test function used to minimize the coefficients.
149     """
150     result = 0
151     for i, value in enumerate(ux):
152         if i < len(ux) and (i+1) < len(ux) and (i+1) % timage.tiles_no[0]!= 0:
153             result += value*(c[i] / c[i+1])
154         elif i < len(ux) and (i+1) % timage.tiles_no[0] == 0 :
155             result += value*(c[i] / c[i-timage.tiles_no[0]+1 ])
156
157     for i, value in enumerate(uy):
158         if i + timage.tiles_no[0] < len(uy) :
159             result += value * (c[i] / c[i+timage.tiles_no[0]])
160         elif i + timage.tiles_no[0] >= len(uy):
161              result += value*(c[i] / c[i-(timage.tiles_no[0]*timage.tiles_no[1]
162                                          - timage.tiles_no[1])])
```

```
163     return abs(math.log10(result)) + abs(math.log10(result))
164
165 def main():
166     PATH = r'PATH_TO_FOLDER\\'
167     fname = r'Image.tif'
168     tile_dim = [30, 30] # tile dimensions
169
170     timage = TileImage(PATH, fname, tile_dim)
171
172     print("Retrieving edge ratios")
173     ux = [timage.get_edge_ratios(x, y, 1) for y in range(0, timage.tiles_no[1])
174                                           for x in range(0, timage.tiles_no[0])]
175
176     uy = [timage.get_edge_ratios(x, y, 2) for y in range(0, timage.tiles_no[1])
177                                           for x in range(0, timage.tiles_no[0])]
178     print("Done")
179
180     # Initial guess
181     init_guess = 1*np.ones(int(timage.tiles_no[0]*timage.tiles_no[1]))
182
183     # Boundary conditions
184     bounds = [(0.5, 1.5) for _ in range(0, int(timage.tiles_no[0]
185                                                * timage.tiles_no[1]))]
186
187     print("Optimizing...")
188     A = optimize.minimize(test_function, init_guess, bounds=bounds,
189                           args=(ux, uy, timage))
190     print("Done")
191     coefs = np.array(A.x)
192     coefs = coefs.reshape(timage.tiles_no[0], timage.tiles_no[1])
193     timage.make_corection(coefs)
194
195 if __name__=="__main__":
196     start_time = time.time()
197     main()
198     end_time = time.time()
199     print("Time taken: {:.2f} s".format(end_time - start_time))
200
```

Bibliography

[1] X. Audier, S. Heuke, P. Volz, I. Rimke, and H. Rigneault. Noise in stimulated Raman scattering measurement: From basics to practice. *APL Photonics*, 5(1):011101, 2020.

[2] Christian W Freudiger, Wenlong Yang, Gary R Holtom, Nasser Peyghambarian, X Sunney Xie, and Khanh Q Kieu. Stimulated Raman scattering microscopy with a robust fibre laser source. *Nature photonics*, 8(2):153–159, 2014.

[3] Theodore George Rochow and Paul Arthur Tucker. *A Brief History of Microscopy*, pages 1–21. Springer US, Boston, MA, 1994.

[4] George Gabriel Stokes. XXX. on the change of refrangibility of light. *Philosophical transactions of the Royal Society of London*, (142):463–562, 1852.

[5] Kirti Prakash, Benedict Diederich, Rainer Heintzmann, and Lothar Schermelleh. Super-resolution microscopy: a brief history and new avenues. *Philosophical Transactions of the Royal Society A*, 380(2220).

[6] Daniel Schraivogel, Terra M. Kuhn, Benedikt Rauscher, Marta Rodríguez-Martínez, Malte Paulsen, Keegan Owsley, Aaron Middlebrook, Christian Tischer, Beáta Ramasz, Diana Ordoñez-Rueda, Martina Dees, Sara Cuylen-Haering, Eric Diebold, and Lars M. Steinmetz. High-speed fluorescence image-enabled cell sorting. *Science*, 375(6578):315–320, 2022.

[7] Francesco Acerbi, Morgan Broggi, Marica Eoli, Elena Anghileri, Lucia Cuppini, Bianca Pollo, Marco Schiariti, Sergio Visintini, Chiara Orsi, Angelo Franzini, et al. Fluorescein-guided surgery for grade iv gliomas with a dedicated filter on the surgical microscope: preliminary results in 12 cases. *Acta neurochirurgica*, 155:1277–1286, 2013.

[8] Nikita Lakomkin and Constantinos G. Hadjipanayis. Fluorescence-guided surgery for high-grade gliomas. *Journal of Surgical Oncology*, 118(2):356–361, 2018.

[9] Oanh Tu, Tim Knott, Michele Marsh, Kate Bechtol, Dennis Harris, David Barker, and John Bashkin. The influence of fluorescent dye structure on the electrophoretic mobility of end-labeled DNA. *Nucleic Acids Research*, 26(11):2797–2802, 06 1998.

[10] Nathan C. Shaner, George H. Patterson, and Michael W. Davidson. Advances in fluorescent protein technology. *Journal of Cell Science*, 120(24):4247–4260, 12 2007.

[11] Max Diem, Antonella Mazur, Kathleen Lenau, Jen Schubert, Ben Bird, Milo Miljković, Christoph Krafft, and Jürgen Popp. Molecular pathology via IR and Raman spectral imaging. *Journal of Biophotonics*, 6(11-12):855–886, 2013.

[12] Angela Walter, Wilm Schumacher, Thomas Bocklitz, Martin Reinicke, Petra Rösch, Erika Kothe, and Jürgen Popp. From bulk to single-cell classification of the filamentous growing streptomyces bacteria by means of Raman spectroscopy. *Appl. Spectrosc.*, 65(10):1116–1125, Oct 2011.

[13] Fanghao Hu, Chen Zeng, Rong Long, Yupeng Miao, Lu Wei, Qizhi Xu, and Wei Min. Supermultiplexed optical imaging and barcoding with engineered polyynes. *Nature methods*, 15(3):194–200, 2018.

[14] Dario Polli, Vikas Kumar, Carlo M. Valensise, Marco Marangoni, and Giulio Cerullo. Broadband coherent Raman scattering microscopy. *Laser & Photonics Reviews*, 12(9):1800020, 2018.

[15] Conor L. Evans, Eric O. Potma, Mehron Puoris'haag, Daniel Côté, Charles P. Lin, and X. Sunney Xie. Chemical imaging of tissue *in vivo* with video-rate coherent anti-Stokes Raman scattering microscopy. *Proceedings of the National Academy of Sciences*, 102(46):16807–16812, 2005.

[16] W Ruchira Silva, Christian T Graefe, and Renee R Frontiera. Toward label-free super-resolution microscopy. *Acs Photonics*, 3(1):79–86, 2016.

[17] Li Gong, Wei Zheng, Ying Ma, and Zhiwei Huang. Saturated stimulated-Raman-scattering microscopy for far-field superresolution vibrational imaging. *Phys. Rev. Appl.*, 11:034041, Mar 2019.

[18] Hongje Jang, Yajuan Li, Anthony A Fung, Pegah Bagheri, Khang Hoang, Dorota Skowronska-Krawczyk, Xiaoping Chen, Jane Y Wu, Bogdan Bintu, and Lingyan Shi. Super-resolution SRS microscopy with a-pod. *Nature methods*, 20(3):448–458, 2023.

[19] Delong Zhang, Ping Wang, Mikhail N Slipchenko, and Ji-Xin Cheng. Fast vibrational imaging of single cells and tissues by stimulated Raman scattering microscopy. *Accounts of chemical research*, 47(8):2282–2290, 2014.

[20] Marcus T. Cicerone, Khaled A. Aamer, Young Jong Lee, and Erik Vartiainen. Maximum entropy and time-domain Kramer-Krönig phase retrieval approaches are functionally equivalent for CARS microspectroscopy. *Journal of Raman Spectroscopy*, 43(5):637–643, 2012.

[21] Federico Vernuccio, Arianna Bresci, Benedetta Talone, Alejandro de la Cadena, Chiara Ceconello, Stefano Mantero, Cristina Sobacchi, Renzo Vanna, Giulio Cerullo, and Dario Polli. Fingerprint multiplex CARS at high speed based on supercontinuum generation in bulk media and deep learning spectral denoising. *Opt. Express*, 30(17):30135–30148, Aug 2022.

[22] Rola Houhou, Parijat Barman, Micheal Schmitt, Tobias Meyer, Jürgen Popp, and Thomas Bocklitz. Deep learning as phase retrieval tool for CARS spectra. *Opt. Express*, 28(14):21002–21024, Jul 2020.

[23] Sergey P. Laptenok Luca Genchi and Carlo Liberale. Background signals in stimulated Raman scattering microscopy and current solutions to avoid them. *Advances in Physics: X*, 8(1):2176258, 2023.

[24] Li Gong, Wei Zheng, Ying Ma, and Zhiwei Huang. Higher-order coherent anti-Stokes Raman scattering microscopy realizes label-free super-resolution vibrational imaging. *Nature Photonics*, 14(2):115–122, 2020.

[25] Christoph Heinrich, Stefan Bernet, and Monika Ritsch-Marte. Wide-field coherent anti-Stokes Raman scattering microscopy. *Applied Physics Letters*, 84(5):816–818, 02 2004.

[26] Christoph Heinrich, Alexander Hofer, Stefan Bernet, and Monika Ritsch-Marte. Coherent anti-Stokes Raman scattering microscopy with dynamic speckle illumination. *New J. Phys.*, 10(2):023029, February 2008.

[27] Cheng Zong, Ran Cheng, Fukai Chen, Peng Lin, Meng Zhang, Zhicong Chen, Chuan Li, Chen Yang, and Ji-Xin Cheng. Wide-field surface-enhanced coherent anti-Stokes Raman scattering microscopy. *ACS Photonics*, 9(3):1042–1049, 2022.

[28] Eric M Fantuzzi, Sandro Heuke, Simon Labouesse, Dominykas Gudavičius, Randy Bartels, Anne Sentenac, and Hervé Rigneault. Wide-field coherent anti-Stokes Raman scattering microscopy using random illuminations. *Nature Photonics*, pages 1–8, 2023.

[29] Max Diem. *Modern vibrational spectroscopy and micro-spectroscopy: theory, instrumentation and biomedical applications*. John Wiley & Sons, 2015.

[30] J. C. D. Brand. The discovery of the Raman effect. *Notes and Records of the Royal Society of London*, 43(1):1–23, 1989.

[31] Andreas Zumbusch, Wolfgang, and Paola Borri. Nonlinear vibrational microscopy applied to lipid biology. *Progress in Lipid Research*, 52(4):615–632, 2013.

[32] Ji-Xin Cheng and Xiaoliang Sunney Xie. *Coherent Raman scattering microscopy*. CRC press, 2016.

[33] Michiel Müller and Andreas Zumbusch. Coherent anti-Stokes Raman scattering microscopy. *ChemPhysChem*, 8(15):2156–2170, 2007.

[34] Sandro Heuke and Hervé Rigneault. Coherent Stokes Raman scattering microscopy (CSRS). *Nature Communications*, 14(1):3337, 2023.

[35] M. D. Duncan, J. Reintjes, and T. J. Manuccia. Scanning coherent anti-Stokes Raman microscope. *Opt. Lett.*, 7(8):350–352, Aug 1982.

[36] E.J. Liang, A. Weippert, J.-M. Funk, A. Materny, and W. Kiefer. Experimental observation of surface-enhanced coherent anti-Stokes Raman scattering. *Chemical Physics Letters*, 227(1):115–120, 1994.

[37] Li Li and Ji-Xin Cheng. Label-free coherent anti-Stokes Raman scattering imaging of coexisting lipid domains in single bilayers. *The Journal of Physical Chemistry B*, 112(6):1576–1579, 2008.

[38] E. Ploetz, S. Laimgruber, S. Berner, W. Zinth, and P. Gilch. Femtosecond stimulated Raman microscopy. *Applied Physics B*, 87(3):389–393, May 2007.

[39] Francesco Crisafi, Vikas Kumar, Tullio Scopigno, Marco Marangoni, Giulio Cerullo, and Dario Polli. In-line balanced detection stimulated Raman scattering microscopy. *Scientific reports*, 7(1):1–8, 2017.

[40] J. F. Ward and G. H. C. New. Optical third harmonic generation in gases by a focused laser beam. *Phys. Rev.*, 185:57–72, Sep 1969.

[41] Ji-Xin Cheng and X. Sunney Xie. Green's function formulation for third-harmonic generation microscopy. *J. Opt. Soc. Am. B*, 19(7):1604–1610, Jul 2002.

[42] Delphine Débarre, Willy Supatto, Ana-Maria Pena, Aurélie Fabre, Thierry Tordjmann, Laurent Combettes, Marie-Claire Schanne-Klein, and Emmanuel Beaurepaire. Imaging lipid bodies in cells and tissues using third-harmonic generation microscopy. *Nature methods*, 3(1):47–53, 2006.

[43] Isaac Freund, Moshe Deutsch, and Aaron Sprecher. Connective tissue polarity. optical second-harmonic microscopy, crossed-beam summation, and small-angle scattering in rat-tail tendon. *Biophysical journal*, 50(4):693–712, 1986.

[44] Oleg Nadiarnykh, Ronald B LaComb, Molly A Brewer, and Paul J Campagnola. Alterations of the extracellular matrix in ovarian cancer studied by second harmonic generation imaging microscopy. *BMC cancer*, 10:1–14, 2010.

[45] Thomas Abraham, Gloria Fong, and Alex Scott. Second harmonic generation analysis of early achilles tendinosis in response to in vivo mechanical loading. *BMC musculoskeletal disorders*, 12:1–6, 2011.

[46] Katja Schenke-Layland, Navid Madershahian, Iris Riemann, Barry Starcher, Karl-Jürgen Halbhuber, Karsten König, and Ulrich A Stock. Impact of cryopreservation on extracellular matrix structures of heart valve leaflets. *The Annals of thoracic surgery*, 81(3):918–926, 2006.

[47] Shih-Peng Tai, Wen-Jeng Lee, Dar-Bin Shieh, Ping-Ching Wu, Hsin-Yi Huang, Che-Hang Yu, and Chi-Kuang Sun. In vivo optical biopsy of hamster oral cavity with epi-third-harmonic-generation microscopy. *Optics express*, 14(13):6178–6187, 2006.

[48] Danielle Tokarz, Richard Cisek, Marc N Wein, Raphaël Turcotte, Christa Haase, Shu-Chi A Yeh, Srinidhi Bharadwaj, Anthony P Raphael, Hari Paudel, Clemens Alt, et al. Intravital imaging of osteocytes in mouse calvaria using third harmonic generation microscopy. *PloS one*, 12(10):e0186846, 2017.

[49] Emilio J Gualda, George Filippidis, G Voglis, M Mari, C Fotakis, and N Tavernarakis. In vivo imaging of cellular structures in caenorhabditis elegans by combined tpef, shg and thg microscopy. *Journal of Microscopy*, 229(1):141–150, 2008.

[50] Hervé Rigneault and Pascal Berto. Tutorial: Coherent Raman light matter interaction processes. *APL Photonics*, 3(9):091101, 2018.

[51] G Jancsó and P Bopp. The dependence of the internal vibrational frequencies of liquid water on central force potentials. *Zeitschrift für Naturforschung A*, 38(2):206–213, 1983.

[52] Theodore H Maiman, RH Hoskins, I Ji D'Haenens, Charles K Asawa, and V Evtuhov. Stimulated optical emission in fluorescent solids. ii. spectroscopy and stimulated emission in ruby. *Physical Review*, 123(4):1151, 1961.

[53] F. J. McClung and R. W. Hellwarth. Giant optical pulsations from ruby. *Appl. Opt.*, 1(S1):103–105, Jan 1962.

[54] LE Hargrove, Richard L Fork, and MA Pollack. Locking of He–Ne laser modes induced by synchronous intracavity modulation. *Applied Physics Letters*, 5(1):4–5, 1964.

[55] T. Norris, T. Sizer, and G. Mourou. Generation of 90 fs pulses with a cpm laser pumped by a frequency-doubled CW mode-locked Nd:YAG. In *Topical Meeting on Ultrafast Phenomena*, page PD5. Optica Publishing Group, 1984.

[56] Donna Strickland and Gerard Mourou. Compression of amplified chirped optical pulses. *Optics Communications*, 55(6):447–449, 1985.

[57] P. A. Franken, A. E. Hill, C. W. Peters, and G. Weinreich. Generation of optical harmonics. *Phys. Rev. Lett.*, 7:118–119, Aug 1961.

[58] J. A. Giordmaine and Robert C. Miller. Tunable coherent parametric oscillation in $LiNbO_3$ at optical frequencies. *Phys. Rev. Lett.*, 14:973–976, Jun 1965.

[59] Israel Rocha-Mendoza, Wolfgang Langbein, and Paola Borri. Coherent anti-Stokes Raman microspectroscopy using spectral focusing with glass dispersion. *Applied Physics Letters*, 93(20), 2008.

[60] Wolfgang Langbein, Israel Rocha-Mendoza, and Paola Borri. Coherent anti-Stokes Raman micro-spectroscopy using spectral focusing: Theory and experiment. *J. Raman Spectrosc.*, 40:800–808, 2009.

[61] Jean-Claude Diels and Wolfgang Rudolph. *Ultrashort laser pulse phenomena*. Elsevier, 2006.

[62] R.P. Scott, C. Langrock, and B.H. Kolner. High-dynamic-range laser amplitude and phase noise measurement techniques. *IEEE Journal of Selected Topics in Quantum Electronics*, 7(4):641–655, 2001.

[63] Bahaa EA Saleh and Malvin Carl Teich. *Fundamentals of photonics*. john Wiley & sons, 2019.

[64] Rongqing Hui. Chapter 4 - photodetectors. In Rongqing Hui, editor, *Introduction to Fiber-Optic Communications*, pages 125–154. Academic Press, 2020.

[65] T. P. Purdy, P.-L. Yu, R. W. Peterson, N. S. Kampel, and C. A. Regal. Strong optomechanical squeezing of light. *Phys. Rev. X*, 3:031012, Sep 2013.

[66] Richard C Prince, Renee R Frontiera, and Eric O Potma. Stimulated Raman scattering: from bulk to nano. *Chemical reviews*, 117(7):5070–5094, 2017.

[67] Chun-Rui Hu, Mikhail N. Slipchenko, Ping Wang, Pu Wang, Jiandie D. Lin, Garth Simpson, Bing Hu, and Ji-Xin Cheng. Stimulated Raman scattering imaging by continuous-wave laser excitation. *Opt. Lett.*, 38(9):1479–1481, May 2013.

[68] X Shan and DM Spirit. Novel method to suppress noise in harmonically modelocked erbium fibre lasers. *Electronics Letters*, 29(11):979–981, 1993.

[69] Wolfgang Langbein, David Regan, Iestyn Pope, and Paola Borri. Invited article: Heterodyne dual-polarization epi-detected CARS microscopy for chemical and topographic imaging of interfaces. *APL Photonics*, 3(9):092402, 2018.

[70] P. Fimpel, C. Riek, L. Ebner, A. Leitenstorfer, D. Brida, and A. Zumbusch. Boxcar detection for high-frequency modulation in stimulated Raman scattering microscopy. *Applied Physics Letters*, 112(16):161101, 2018.

[71] Israel Rocha-Mendoza, Wolfgang Langbein, Peter Watson, and Paola Borri. Differential coherent anti-Stokes Raman scattering microscopy with linearly-chirped femtosecond laser pulses. *Opt. Lett.*, 34:2258–2260, 2009.

[72] Thomas Hellerer, Annika MK Enejder, and Andreas Zumbusch. Spectral focusing: High spectral resolution spectroscopy with broad-bandwidth laser pulses. *Applied Physics Letters*, 85(1):25–27, 2004.

[73] Minghua Zhuge, Kai-Chih Huang, Hyeon Jeong Lee, Ying Jiang, Yuying Tan, Haonan Lin, Pu-Ting Dong, Guangyuan Zhao, Daniela Matei, Qing Yang, and Ji-Xin Cheng. Ultrasensitive vibrational imaging of retinoids by visible preresonance stimulated Raman scattering microscopy. *Advanced Science*, 8(9):2003136, 2021.

[74] S. A. Asher. UV resonance Raman studies of molecular structure and dynamics: Applications in physical and biophysical chemistry. *Annual Review of Physical Chemistry*, 39(1):537–588, 1988. PMID: 3075468.

[75] A. J. X. Choorakuttil, A. Pruccoli, M. J. Winterhalder, P. Zirak, D. Gudavičius, G. Martynaitis, D. Petrulionis, D. Samsonas, L. Kontenis, and A. Zumbusch. Electronically preresonant stimulated Raman scattering microscopy in the visible. *Applied Physics Letters*, 123(16):163701, 10 2023.

[76] Alan C. Eckbreth and Torger J. Anderson. Dual broadband CARS for simultaneous, multiple species measurements. *Appl. Opt.*, 24(16):2731–2736, Aug 1985.

[77] Tak W. Kee and Marcus T. Cicerone. Simple approach to one-laser, broadband coherent anti-Stokes Raman scattering microscopy. *Opt. Lett.*, 29(23):2701–2703, Dec 2004.

[78] Adrian F Pegoraro, Aaron D Slepkov, Andrew Ridsdale, Douglas J Moffatt, and Albert Stolow. Hyperspectral multimodal CARS microscopy in the fingerprint region. *Journal of biophotonics*, 7(1-2):49–58, 2014.

[79] Feruz Ganikhanov, Silvia Carrasco, X. Sunney Xie, Mordechai Katz, Wolfgang Seitz, and Daniel Kopf. Broadly tunable dual-wavelength light source for coherent anti-Stokes Raman scattering microscopy. *Opt. Lett.*, 31:1292, 2006.

[80] Iestyn Pope, Wolfgang Langbein, Peter Watson, and Paola Borri. Simultaneous hyperspectral differential-CARS, TPF and SHG microscopy with a single 5 fs Ti:Sa laser. *Opt. Express*, 21(6):7096–7106, 2013.

[81] Ondrej Burkacky, Andreas Zumbusch, Christian Brackmann, and Annika Enejder. Dual-pump coherent anti-Stokes Raman scattering microscopy. *Opt. Lett.*, 31:3656, 2006.

[82] Rabah Mouras, G Rischitor, Andy Downes, D Salter, and Alistair Elfick. Nonlinear optical microscopy for drug delivery monitoring and cancer tissue imaging. *J. Raman Spectrosc.*, 41(8):848–852, 2010.

[83] Kotaro Hiramatsu, Tatsuya Tajima, and Keisuke Goda. Ultrafast, dual-band coherent Raman spectroscopy without ultrashort pulses. *ACS Photonics*, 9(11):3522–3528, 2022.

[84] SF57 data sheet, 2 2018.

[85] SF66 data sheet, 2 2014.

[86] Claude A. Klein. Room-temperature dispersion equations for cubic zinc sulfide. *Appl. Opt.*, 25(12):1873–1875, Jun 1986.

[87] Laura L. Listenberger and Deborah A. Brown. Fluorescent detection of lipid droplets and associated proteins. *Current Protocols in Cell Biology*, 35(1):24.2.1–24.2.11, 2007.

[88] Dale Boorman, Iestyn Pope, Francesco Masia, Peter Watson, Paola Borri, and Wolfgang Langbein. Quantification of the nonlinear susceptibility of the hydrogen and deuterium stretch vibration for biomolecules in coherent Raman micro-spectroscopy. *Journal of Raman Spectroscopy*, 52(9):1540–1551, 2021.

[89] Christoph Heinrich, Stefan Bernet, and Monika Ritsch-Marte. Wide-field coherent anti-Stokes Raman scattering microscopy. *Applied Physics Letters*, 84(5):816–818, 01 2004.

[90] I. Toytman, K. Cohn, T. Smith, D. Simanovskii, and D. Palanker. Wide-field coherent anti-Stokes Raman scattering microscopy with non-phase-matching illumination. *Opt. Lett.*, 32(13):1941–1943, Jul 2007.

[91] Christoph Heinrich, Alexander Hofer, Andreas Ritsch, Christian Ciardi, Stefan Bernet, and Monika Ritsch-Marte. Selective imaging of saturated and unsaturated lipids by wide-field CARS-microscopy. *Opt. Express*, 16(4):2699–2708, Feb 2008.

[92] Takeo Minamikawa, Mamoru Hashimoto, Katsumasa Fujita, Satoshi Kawata, and Tsutomu Araki. Multi-focus excitation coherent anti-Stokes Raman scattering (CARS) microscopy and its applications for real-time imaging. *Opt. Express*, 17(12):9526, May 2009.

[93] Robert D Cardiff, Claramae H Miller, and Robert J Munn. Manual hematoxylin and eosin staining of mouse tissue sections. *Cold Spring Harbor Protocols*, 2014(6):pdb–prot073411, 2014.

[94] Jörg Bewersdorf, Rainer Pick, and Stefan W. Hell. Multifocal multiphoton microscopy. *Opt. Lett.*, 23(9):655, May 1998.

[95] Arnica Karuna, Francesco Masia, Paola Borri, and Wolfgang Langbein. Hyperspectral volumetric coherent anti-Stokes Raman scattering microscopy: quantitative volume determination and nacl as non-resonant standard. *J. Raman Spectrosc.*, 47(9):1167–1173, 2016.